

©2017

Benjamin J. Deibert

ALL RIGHTS RESERVED

CATALYTIC AND LUMINESCENT APPLICATIONS OF
METAL-ORGANIC FRAMEWORKS

By

BENJAMIN J. DEIBERT

A dissertation submitted to the

Graduate School-New Brunswick

Rutgers, The State University of New Jersey

In partial fulfillment of the requirements

For the degree of

Doctor of Philosophy

Graduate Program in Chemistry

Written under the direction of

Jing Li

And approved by

New Brunswick, New Jersey

October 2017

ABSTRACT OF THE DISSERTATION
CATALYTIC AND LUMINESCENT APPLICATIONS OF
METAL-ORGANIC FRAMEWORKS

by BENJAMIN J. DEIBERT

Dissertation Director:
Professor Jing Li

Energy consumption is the highest in recorded history and will continue to increase as the population continues to grow and as nations continue developing. More than 80% of human energy consumption originates with the combustion of carbon-based fuels, resulting in the release of carbon dioxide, a greenhouse gas and contributor to anthropogenic climate change. Currently, renewable energy (including hydroelectric) accounts for no more than 20% of total energy consumption. Much of the scientific community is focused on developing cleaner and more efficient energy technologies to address this crisis.

Metal-organic frameworks (MOFs) are a relatively new type of coordination polymer that have been the subject of intense investigation since their popularization around the turn of the millennium. These materials are characterized by metal atoms or clusters connected in infinite crystalline arrays by multi-dentate organic ligands and often possess permanent porosity. The main focus of this project was to investigate the potential of these materials to function as catalysts for artificial photosynthetic reactions modeling natural photosystems (water oxidation and/or CO₂ reduction). As part of this project, it was necessary to set up a lab capable of such catalytic testing. The auxiliary focus of this work was to study and develop MOFs as functional materials for energy efficient luminescent applications.

A manganese MOF bearing a Mn₄O₄ structural subunit was selected for evaluation as a water oxidation catalyst owing to its similarity to the active site in Photosystem II. When

illuminated in a photoassay containing $[\text{Ru}(\text{bpy})_3]^{2+}$ and $\text{S}_2\text{O}_8^{2-}$, $\text{Mn}_4(\mu_3\text{-OMe})_4(\text{nic})_4$ (nic = nicotinate) undergoes transformation to a catalytically active mixed valence layered manganese (III/IV) oxide closely resembling the mineral birnessite. This work led to the hypothesis that the active sites were likely the $\text{Mn}_{\text{interlayer}}^{3+}$ locations, which possess structural similarities to manganite ($\gamma\text{-MnOOH}$). Through collaborative work, manganite was prepared and tested for electrochemically driven water oxidation and was found to have one of the lowest overpotentials for of all reported manganese oxides, second only to bixbyite (Mn_2O_3), but suffers from chemical instability and subsequent deactivation.

The zirconium-porphyrin MOF, PCN-222, was chosen for evaluation as a CO_2 reduction catalyst. PCN-222 boasts aqueous stability over a wide range of pH values, enabling catalytic testing in aqueous solution. Additionally, the porphyrin subunit is a well-studied organic macrocycle capable of housing a metal atom in its core, and shows catalytic activity for CO_2 reduction when metallated with an appropriate metal (Fe, Co, Cu). After setting up a lab capable of CO_2 reduction analysis, preliminary testing was ended when Jiang et al. published work mirroring our study. However, it was found that PCN-222 functions as a reversible colorimetric and fluorescent pH sensing material from a range of pH 0–3, making it one of the first solid-state pH sensors of its kind.

Finally, two new bismuth MOFs were synthesized based on reports of Bi^{3+} having catalytic activity. Bismuth MOFs are rare, with only about ten different varieties reported at the start of this work, and only three with permanent porosity. The rarity of these materials is ascribed to difficulties in obtaining single crystals, which was overcome in this work by employing modulating acids and metal-cluster precursors during synthesis. The first of these two new Bi MOFs features a large tetracarboxylate linker based on the tetraphenylethylene core, which is known as an aggregation-induced emission (AIE) fluorophore. The resulting structure is anionic and has charge balancing K^+ ions, which form a 1-D chain with Bi. The as-made material

has strong green luminescence that undergoes significant emission wavelength shifting upon solvent removal. When fully activated, the solvochromic material adopts yellow emission with a maximum wavelength of ~553 nm and a quantum yield of ~74% under blue-light excitation (455 nm). The high quantum yield and blue-excitable yellow emission makes this MOF a strong candidate for use in phosphor-converted white LEDs.

Utilizing the synthetic strategy developed in the former case, another new Bi MOF was prepared. This material is also constructed from a tetracarboxylate linker, but is based on the well-known macrocyclic porphyrin subunit. The resulting anionic MOF framework is charge balanced by dimethylammonium cations formed in-situ during synthesis. Structural changes occur upon guest-cation exchange with lithium, reducing the three-fold intercalation state to two-fold. Additional structural changes are observed upon solvent exchange, demonstrating framework flexibility due to the flexible coordination geometry of Bi^{3+} . This material can be prepared with 2+ and 3+ transition metal cations (Cu^{2+} , Ni^{2+} , Fe^{3+} , Mn^{3+}) occupying the linker's macrocyclic core, resulting in a trimetallic MOF. The Fe^{3+} containing phase was examined as a potential catalyst for electrocatalytic CO_2 reduction under non-aqueous conditions. At an applied potential of -1.7 V vs. Ag/AgCl, CO and H_2 are produced in roughly equal mole quantities. Further testing is underway to fully benchmark the MOF's catalytic performance.

ACKNOWLEDGEMENT

First, I would like to express my sincere gratitude to my research advisor, Prof. Jing Li. It was due to her encouragement during my undergraduate tenure that I began down the path of MOF research in the first place. Dr. Li was consistently supportive throughout my time in the group, and has always made herself available for guidance and advice. She is one of the hardest working people I know and has set an example that I hope to follow in the years to come. I am also especially grateful to my dissertation committee: Profs. Teddy Asefa, Steven Rowley, and Ralf Warmuth. Throughout the years they have provided valuable insight that is obtainable only after years of research and exposure to the scientific community. They were never short on constructive comments and encouragement; I could not have chosen a better or kinder group of people to work with.

I would also like to thank the Li group members (both former and current) who have made the approximately 16,000 hours spent in the lab a pleasant experience. Special thanks to Dr. Jingming Zhang for his tutelage, friendship, and support, Wei Liu for being one of the most supportive and generous people I have met, and Hao Wang for always being willing to help in the lab, no matter how trivial a task. I am also grateful to the following members who have all contributed to the following dissertation work in one way or another (in no particular order): Dr. David Olsen, Dr. Sujing Wang, Dr. Debasis Banerjee, Dr. Baiyan Li, Ever Velasco, Bill Lustig, Nate Rudd, Yang Fang, Dr. Zhichao Hu, Dr. Qihan Gong, Kun Zhu, Willy Gonzalez, Lucy Lee, Michael Yang, and Iyanosa Ogbevoen.

Throughout the past five years, I have worked with many great people, many of whom have made significant contributions to the following work. Prof. G. Charles Dismukes and his research group have been essential collaborators for almost all of our catalytic studies, especially Dr. Paul Smith, Dr. Anders Laursen, and Karin Calvinho. Due to the nature starting in a new field, especially a nuanced one like electrochemistry, I often say I have probably made every

rookie mistake one can make – in the events that I missed some, it was likely due to their guidance. Prof. Ki Bum Li and his group members, Nick Pasquale, Yichao Zhang, and Hadifa Rabie, were wonderful lab neighbors who were always quick to help with any number of issues. I am also grateful to our other essential collaborators for their valuable contributions: the crystallography wizards, Dr. Tom Emge and Dr. Simon Teat, Dr. Sylvie Rangan for her XPS tutelage and assistance, Dr. Karena Chapman for the PDF data and explanations, and especially Dr. Gene Hall, who has never turned down a request for his analysis assistance.

None of this would have been possible if not for the loving support and encouragement of my father, Mark Deibert, my mother, Joanne Deibert, and especially my fiancé, Rachel Spring. Rachel has been an endless well of support, despite my long hours in the lab, often on weekends and holidays. It takes a special kind of personal fortitude to be in a relationship with a research-based graduate student. No matter the situation, I know I can always count on her and I could not have done this without her. I am extremely fortunate to have these people in my life.

Finally, I want to express my deepest gratitude to my Aunt Sharon Quinlan, and brother Wayne Laul. If I am anywhere today, it is because of them.

Dedicated to:

Sharon Quinlan

TABLE OF CONTENTS

ABSTRACT OF THE DISSERTATION	ii
ACKNOWLEDGEMENT	v
TABLE OF CONTENTS.....	vii
LIST OF TABLES.....	x
LIST OF ILLUSTRATIONS.....	xi
LIST OF ABBREVIATIONS.....	xviii
CHAPTER 1: Introduction	1
1.1 The Grand Challenge	1
1.2 Metal-Organic Frameworks	3
1.2.1 Network Topology and Design.....	4
1.2.2 Synthetic Conditions and Single Crystal Growth	8
1.2.3 Modulated Synthesis.....	10
1.2.4 Crystal Structure and Porosity Characterization	11
1.3 MOFs for Catalytic and Luminescent Applications	13
CHAPTER 2. Surface and Structural Investigation of MnO _x Birnessite-type Water Oxidation Catalyst Formed under Photocatalytic Conditions ⁵¹	18
2.1 Introduction.....	18
2.2 Experimental Details.....	21
2.2.1 Material Synthesis.....	21
2.2.2 Photochemical Reactions	22
2.2.3 Instrumental Details	23
2.2.4 Mn content via XPS and TGA data	26
2.3 Results and Discussion	29
2.3.1 Models for Performance of ⁴ MnO _x	35

2.3.2 XPS Surface Investigation	36
2.3.3 $^{4}\text{MnO}_x$ Structural Characterization	41
2.3.4 $^{4}\text{MnO}_x$ Formation	48
2.4 Conclusion	49
2.5 Collaborative Follow-Up Study on Manganite as a Water-Oxidation Catalyst ¹³⁸	50
CHAPTER 3. Distinct Reversible Colorimetric and Fluorescent Low pH Response on a Water-Stable Zirconium-Porphyrin Metal-Organic Framework ⁵⁰	55
3.1 Introduction.....	55
3.2 Experimental Details.....	57
3.2.1 Material Synthesis.....	57
3.2.2 Sample Preparation	57
3.2.3 Experimental Methods	58
3.2.4 Instrumental Details	58
3.3 Results and Discussion	58
3.4 Conclusion	67
3.5 Preliminary Results of PCN-222 Photocatalytic CO_2 Reduction.....	68
CHAPTER 4. High-Performance Blue-Excitable Yellow Phosphor Obtained from an Activated Solvochromic Bismuth-Fluorophore Metal–Organic Framework ³⁵	69
3.1 Introduction.....	69
4.2 Experimental Details.....	71
4.2.1 Ligand Synthesis	72
4.2.2 $\text{Bi}_4\text{O}_2(\text{Hsal})_8 \cdot 2\text{MeCN}$ Synthesis	73
4.2.3 $[\text{BiK}(\text{tcbpe})(\text{DMF})_2] \cdot x\text{DMF}$ Synthesis	73
4.2.4 Activation Procedure and Solvochromic Studies for the Transformation of 1 to 1A ...	74
4.2.5 PC-WLED Coating	75
4.2.6 Instrumental Details	75
4.3 Results and Discussion	76

4.4 Conclusion	90
CHAPTER 5. Structural Versatility and Electrocatalytic Activity of an Anionic Bi-porphyrin Metal-Organic Framework.....	91
5.1 Introduction.....	91
5.2 Experimental Details.....	94
5.2.1 Ligand Synthesis.....	94
5.2.2 MOF Synthesis.....	95
5.2.3 Instrumental Details	97
5.3 Results and Discussion	101
5.4 Future Outlook	118
Appendix I	119
Appendix II	119
References.....	120

LIST OF TABLES

Table 2.1. Multiplet Fitting Parameters for Mn 2p _{3/2} Spectra.....	37
Table 2.2. XPS Survey Scan Atomic Percentages	39
Table 2.3. Estimated relative abundances of Mn oxidation states on catalyst surfaces from XPS measurements.....	41
Table 4.1. Crystal data and structure refinement for 1 (LMOF-401).....	78
Table 4.2: Quantum yield values obtained at different excitation energies.	86
Table 5.1. Crystal data and structure refinement for DMA+-Bi-tcpp.....	104
Table 5.2. Crystal data and structure refinement for Li-Bi-tcpp.....	113

LIST OF ILLUSTRATIONS

Figure 1.1. (a) Conceptual illustration of MOF self-assembly. (b) Examples of organic ligands used in MOF construction.....	4
Figure 1.2. Examples of the building block (reticular) approach applied to some commonly formed MOF SBUs.	5
Figure 1.3. Structure plot of MOF-5 and its underlying 6-connected net (pcu topology).....	6
Figure 1.4. Structure plots of PCN-222, 225, and 224.....	7
Figure 1.5. Conceptual illustration of the ligand exchange mechanism and possible synthetic intermediates during MOF synthesis using benzoic acid as a modulator.	11
Figure 1.6. Structure plots of trinuclear basic metal acetate [$M_3O(CO_2)_6L_3$] and dinuclear ‘paddlewheel’ [$M_2(CO_2)_4L_2$] SBUs containing OMSs.....	14
Figure 1.7. Conceptual illustration of the two main pathways for utilizing porphyrin in the construction of a MOF CO ₂ reduction catalyst.	15
Figure 1.8. (a) AIE fluorophore tetraphenylethylene (tpe). (b) Conceptual illustration of ligand-based luminescence and guest induced quenching.	16
Figure 2.0. TGA curve for ⁴ MnO _x (top) and ⁵ MnO _x (bottom).	28
Figure 2.1 Conceptual drawing of the conversion of Mn ₄ (μ ₃ -OMe) ₄ (nic) ₄ to ⁴ MnO _x with subsequent catalytic water oxidation.	29
Figure 2.2. (a) Microscope image of as-synthesized Mn ₄ -MOF (inset shows bulk synthesis product, scale = 1.0 mm); (b) zoom out HR-TEM image of catalyst ⁴ MnO _x ; (c) structure-plot of Mn ₄ -MOF (green polyhedrons represent cube-shaped SBU); (d) generic conceptual drawing of layered MnO ₂ (triclinic-type) with disordered interlayer.....	30

Figure 2.3. (a) Simulated and measured PXRD patterns for Mn ₄ -MOF (green), ⁴ MnO _x (black), ⁵ MnO _x (blue), and HexBir (purple). (b) Dissolved oxygen concentration measured by Clark-type electrode at 20 °C using 125 ppm catalyst concentration in 2 mL bicarbonate buffer (pH 7) with 0.5 mM Ru(bpy) ₃ Cl ₂ ·6H ₂ O and 10 mM Na ₂ S ₂ O ₈ . Illumination begins at time t ≈ 25 s.	31
Figure 2.4. Emission profile for the WLED lamps.	32
Figure 2.6. β-MnO ₂ Mn 2p _{3/2} spectra	37
Figure 2.7. Mn 2p _{3/2} XPS spectra. (a) Deconvoluted spectra for ⁴ MnO _x (top left), ⁵ MnO _x (top right), HexBir (bottom left), and HexBir AR (bottom right). Traces: experimental data (boxes), overall fit (black), Mn ⁴⁺ (purple), Mn ³⁺ (pink), Mn ²⁺ (green), residual (grey dash below spectra). (b) Intensity and binding energy normalized Mn 2p _{3/2} spectral data overlay (experimental). β-MnO ₂ (reference sample, red), ⁴ MnO _x (black), ⁵ MnO _x (blue), HexBir (purple), and HexBir AR (purple dashed).	38
Figure 2.8. XPS survey scans.	39
Figure 2.9. Synchrotron PXRD pattern for ⁴ MnO _x	43
Figure 2.10. Comparison of the experimental G(<i>r</i>) obtained for ⁴ MnO _x (black) with the calculated G(<i>r</i>) for the refined birnessite structure model (red). Illustrations correlate distances obtained by the PDF study with distances found within a single birnessite layer. Inset shows PDF data expanded to 20 Å and the dashed line shows the residual pattern.	43
Figure 2.11. Idealized conceptual drawing of 4MnO _x along the crystallographic c-axis (a) and b-axis (b). Interlayer/surface Mn ³⁺ species over vacant sites are represented as the triply bonded species Mn atoms in (a) and as the Mn octahedra out of the layer plane in (b).	44
Figure 2.12. Comparison of PDF bond parameters resulting from current study to those of Zhu et al. ¹²⁹ (a) Mn-O bond length; (b) Mn-Mn distance (u ₃ -O bridged); (c) ratio of Mn-Mn:Mn-O distance; (d) ratios of Mn-O:Mn-Mn peak intensities and peak widths.	44

Figure 2.13. Raman spectra of Mn ₄ -MOF (green), ⁴ MnO _x (black), and δ-MnO ₂ (purple).	47
Figure 2.14. HR-TEM images of ⁴ MnO _x . (a) 50 nm scale showing layered flake-like morphology; (b) 5 nm scale showing disordered basal plane, the inset is a magnification of the indicated region showing ~ 2.8 Å lattice fringes; (c) 10 nm scale showing lattice fringe curvature.	48
Figure 2.15. Structural illustration of the equilibrium between δ-MnO ₂ and γ-MnOOH.	51
environment.	51
Figure 2.16. “Cyclic voltammograms (10 mV/s, iR corrected) for the 1 × 1 tunnel manganese oxides of Figure 1 in 1 M NaOH or 1 M phosphate buffer, with loading 0.5 mg/cm ² . Conditions: 5 mm glassy-carbon working electrode, Ti counter electrode, reference electrodes Hg/HgO (pH 14, E _{ref} = +0.100 V vs NHE) and Ag/AgCl (pH 7). The silver reference electrode was externally calibrated vs SCE (E _{ref} = +0.240 V vs NHE). Overpotentials are corrected for the pH dependence of water oxidation and given relative to each reference electrode using the expression (measured potential) – (1.23 V – (0.059 × pH) – E _{ref}). The current is normalized to the geometric electrode area.” ¹³⁷	52
Figure 2.17. Crystal structure illustrations of various tested phases of manganese-oxide.....	53
Figure 2.18. “Mn 2p _{3/2} region of XPS spectra comparing γ-MnOOH (A), β-MnO ₂ (C), and electrochemically oxidized γ-MnOOH (B). These spectra are deconvoluted into contributions from Mn ⁴⁺ (purple), Mn ³⁺ (green), and Mn ²⁺ (red) via the method of Nesbitt and Banerjee as described previously.” ¹³⁷	54
Figure 3.1. Structural drawings of PCN-222 along the crystallographic c axis (a), and a axis (b); images showing the accessibility of the porphyrin linker from inside the ~3.7 (c) and ~1.3 (d) nm diameter pores; protonation of the H ₂ tcpp linker (e).	56
Figure 3.2. PXRD patterns: simulated pattern for PCN-222(Fe) (black); activated PCN-222 sample (purple); activated PCN-222 sample while immersed in 1.0M HCl (red); recovered 1.0M	

HCl sample washed with H ₂ O/DMF/acetone (green); recovered sample soaking in conc. HCl for 6 hours then washed with H ₂ O/DMF/acetone (orange); older/different sample of PCN-222 soaked in H ₂ O for 9 months (blue).	60
Figure 3.3. Photographs of PCN-222 samples (a) and ligand H ₆ tcpp (b) under ambient light. These samples are exposed to acidic solutions at various concentrations, followed by reversal washes in between each exposure; exposures were made in the order in which they appear from top left to bottom right. Caption photos are intended demonstrate responsiveness.	61
Figure 3.4. Solid state UV-Vis data for H ₆ tcpp collected after exposure to varying concentrations of HCl and reversal washes with H ₂ O.	62
Figure 3.5. UV-Vis spectra for PCN-222 after exposure to varying concentrations of HCl solution (a) and after reversing the effect by washing with H ₂ O and DMF (b). Measurements were made in the order in which they appear in the legend from top to bottom, where Wash 1 corresponds to washing PCN-222 with no acid exposure.	63
Figure 3.6. Solid state UV-Vis data for PCN-222 comparing bandgap energies after exposure to varying concentrations of HCl.	64
Figure 3.7. Photoluminescence data for PCN-222 after exposure to varying concentrations of HCl solution (a) and after reversing the effect by washing with H ₂ O and DMF (b). Measurements were made in the order in which they appear in the legend from top to bottom, where Wash 1 corresponds to washing PCN-222 with no acid exposure.	65
Figure 3.8. PCN-222 fluorescence excitation spectrum; monitored at 489 nm emission.	66
Figure 3.9. H ₆ tcpp solid state emission spectrum. Slide sample was prepared using the same method as for PCN-222.	66
Figure 4.1. Structure of H ₄ tcbpe ligand.	70

Figure 4.2. a) Structure plots of 1 along the crystallographic b-axis (left) and slightly rotated from the a-axis (right). b) Coordination geometry of Bi ³⁺ with approximate location of 6s ² lone pair and polyhedral representation. c) Single Bi-tcbpe 4,4-connected net along the b-axis. d) Line connectivity drawing showing the two-fold interpenetration of the Bi-tcbpe nets.	79
Figure 4.3. Structure plots of 1 along the b-axis (a, b) and a slightly rotated a-axis (c, d); b) and d) show the connectivity of a single Bi-tcbpe net with potassium bonds removed. e) Close-up view of the inorganic Bi-K chain formed through u ₃ -O carboxylate and DMF oxygens (red and black spheres, respectively).	80
Figure 4.4. Polyhedral representation of the individual Bi-tcbpe nets in 1 as viewed along the crystallographic a, b and c axes (a, b, and c, respectively). d) Connectivity of the highly distorted tetrahedral and rectangular building units.	81
Figure 4.5. Data for 1 at various stages of desolvation. The colored legend lists the percent weight and estimated number of DMF (per formula unit) remaining in the sample. a) Optical micrographs under ambient light (top row) and 395 nm UV light (bottom row). b) Emission spectra, $\lambda_{\text{ex}} = 360$ nm. c) CIE coordinates calculated from the PL spectra. d) PXRD patterns showing structural changes in response to DMF content.	83
Figure 4.6. UV-Vis spectra of 1 (black), partially desolvated 1 (sky blue), 1A (red), and H ₄ tcbpe (dotted black). Corresponding lines were added to show the positions used to estimate the optical band gap, which are listed in the bottom right.	84
Figure 4.7. PL excitation (top) and emission (bottom) spectra for 1 at various stages of desolvation. The colored legend lists the approximate DMF content per formula unit, and the emission maximum wavelength ($\lambda_{\text{ex}} = 360$ nm) used for monitoring during excitation measurements.	85

Figure 4.8. TGA profile for samples of 1 at various stages of desolvation. The colored legend at the bottom lists the weight loss in the grey region for each trace, and the corresponding number of calculated DMF molecules per formula unit (including the two coordinated DMF).....	86
Figure 4.9. PXRD patterns for 1 during various stages of desolvation. The grey arrows mark the appearance and growth of the peaks corresponding to the activated phase.	88
Figure 4.10. a) QY scaled PL excitation (dotted traces) and emission ($\lambda_{\text{ex}} = 455$ nm, solid traces) spectra for 1A (red), YAG:Ce ³⁺ (black) and H ₄ tcbpe (blue); excitation spectra monitored at 553 nm for 1A , 543 nm for YAG:Ce ³⁺ , and 550 nm for H ₄ tcbpe. b-e) 10W blue LED chip (450-455 nm) uncoated and coated with 1A under ambient lighting (b,d) and powered on (9V DC) (c, e).	89
Figure 5.1. Photograph of the custom-made electrochemical cell and a schematic illustration of the Toray working electrodes used for BE measurements.	99
Figure 5.2. Representative chromatogram and analysis results of the calibration gas.....	101
Figure 5.3. Optical micrographs of DMA ⁺ -Bi-tcpp crystals.....	102
Figure 5.4. Structure plots and unit cell information for DMA ⁺ -Bi-tcpp and Li-Bi-tcpp.....	102
Figure 5.5. Polyhedral net, line drawings, and PBU ‘chains’ of DMA ⁺ -Bi-tcpp and Li-Bi-tcpp.	103
Figure 5.6. Simulated, as-made, directly outgassed, and solvent exchanged PXRD patterns for DMA ⁺ -Bi-tcpp.	106
Figure 5.7. TGA profile for DMA ⁺ -Bi-tcpp as-made (black) and solvent exchanges samples. ...	106
Figure 5.8. TGA profile of MeOH exchanged DMA ⁺ -Bi-tcpp after applying dynamic vacuum at room temperature overnight.....	107
Figure 5.9. PXRD patterns for DMA ⁺ -Bi-tcpp (black = simulated pattern) after MeOH exchange followed by outgassing under dynamic vacuum at room temperature (red) and after heating at 85 °C for 4 hours (blue).	107

Figure 5.10. Depiction of π stacking in DMA ⁺ -Bi-tcpp, photographs of the ITO electrode used for photocurrent measurements, and photocurrent response under chopped white LED light at 30 sec intervals.....	109
Figure 5.11. PXRD of DMA ⁺ -Bi-tcpp after 1 and 3 days of Li ⁺ cation exchange.....	109
Figure 5.12. TGA profile of Li@Bi-tcpp after 3 days of exchange time.....	110
Figure 5.13. PXRD patterns for DMA ⁺ -Bi-tcpp (simulated, black), Li@Bi-tcpp (grey), and samples prepared with Li ⁺ present during synthetic trials (light to dark blue).	111
Figure 5.14. Simulated PXRD pattern comparison for Li-Bi-tcpp (bottom, black) and DMA ⁺ -Bi-tcpp (top, red).....	111
Figure 5.15. TGA profile for as-made Li-Bi-tcpp (red) and acetone exchanged DMA ⁺ -Bi-tcpp (black).	114
Figure 5.16. CO ₂ sorption isotherm for Li-Bi-tcpp.....	114
Figure 5.17. CV data for (a) DMA ⁺ -Bi-tcpp-Cu, (b) DMA ⁺ -Bi-tcpp-Ni, and (c) Li-Bi-tcpp-Fe. (d) BE data for the bare Toray electrode (blue) and Li-Bi-tcpp-Fe (black).	116
Figure 5.18. Product distribution after BE measurements on the bare Toray electrode and Li-Bi-tcpp-Fe with conductive carbon.....	116
Figure 5.19. Optical micrographs of Li-Bi-tcpp-Fe/Toray composites. The inset images show zoomed out images of the coated carbon fiber paper; (a) manual application of catalyst showing poor catalyst-fiber contact, (b-f) direct growth on Toray paper with decreasing concentrations of benzoic acid.	117

LIST OF ABBREVIATIONS

AIE	aggregation induced emission
BET	Brauner-Emmett-Teller
BE	bulk electrolysis
CP	coordination polymer
CV	cyclic voltammetry
DMA	dimethylacetamide
DMF	dimethylformamide
EtOH	ethanol
FID	flame ionization detector
GC	gas chromatography
GHG	greenhouse gas
HER	hydrogen evolution reaction
LBS	Lewis-basic site
MeCN	acetonitrile
MeOH	methanol
MOF	metal-organic framework
nic	nicotinic acid/nicotinate
OER	oxygen evolution reaction
OMS	open-metal site
PBU	primary building unit
PCN	porous coordination network
PDF	pair-distribution function
PL	photoluminescence
PXRD	powder X-ray diffraction

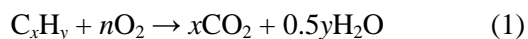
RCSR	reticular chemistry structure database
SBU	secondary building unit
tcbpe	4', 4''', 4''''', 4'''''''- (ethene-1,1,2,2-tetrayl)
	tetrakis([1,1'-biphenyl]-4-carboxylic acid))
TCD	thermal conductivity detector
tcpp	meso-Tetrakis(4-carboxyphenyl)porphyrin
TGA	thermogravimetric analysis
tpe	tetraphenylethylene
UiO	University of Oslo
UV-Vis	ultraviolet-visible spectroscopy
XRD	X-ray diffraction

CHAPTER 1: Introduction

1.1 The Grand Challenge

The overall scientific consensus is that human activity is anomalously increasing average global temperatures through the release of greenhouse gases (GHGs), such as CO₂, CH₄, and NO_x.¹ While this concept has become a highly politicized ‘hot-button’ topic, it is not a new one. The idea of heat-trapping gases in Earth’s atmosphere was first discussed by scientists in the early 19th century. By mid-century John Tyndall had identified water vapor and CO₂ as GHGs.² In the late 1800’s Svante Arrhenius hypothesized that via natural cycles (volcanoes, oceanic uptake, geochemical process, etc.), CO₂ acts as a sort of long-term regulator on global temperatures and calculated that halving the concentration of CO₂ in the atmosphere would result in a 4-5 °C reduction in average European temperatures.³ In 1894, Arrhenius’s colleague Arvid Högbom calculated that CO₂ emitted from industrial activity was comparable natural geochemical processes, suggesting that human activity can indeed affect global temperature.⁴ The atmospheric concentration of CO₂ is currently around 400 ppm, the highest it has been for over 800,000 years. Prior to 1950, CO₂ cycled naturally between about 170 and 300 ppm with closely tracking average global temperature changes, illustrating a significant cause for concern.⁵⁻⁶

In 2016, the Population Reference Bureau estimated Earth’s population at 7.4 billion, which is predicted to grow to 10 billion by the year 2050.⁷ To put this in perspective, 200 years ago the global population was only an estimated 1 billion. Human energy consumption is at record highs and will continue increasing as the population continues to grow and as more nations to continue to develop industrially. This is problematic considering that more than 80% of societal energy consumption originates from the combustion of carbon-based fossil fuels,⁸ resulting in the release of carbon dioxide (eqn. 1). While carbon-neutral renewable energy



sources are available and in use, they only account for about 18-20% of the total energy consumption, and only about 3% of that from variable renewables (solar, wind, tidal, geothermal). Since the theoretical calculations of Arrhenius and Högbom, yearly CO₂ emissions have risen from an estimated 534 million metric tons in 1900, to 9855 tons in 2014.⁹⁻¹⁰

Much of the scientific and engineering community is working towards addressing this critical issue, with the grand challenge of developing a carbon neutral energy infrastructure. This is possible via numerous methods, but it is clear that for the foreseeable future no single technology is sufficient to address the issue entirely. The current paradigm of thought is that adoption of a combination of carbon neutral energy sources, such as wind, solar, tidal, geothermal, nuclear, hydroelectric, etc. is required, and deployment of such technologies can be observed in many parts of the world. From a materials science standpoint, this crisis serves as an opportunity to develop energy efficient materials to help reduce carbon emissions, as well as develop alternative energy sources. A recent example of such a technology is LED (light emitting diode) lighting, which has recently proven to drastically reduce the overall energy cost of general lighting, thereby reducing carbon emissions.¹¹

One of the most promising technologies currently being developed is artificial photosynthesis in the form of water splitting and carbon dioxide reduction. Solar energy is one of the most abundant renewable energy resources available, and is therefore considered to be a key element for energy sustainability. Hydrogen produced from solar driven water splitting poses a particularly attractive alternative to fossil fuels owing to the availability of water and solar resources. Alternatively, utilizing solar energy to reduce CO₂, either directly with a photocatalyst or indirectly as electrical energy with an appropriate electrocatalyst, has enormous potential. As the byproduct of all fossil fuel based combustion reactions, there is little shortage of CO₂ as a chemical feedstock. If CO₂ captured from combustion emissions can be reduced directly back

into a usable fuel, such as methane or methanol, it could ‘close the loop’ of carbon emissions and help reduce our overall contribution to climate change.

1.2 Metal-Organic Frameworks

Metal-organic frameworks (MOFs) are a type of coordination polymer (CP) that were popularized in the late 1990’s when Li et al. from Omar Yaghi’s lab at Berkeley reported the structure of a porous coordination polymer featuring zinc-carboxylate linkages, dubbed MOF-5, and coined the term ‘metal-organic framework’.¹² This famous work opened up a research area that has since witnessed incredible growth – searching the term ‘metal-organic framework’ on SciFinder produces over 30,000 references which have been published since then. Despite MOFs recent popularization, the term coordination polymer was can be traced back to a 1960’s review article by J.C. Bailar, and the structures of these materials were being studied as early as the 1950’s, when they were almost exclusively composed of cyanide bridges. In 1989, Robson et al. pushed the field forward by designing a CP comprised of copper and a tetrahedral shaped organic ligand, which established the use of tunable organic ligands in CP design. The field continued to develop from there, with ligands evolving to nitriles and polypyridyl species. Kitagawa and coworkers reported the first permanently microporous pyridyl based CP in 1997.¹³

MOFs are self-assembled materials constructed from metal atoms (primary building units, PBUs) or polyatomic metal clusters (secondary building units, SBUs) connected in infinite one-, two-, or three-dimensional crystalline arrays by polytopic organic ligands via classical coordination bonds (Figure 1.1). They often possess high permanent porosity (remain porous upon solvent removal) and can boast immense internal surface areas (upwards of 10,000 m²/g), promoting accessibility to internal functional groups, such as open metal sites (OMS) and organic Lewis basic sites (LBS), where desirable interactions with guest molecules can occur.¹⁴⁻¹⁵ These combined features have promoted studies on MOFs for wide variety of potential applications, some of which include: gas storage and separation, luminescence sensing and

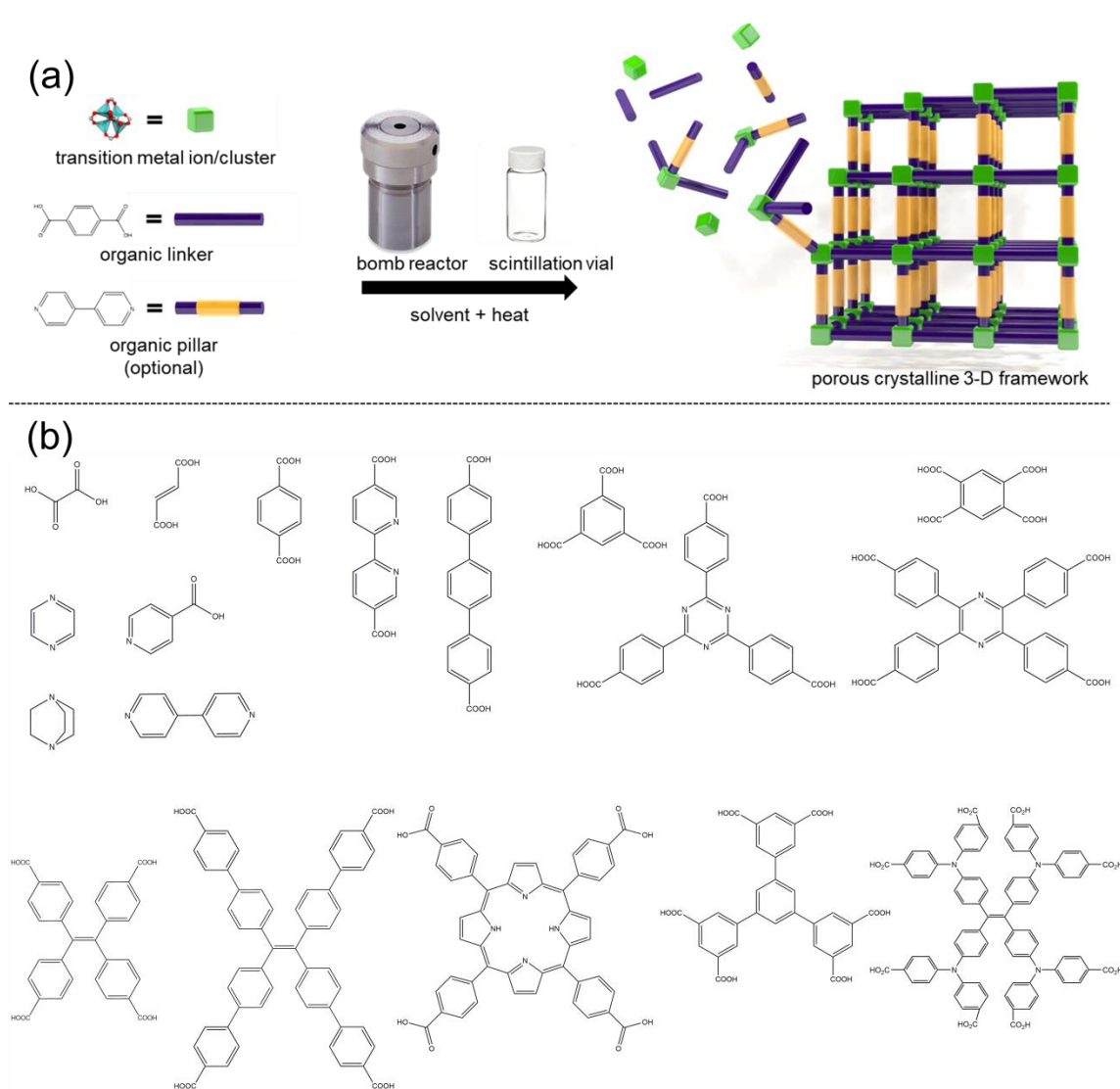


Figure 1.1. (a) Conceptual illustration of MOF self-assembly. (b) Examples of organic ligands used in MOF construction.

general lighting, catalysis, water and nuclear waste remediation, drug delivery and bio-imaging, proton conductivity for fuel cells, water harvesting from air, etc.¹⁶ There is doubtlessly a multitude of potential applications as of yet studied for MOFs, which is intrinsic to their allure.

1.2.1 Network Topology and Design

A building block approach, termed *reticular chemistry*, can be invoked in the design of MOF structures, where the metal and organic subunits are treated as nodes and spacers, respectively. Crystal structures have long been described in terms of connected nets, with atoms considered as vertices and bonds as the links between them (edges). Similarly, coordination polymers built on ditopic linkers extend this concept, where the metal atom functions as the vertex, but instead of the bonds acting as the edges, the organic linker serves as the edge connecting two vertices, resulting in a periodic net that describes the underlying crystal topology. MOF structures take this approach one step further. In the case of MOFs bearing polyatomic metal clusters (SBUs), the overall SBU connectivity is treated as the vertices (nodes) (Figure 1.2), and ditopic linkers as the edges (spacers). In contrast to early coordination polymers employing dipyriddy or cyanide spacers, the nodal coordination geometry of carboxylate based MOFs is dictated by carboxylate geometric positioning, as opposed to the coordination environment of the metal. When polytopic linkers with more than two points of connectivity are integrated, additional vertices exist at the geometric center of the linkers, while the edges remain as the

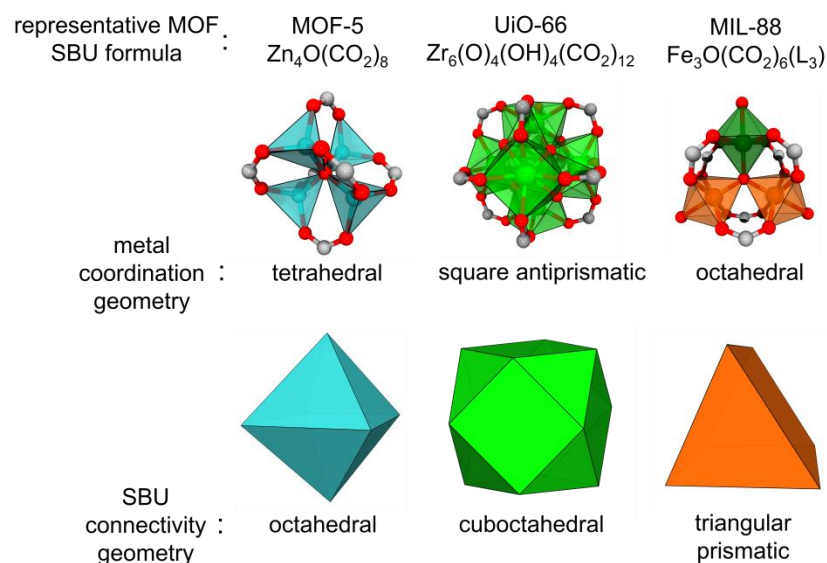


Figure 1.2. Examples of the building block (reticular) approach applied to some commonly formed MOF SBUs.

organic moieties between these central points and the SBUs. One way to describe the resulting vertex-edge net is by using the (n,m) -connected net convention. In this case, n represents the overall connectivity to points of extension (edges) of the main building unit, typically a PBU or SBU. The term m represents the overall connectivity of the linker connecting the main vertices, where $m \geq 3$. In the event that $m = 2$, the net is simply described as an n -connected net (Figure 1.3). *Reticular chemistry*, a term coined by Michael O’Keefe and Omar Yaghi’s efforts, utilizes these features by assuming there are a limited number of nets (underlying topologies) that exist for a given combination of geometric building blocks, regardless of the constituents that give rise to vertices (n,m) or edges.¹⁷ In 2008 a naming scheme was created to define these specific topologies and the Reticular Chemistry Structure Database (RCSR) serves as the main archive of all reported topological nets. As an archetypical example, MOF-5 has a tetranuclear zinc SBU, with each Zn atom having tetrahedral geometry; the SBUs are connected by ditopic terephthate linkers.¹² Using the reticular approach, these SBUs can be viewed as octahedrons with respect to linker connectivity, and the underlying 6-connected net adopts **pcu** topology (Figure 1.3).

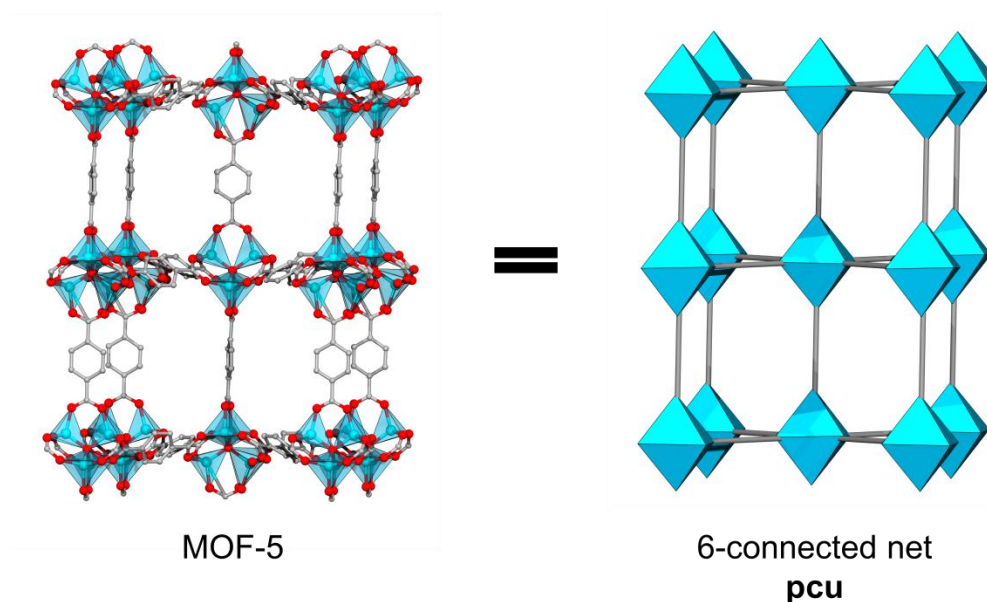


Figure 1.3. Structure plot of MOF-5 and its underlying 6-connected net (**pcu** topology).

It is possible to predict MOF topologies *a priori* using the reticular chemistry approach, assuming that building block geometries from specific metal/linker combinations are well established.¹⁸ This is especially true in the case of MOF syntheses using metals that have a tendency to form the same SBU under a given set of conditions and ditopic linkers. However, when using polytopic linkers that serve as a second vertex (more than two points of connectivity and deviate from 1-dimension), it becomes significantly more difficult to make accurate predictions about resulting topologies. Stated another way, as vertex connectivity, n and m , increases, so does the number of possible topologies for a given combination. Additional phenomena, such as linker flexibility, torsion angles, linker vacancies and terminal ligands, etc., can further complicate such predictions and can result in deviation from expected topologies. The PCN-22X (PCN = porous coordination network) family of MOFs prepared in Hong Cai Zhou's lab serve as an example (Figure 1.4).¹⁹⁻²¹ The SBUs of these MOFs is the well-known hexanuclear zirconium node, $Zr_6(u_3-O)_4(\mu_3-OH)_4$, the most common building node of Zr-based MOFs (Figure 1.2), which was originally reported in the Zr-terephthalate structure, UiO-66 (UiO = University of Oslo).²² This Zr cluster can be viewed as an octahedron with Zr atoms occupying the vertices with carboxylate linkages extending from the edges, accommodating up to 12 points of extension when 1-D linkers are employed; the resulting network topology is **fcu**. In contrast, the PCN-22X series utilizes a tetracarboxylate linker with square planar geometry, tetrakis(4-

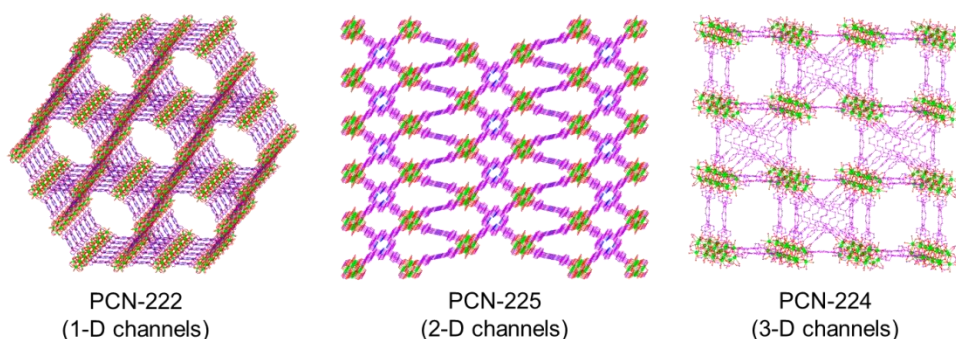


Figure 1.4. Structure plots of PCN-222, 225, and 224.

carboxyphenyl)porphyrin (tcpp), resulting reduced SBU connectivity. In fact, three different structures with three unique topologies are reported based on this combination. PCN-222 and -225 (**kag** and **sqc** topologies, respectively) both have 8 points of extension from their SBUs, reducing the symmetry of the Zr SBU cluster from O_h to D_{4h} and D_{2d} , respectively. The PCN-224 SBU (**she** topology) has only 6 points of linker extension and has D_{3d} cluster symmetry as a result. In all cases, hydroxyl groups serve as terminal ligands where carboxylate vacancies exist.

MOFs are well-known as being ‘tunable’ materials.²³ Besides changing metal species or organic functional moieties, the pore sizes of MOFs can be specifically tailored by changing the ligand length of known structures, resulting in ‘isorecticular’ frameworks. Isorecticular structures have the same underlying topology but can differ by vertex surface areas and edge lengths. This was initially demonstrated by Yaghi’s lab with the IR-MOF series (IR = isorecticular), but can also be observed in a number of other structures, including UiO-66, -67, and -68.^{22, 24} By changing the linker from terephthalate (1,4-benzenedicarboxylate = bdc), to biphenyldicarboxylate (bpdc) or triphenyldicarboxylate (tpdc), a series of isorecticular networks is obtained with increasing pore sizes commensurate with increasing ligand length.

1.2.2 Synthetic Conditions and Single Crystal Growth

Metal-organic frameworks generally form via self-assembly, meaning no template or external structure directing agent is required. The coordination environment of the metal or metal cluster primarily acts as the structure directing impetus. Most often, traditional inorganic salts of nitrate, sulfate, chloride, acetate, etc. are paired with multi-dentate carboxylic acids, carboxylate salts, or polyamines. MOFs have also been constructed from organic phosphates and sulfonates, and functional groups such as hydroxides can partake in metal-ligand bonding.

Syntheses traditionally proceed via single-step one-pot solvothermal reactions at autogenous pressure, superficially rendering synthesis a fairly simplistic process. Specific

conditions are largely dictated by the properties of the constituent metal and ligands, and solvents and reaction temperatures are chosen accordingly. Because reactions contain both metal and organic species, solvents are typically protic or aprotic organic solvents having relatively high dielectric constants in order to dissolve both the organic and inorganic components. Examples of some of common solvents used in MOF syntheses include dimethylformamide (DMF), dimethylacetamide (DMA), diethylformamide (DEF), and dimethylsulfoxide (DMSO). Water can also be used as solvent, but ligand solubility can be problematic, in which case converting carboxylic acids to carboxylate salts, or employing mixed solvents can aid dissolution. Worth noting is that the constituents need not necessarily be totally dissolved, where undissolved reagents can provide seeds or surfaces for crystal growth, in addition to promoting a slow reaction rate by limiting nucleation sites, as single crystals are often desired in new MOF syntheses. Reactions are typically carried out in closed systems, and often utilize ‘Parr’ reactors (bombs), especially in the case of reaction temperatures exceeding the boiling point of chosen solvents. Scintillation vials are another common vessel used in MOF preparation, but are not as air-tight as bomb reactors and as such are more suited for when reaction temperatures are lower than solvent boiling points.

One of the most significant synthetic challenges in developing new metal-organic frameworks is obtaining single crystals suitable for X-ray diffraction studies. X-ray diffraction (XRD) remains the primary method used to determine the underlying crystal structure of crystalline materials and will be discussed in more detail in the proceeding sections. Optimizing synthetic temperature, reaction time, solvent type, and reactant stoichiometry are the keys to growing crystals suitable for diffraction studies. Synthetic temperatures are determined experimentally on a trial-and-error basis for high-quality crystal growth. Reported temperatures for a given metal-solvent combination commonly act as convenient starting points for new MOF synthesis. As an example, single crystals of Zr based MOFs prepared in DMF are often

synthesized between 100 - 120 °C, while single crystals of Bi MOFs in DMF are obtained from 80 - 100 °C. Generally speaking, the lower boundary of suitable reaction temperature ranges will yield larger crystal sizes by slowing the motion of reactant molecules, thereby reducing intermolecular collisions and producing fewer nucleation sites. Reaction times vary amongst MOF species and range anywhere from a few hours to multiple days.

1.2.3 Modulated Synthesis

MOFs comprised of high-valence metals are known for being especially difficult to grow single crystals of. This specifically refers to periodic table groups 4, 5, and 6, and includes a few other post-transition metals, such as Al and Bi. These metals have a tendency to hydrolyze easily forming strong, highly polarized bonds with oxygen. This characteristic renders them highly reactive under typical synthetic conditions resulting in a high degree of nucleation sites and thus forming fine powders (often amorphous) or undesired metal-oxides and -hydroxides. For the same reason, carboxylate-based MOFs grown of these species are typically more chemically robust and are often stable under aqueous and even sometimes highly acidic conditions, making them high sought-after variants. While MOFs based on mid to late transition metals (groups 7-12) can be easier to obtain single crystals of, they also often suffer from poor water stability, limiting their applicability to non-aqueous environments.

The use of competing monodentate carboxylic acids (benzoic acid, acetic acid, formic acid, etc.) has proven an invaluable method to obtain single crystals of multivalent metals. This technique was originally reported by Susumu Kitagawa and coworkers in 2009 and termed as ‘modulated synthesis’.²⁵ Soon thereafter, the method was successfully applied to the growth of Zr MOFs, which until that point had relied heavily on Rietveld powder refinement for structural determination.²⁶ The mechanism of action is two-fold. First, introducing a ligand with a single coordination site slows crystal growth by competing with linkers for coordination to the metal nodes; the overall process can be thought of as a ligand-exchange mechanism (Figure 1.5).

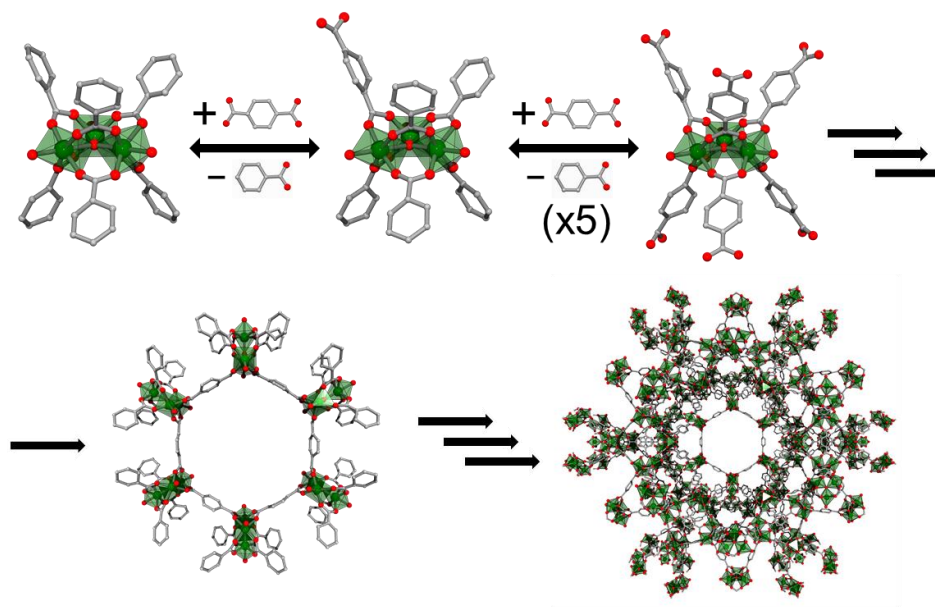


Figure 1.5. Conceptual illustration of the ligand exchange mechanism and possible synthetic intermediates during MOF synthesis using benzoic acid as a modulator.

Second, increasing proton concentration in solution via additional carboxylic acid decreases the quantity of deprotonated linkers at a given time, thereby slowing metal-linker coordination bond formation. It has also been demonstrated that this method can induce crystal defects via linker vacancies, whose positions are occupied by the modulating acid.²⁷ This may be a desirable phenomenon as it allows for further crystal engineering control. Linker defects can produce increased porosity and installation sites for post-synthesis modification, such as anchoring additional metal ions to the SBU.

1.2.4 Crystal Structure and Porosity Characterization

The primary method of structure determination for MOFs is single-crystal X-ray diffraction (XRD). Generally, high quality crystals with lengths of about 10 μm are suitable for XRD. Besides providing atomic coordinates, XRD measurements can be used to generate simulated powder diffraction patterns, which are used as a virtual fingerprint to confirm structural

identity/integrity via powder X-ray diffraction (PXRD) measurements. Conveniently, PXRD does not have the same crystal size or quality requirements as XRD, and is used almost exclusively to confirm structural identities and phase purity once the initial structure has been solved. Powder diffraction patterns appear as a series of lines or peaks occurring at diffraction angles, two-theta, corresponding to constructive interference of incident monochromatic X-rays with the sample when Bragg's Law is satisfied ($n\lambda = 2d \sin \theta$). This law relates the wavelength of incident X-rays (λ) with diffraction angles ($\sin \theta$) and lattice spacing (d) of a sample. In the event that single crystals of a given sample are unobtainable, a technique known as Rietveld powder refinement can be used to determine the crystal structure from a powder diffraction pattern. This method uses a least squares approach to produce a theoretical line profile that is matched with the powder diffraction pattern through trial and error.²⁸

Many of the potential applications of MOFs rely upon their permanent porosity. Paired with the crystal structure, thermogravimetric analysis (TGA) and gas adsorption measurements are often sufficient for full porosity characterization. TGA measurements rely upon a microbalance embedded within a furnace to measure the weight loss of a sample as it is gradually heated to a predetermined temperature; the resulting data is plotted as percent weight loss vs. temperature. This data provides the temperature required to remove the synthesis solvent from within the pores, known as 'activation', which is a critical step for many applications to make use of the materials' porosity.²⁹ It is worth noting that synthesis solvents with relatively high boiling points, such as DMF (153°C) and DMA and (165 °C), often cannot be outgassed directly without causing structural degradation, and require 'solvent exchange' with a more volatile solvent, such as MeOH or MeCN. Heating under dynamic vacuum can also assist with full solvent removal. Additionally, TGA data also indicates the thermal stability of the MOF, which varies amongst species, but is usually in the range of 250 – 450 °C.

Gas adsorption experiments are used to record ‘isotherms’ of microporous (< 2 nm) and mesoporous (2 > 50 nm) materials. According to IUPAC nomenclature, there are 6 different types of isotherms (Type I-VI) representing different adsorbent-adsorbate interactions, and are shown as a plot of gas uptake vs. partial pressure at a given temperature.³⁰ Following activation by heating under dynamic vacuum to completely outgas the sample, adsorption-desorption isotherms are recorded using some inert ideal gas, such as N₂ at 77 K. BET or Langmuir theories are then applied, typically by accompanying computer software, to calculate the internal surface area, pore volume, and pore size distribution.

1.3 MOFs for Catalytic and Luminescent Applications

Generally speaking, MOFs have enormous potential for numerous applications. Their SBUs can be viewed as metal-oxide nanoparticles that are spatially fixed in a porous network, providing substrate access to each metal center, assuming appropriate pore architecture for guest entry. The same is true of utilizing the organic linkers as functional sites. By nature, the pore walls of MOFs are comprised of spatially isolated organic linkers, potentially providing access to each molecule. This is a significant advantage over traditional solids for host-guest applications, such as molecular sensing or catalysis, as most solid species have densely packed structures whose bulk are inaccessible to guest molecules, thereby relying on surface sites for activity.

MOF SBUs commonly contain OMSs that many researchers seek to make use of for catalysis.³¹ These sites are generally occupied by terminal solvent molecules that can be removed through thermal activation at a specific temperature (which can be accelerated via use of dynamic vacuum), while maintaining structural integrity. In terms of catalyst design, SBUs with pre-established OMSs may be targeted during MOF synthesis. Two such examples include as the well-known trinuclear basic metal acetate [M₃O(CO₂)₆L₃] and dinuclear ‘paddlewheel’ [M₂(CO₂)₄L₂] clusters (where L = terminal solvent ligands and CO₂ = linker carboxylates) (Figure

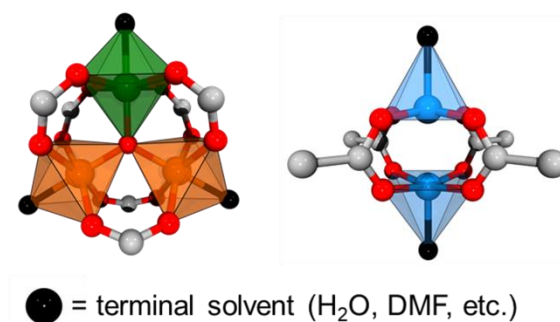


Figure 1.6. Structure plots of trinuclear basic metal acetate $[M_3O(CO_2)_6L_3]$ and dinuclear ‘paddlewheel’ $[M_2(CO_2)_4L_2]$ SBUs containing OMSs.

1.6).³²⁻³³ In fact, it was recently demonstrated by Zhou et al. that trinuclear basic metal acetate clusters may be used directly to form MOFs through a ligand exchange mechanism between capping and bridging ligands.³⁴ Our recent work has also shown that frameworks containing Bi^{3+} PBUs can also be expected to contain OMSs occupied by terminal solvent molecules.³⁵ These Bi^{3+} PBUs tend to coordinate to 4 carboxylates (8 oxygen atoms), but have an overall coordination number of 9, resulting in terminal solvent molecule occupancy of the free site. Additionally, because of their stereoscopic pair of $6s^2$ electrons, the PBU’s coordination geometry tends to be hemidirected, resulting in a large accessible area for guest interaction.

MOF linkers provide an auxiliary method to install OMSs and molecular catalysts. As an example, Lin and coworkers prepared photocatalysts for CO_2 reduction, water splitting, and organic transformations by doping 2,2'-bipyridine-5,5'-dicarboxylic acid (dc bpy) containing known molecular Ir and Re catalysts into the structure of UiO-67.³⁶ This same strategy was used by Cohen et al. to dope the $Mn(bpydc)(CO)_3Br$ ($bpydc = 5,5'$ -dicarboxylate-2,2'-bipyridine) CO_2 reduction catalyst into the same structure.³⁷ MOFs catalysts incorporating porphyrin derivative linkers are also quite popular. These heme-like molecules contain four nitrogen LBSs at their core, two of which contain acidic protons. Upon deprotonation, the core can adopt a 2- state allowing for the insertion of 2+ and 3+ transition metals; in the case of 3+ metals, an

accompanying anion acts to balance the net positive charge. Two obvious pathways exist to utilize porphyrin in the construction of MOF catalysts (Figure 1.7). When metallated with Fe^{3+} , Co^{2+} , and Cu^{2+} , porphyrin MOFs have been shown to have both photo- and electrocatalytic activity towards CO_2 reduction.³⁸⁻⁴¹ Alternatively, the non-metallated tcpp linker can serve as a light-harvesting unit to sensitize MOF PBUs and SBUs for photocatalysis, as was demonstrated in the case of PCN-222 for CO_2 reduction.⁴² In this scenario, absorption of visible light generates a $\pi \rightarrow \pi^*$ transition within the ligand, followed by electron transfer to the metal building unit, thereby generating a reduced metal species capable of reduction chemistry. In these systems, sacrificial reducing agents such as triethanolamine (TEOA) or triethylamine (TEA) are used to replenish the electrons lost by the ligand.

Ligand functionality is the primary way to design luminescent MOFs (LMOFs).⁴³ When paired with appropriate metals, fluorophore ligands often maintain or experience enhancement of their optical properties by limiting molecular vibrations and rotations, and thereby reducing non-

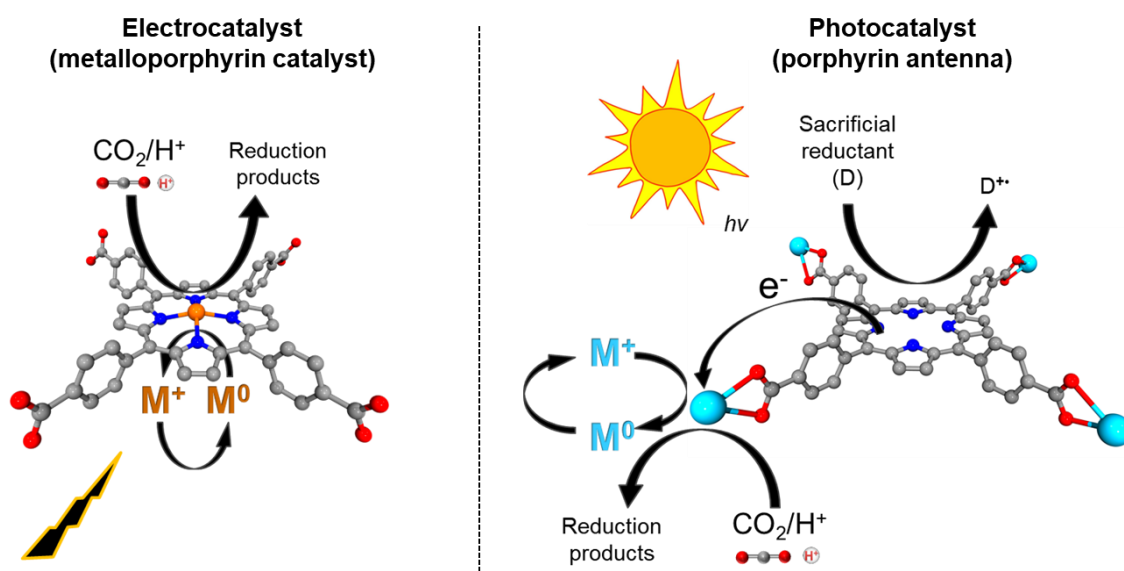


Figure 1.7. Conceptual illustration of the two main pathways for utilizing porphyrin in the construction of a MOF CO_2 reduction catalyst.

radiative decay pathways. Typically d^{10} metals (Zn^{2+} and Cd^{2+}) are chosen for these types of materials as they do not undergo LMCT (ligand-to-metal charge transfer), which is the most common pathway for emission quenching in MOFs. Our group work has demonstrated that incorporation of aggregation induced emission (AIE) ligands based on the tetraphenylethylene (tpe) core (Figure 1.8a) into MOF structures can significantly enhance the fluorescence quantum yields.⁴⁴⁻⁴⁵ These LMOFs were shown to have significant potential to serve as phosphors for general lighting applications. Additionally, because MOFs often contain open pore systems, guest molecules of appropriate size can freely enter the framework and interact with these fluorophores resulting in perturbation of the optical signal, which is the basis for luminescent sensing applications (Figure 1.8b).⁴⁶ In an optimized MOF sensing platform, the fluorescent ligand should be easily accessible to guest analyte molecules and should be designed in such a way as to promote selective analyte-linker interactions. Besides linker based MOF luminescence, metal centers can also act as the primary luminescent component. The most common method to design metal-based luminescent MOFs is to sensitize lanthanide atoms via antenna linkers.⁴⁷ These MOFs often demonstrate interesting luminescent properties, and have been reported as

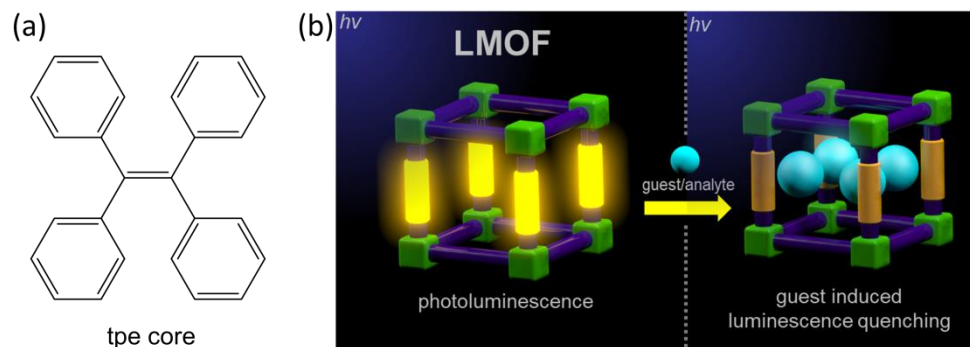


Figure 1.8. (a) AIE fluorophore tetraphenylethylene (tpe). (b) Conceptual illustration of ligand-based luminescence and guest induced quenching.

both chemical and temperature luminescent sensing materials.

Porphyrin based MOFs also make for highly sensitive optical sensing platforms. Upon photoexcitation, the porphyrin macrocycle undergoes both S_2 and S_1 transitions from a doubly-degenerate set of HOMOs and LUMOs resulting in a characteristic UV-Vis Soret band occurring at ~450 nm, and four smaller Q bands in the range of 500-700 nm.⁴⁸ It is well documented that even minor perturbation of this conjugated π system results in significant changes to the molecules optical properties. Traditionally, these sensitive optical signals are exploited by dissolving molecular porphyrin species in an appropriate solvent with an analyte of interest.⁴⁹ Accessibility of the porphyrin core is hindered when the ligand is in the solid state as only the outer surface of the solid particles are available for guest interactions. Conversely, our work has shown that incorporation into an appropriate porous MOF structure allows for molecular level sensitivity to be maintained in the solid state owing to the pore system providing guest access to the majority of the porphyrin molecules.⁵⁰

The following dissertation work began primarily as a study of MOFs for water for CO_2 reduction and water splitting catalysis, however this is a new area of research for the Li group, requiring a significant time investment to establish methods, instrumentation, and best practices for such a study. The sensing and luminescent work was chosen an auxiliary project and is traditionally the main focus of the Li group, hence, the disparate nature of the dissertation.

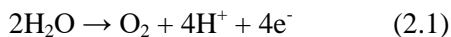
CHAPTER 2. Surface and Structural Investigation of MnO_x Birnessite-type Water

Oxidation Catalyst Formed under Photocatalytic Conditions ⁵¹

[*Chem. Eur. J.* **2015**, 21,14218 –14228]:*Project coauthored by Jingming Zhang; Appendix I

2.1 Introduction

Solar energy is one of the most abundant renewable energy resources available, and is therefore considered to be a key element for energy sustainability. Hydrogen produced from solar driven water splitting poses a particularly attractive alternative to fossil fuels due to the availability of water and solar resources. The overall water splitting reaction is comprised of two half-reactions: water oxidation (O₂ evolution reaction, OER) and proton reduction (H₂ evolution reaction, HER), where the former half generates protons and electrons for the latter half. Thermodynamic and kinetic limitations make the oxidation half-reaction the bottleneck of the overall process, which requires two water molecules and a four electron oxidation; a minimum potential of 1.23 V vs NHE at pH 0 is needed to drive this reaction (eqn. 1).⁵²⁻⁵⁶



Pt, Ru, and Ir based materials have proven effective as water oxidation catalysts (WOCs), however their low abundance and subsequent high cost make them ill-suited for widespread application.⁵⁷⁻⁶¹ With this in mind, catalysts based on common transition metals, such as Mn, Fe, Co, Ni, and Cu, are attractive alternatives. Of these, Manganese is of particular interest; for the past few decades immense effort has been spent resolving the structure and OER mechanism of the naturally occurring Photosystem II (PSII) oxygen evolving complex (OEC), “hetero-cubic” CaMn₄O₅.⁶²⁻⁶³ Various Mn-oxides and multinuclear Mn-complexes have been studied, with special attention paid to materials containing OEC-like structural motifs.⁶⁴⁻⁷⁹ Despite these efforts, few Mn complexes have proven themselves as stable WOCs,⁵⁵ however several polymorphs of Mn-oxide are known to be active. Our previous work tested a number of

crystalline Mn-oxide phases under photochemical conditions, which may reflect possible performance in a photochemical cell.⁷¹ Our initial results have shown Mn_2O_3 , Mn_3O_4 , and λ - MnO_2 (spinel) as active when driven by photogenerated $[\text{Ru}(\text{bpy})_3]^{3+}$. Activity from these materials trends with flexible Mn^{3+} features, such as long Mn-Mn distances and weak Mn-O bonds.

Some birnessite MnO_2 polymorphs have also been reported as active, but frequently under alternate conditions.^{64-69, 80-85} Birnessite is a hydrated lamellar phyllosilicate comprised of negatively charged sheets of edge-sharing MnO_6 octahedra and $\sim 7 \text{ \AA}$ periodicity from layer to layer (Figure 1d).⁸⁶⁻⁸⁷ The negative charge arises from either the presence of Mn^{3+} atoms within the octahedral layer ($\text{Mn}_{\text{layer}}^{3+}$, triclinic- or monoclinic-type) when formed under alkaline conditions, or $\text{Mn}_{\text{layer}}^{4+}$ vacancies (hexagonal-type), which is typically formed under acidic conditions. Triclinic-type is generally charge balanced by interlayer cations (Na^+ , K^+ , Mg^{2+} , Ca^{2+} , Sr^{2+} , etc.) and hexagonal-type by Mn^{3+} triple corner sharing octahedra above or below the layer vacancy ($\text{Mn}_{\text{interlayer}}^{3+}$).⁸⁸⁻⁹³ Trends in catalytic activity have been correlated to degree of disorder (higher disorder usually resulting in higher activity), structure flexibility, and interlayer species, with Ca^{2+} birnessites showing some of the highest levels of activity by Kurz et al.^{67, 69, 94} It has been suggested by Suib et al. that activity in birnessites may correspond to interlayer/surface Mn^{3+} bound above and below vacancies.⁶⁸ Notably, the specific structural polytype is rarely discussed in context of performance, likely owing to birnessites' intrinsic poor crystallinity, structural disorder, and small particle sizes, thereby complicating unambiguous characterization.⁶⁷ That fact that these materials readily undergo structural changes in response to solution pH further complicates structural analysis. Cerium (IV) ammonium ammonium nitrate (CAN) solution is commonly employed as sacrificial chemical oxidant to evaluate birnessite OER catalysts, but has an intrinsically low pH (~ 1).^{66-67, 69} As documented, birnessite is well known to

transition from the triclinic to hexagonal phase under \sim pH 5, which is virtually undetectable to most analytical methods.⁹¹⁻⁹³

Recent literature has focused upon the transformation of molecular Mn species into amorphous MnO_x during CAN oxidant and electrochemically driven water oxidation. The active species has been loosely characterized as birnessite-like based on bonding features present in extended X-ray absorption fine structure (EXAFS) studies. However, structural characterization is limited by the necessary use of support materials, such as clay in the case of CAN reactions, and Nafion in electrocatalytic systems.⁹⁵⁻⁹⁷ Recently, Driess, Dau and coworkers studied the formation of an amorphous MnO_x catalyst through partial corrosion of a support-free crystalline MnO precursor.⁹⁸⁻⁹⁹ The resulting MnO_x was found to be active under both CAN and photochemical conditions, however the former was required to oxidize the MnO to MnO_x and generate an active phase. Because the precursor is only partially oxidized, a heterogeneous material very high in Mn^{2+} content was obtained (average oxidation state of Mn reported as 2.5). It is worth noting that recently the solution structure and role of CAN as a one-electron outer sphere oxidant has been called into question, prompting us to limit the current study to photocatalytic conditions.¹⁰⁰

Metal-organic frameworks (MOFs) are an emerging class of materials comprised of crystalline coordination networks between metal ions and organic linkers, and have been demonstrated as important candidates for multiple applications.^{36, 43, 50, 101-107} By utilizing an $\text{Mn}^{\text{II}}_4\text{O}_4$ based MOF precursor approach, we show for the first time that MnO_x catalysts form under photochemical water oxidation conditions and without the use of support material. Highly active discrete MnO_x particles ($^4\text{MnO}_x$) were isolated that can be best described as resembling hexagonal-type birnessite. We compare our results to amorphous precipitate formed from Mn^{2+} salt ($^s\text{MnO}_x$) under the same conditions, as well as crystalline hexagonal K^+ birnessite (HexBir). Bulk characterization of the catalysts was carried out using powder X-ray diffraction (PXRD) and

X-ray photoelectron spectroscopy (XPS) was used to investigate the active surfaces. Additional detailed structural analysis was performed on the most active catalyst, ${}^4\text{MnO}_x$, using high energy synchrotron X-ray diffraction with pair distribution function (PDF) analysis, Raman spectroscopy, and high-resolution transmission electron microscopy (HR-TEM).

2.2 Experimental Details

All chemical reactants used for this study were purchased from commercial sources and used without further purification: acetonitrile (99.998%) from Acros; manganese (II) perchlorate hexahydrate ($\geq 99\%$), nicotinic acid (99%), and sodium hydrogen carbonate ($\geq 99.7\%$) from Alfa Aesar; conc. nitric acid from Fisher Scientific; sodium persulfate ($\geq 98\%$), tris(2,2'-bipyridine)dichlororuthenium (II) hexahydrate (99.95%), potassium permanganate ($\geq 99\%$), Manganese(II) sulfate monohydrate ($\geq 99\%$) and methanol ($\geq 99.8\%$) from Sigma-Aldrich.

2.2.1 Material Synthesis

Crystalline $\text{Mn}_4(\mu_3\text{-OMe})_4(\text{nic})_4$ (nic = nicotinate) was obtained using a reported method.¹⁰⁸ $\text{Mn}(\text{ClO}_4)_2 \cdot 6\text{H}_2\text{O}$ (0.25 mmol), nicotinic acid (0.5 mmol), MeOH (3 mL), and MeCN (4 mL) were sealed in a teflon-lined bomb reactor and heated from room temperature to 160 °C over four hours, maintained at 160 °C for two days, and slow cooled at a rate of 0.1 °C/min to room temperature. Large amber prism crystals were collected, washed thoroughly with methanol, and air dried (~ 70% yield based on Mn). Hexagonal-type *c*-ordered K^+ birnessite was prepared from the thermal decomposition of KMnO_4 at 800 °C according to the literature procedure.¹⁰⁹⁻¹¹⁰ KMnO_4 (5 g) was heated at 2 °C/min to 800 °C, maintained at 800 °C for 16 h, and cooled at 1 °C/min to room temperature to promote crystallization. The product was washed with Milli-Q water until the filtrate became clear to remove soluble surface species and air dried at room temperature. $\beta\text{-MnO}_2$ (XPS reference material) was prepared as described in our previous work according to a modified reported procedure.^{71, 111} An aqueous solution of $\text{MnSO}_4 \cdot \text{H}_2\text{O}$ (8 mmol)

and $\text{Na}_2\text{S}_2\text{O}_8$ (8 mmol) was heated in a stainless steel reactor with a Teflon liner at 120 °C for 12 h. The resulting product was centrifuged, decanted and washed with deionized H_2O and dried at 90 °C in air. Mn_2O_3 impurity and was further purified by adding 1g of initial product to 2 mmol of $\text{Na}_2\text{S}_2\text{O}_8$ dissolved in 25 ml H_2O . The slurry was placed in a stainless steel reactor with a Teflon liner at 120 °C for 12 h. The resulting material was determined to be homogeneous phase with less than 3% impurity by slow scan PXRD.

Conversion from Mn_4 -MOF to birnessite-type $^4\text{MnO}_x$ was first noted when Mn_4 -MOF was evaluated for photochemical WOC activity. Following this initial experiment, $^4\text{MnO}_x$ was synthesized directly *via* decomposition of Mn_4 -MOF. ~ 10 mg of Mn_4 -MOF was added to a 20 mL vial containing 10 mL pH 7 bicarbonate buffer solution (0.1 M, adjusted with ~ 4M HNO_3) with 0.5 mM $\text{Ru}(\text{bpy})_3\text{Cl}_2 \cdot 6\text{H}_2\text{O}$ (photosensitizer) and 20 mM $\text{Na}_2\text{S}_2\text{O}_8$ (electron scavenger). The vial was then illuminated with four white LEDs (see Figure S1 for illumination profile) under constant magnetic stirring at room temperature. Within one minute of illumination, a solution colour change from orange to brown was observed indicating light-induced conversion. After one hour of reaction time, the reaction suspension was centrifuged, washed with DI water to remove any surface adsorbed impurities, and left to air dry under ambient lab conditions. Conversion from Mn^{2+} salt to birnessite-type $^5\text{MnO}_x$ was performed in an identical manner as $^4\text{MnO}_x$, except that stoichiometric quantities of the constituents within the MOF were used in its place, with nicotinic acid (6.2 mg) substituting for the linker and $\text{Mn}(\text{ClO}_4)_2 \cdot 6\text{H}_2\text{O}$ (18.2 mg) acting as the Mn source. These reactions were later scaled up directly to obtain enough material to carry out additional measurements.

2.2.2 Photochemical Reactions

Photochemical water oxidation reactions were conducted in a headspace-free 2 mL quartz reaction chamber surrounded by a circulating water jacket maintained at 20 °C. For a typical reaction, 1 mL of 250 ppm catalyst suspension in pH 7 NaHCO_3 (or 2200 ppm in the case of the

high loading experiment) was injected into the photoassay chamber containing 1 mL of buffer, 1.0 mM $\text{Ru}(\text{bpy})_3\text{Cl}_2 \cdot 6\text{H}_2\text{O}$ (photosensitizer, 0.5 mM concentration after dilution from catalyst suspension) and 20 mM $\text{Na}_2\text{S}_2\text{O}_8$ (electron scavenger, 10 mM total concentration after dilution). After establishing a stable baseline for two minutes in both N_2 purged and non-purged systems, the reactions were illuminated by four white LEDs as described above and dissolved O_2 concentrations were measured with a Clark-type electrode (Hansatek Ltd), which was calibrated with both sodium dithionate and N_2 purged solutions daily.

2.2.3 Instrumental Details

Gas chromatography

The long-term stability and catalytic nature of $^4\text{MnO}_x$ was confirmed by gas chromatography (GC). Data was recorded using an Agilent 6890N GC, equipped with a 30 m, 0.53 mm ID, 50 μm Rt-Msieve 5A capillary column and thermal conductivity detector (TCD). In a 23 mL crimp-cap septum-sealed glass vial, 150 ppm (1.5 mg) $^4\text{MnO}_x$ was added into 10 mL of pH 7 bicarbonate buffer (0.1 M, adjusted with HNO_3) containing 0.5 mM $\text{Ru}(\text{bpy})_3\text{Cl}_2 \cdot 6\text{H}_2\text{O}$ and 20 mM $\text{Na}_2\text{S}_2\text{O}_8$. While remaining covered with aluminium foil to inhibit the photoreaction, the solution was purged with He for 5 mins followed by illumination for 1 hour under magnetic stirring at room temperature (monitored by a laser thermometer at $\sim 24^\circ\text{C}$); 10 μL manual headspace aliquots were injected into the GC. After each reaction the catalyst was recovered by centrifugation, washed with DI water three times and transferred to a fresh aluminium foil covered reaction vial using 10 mL of NaHCO_3 buffer to prevent loss of catalyst. $\text{Ru}(\text{bpy})_3\text{Cl}_2 \cdot 6\text{H}_2\text{O}$ and $\text{Na}_2\text{S}_2\text{O}_8$ were added to the vial in the same concentration as for the first trial and sonicated to aid dissolution. The vial was then purged and illuminated for an additional hour. This process was repeated for six cycles.

Powder X-ray diffraction

PXRD patterns were recorded on a Rigaku Ultima IV X-ray diffractometer, using Cu K α radiation ($\lambda = 1.5406 \text{ \AA}$). A graphite monochromator was used and the generator power settings were set to 40 kV and 44 mA. Data were collected between 2θ of $3\text{--}50^\circ$ with a step size of 0.02° and a scan speed of 1.5 deg/min .

N₂ sorption measurements

BET surface area measurements were made by N₂ gas adsorption at 77K on a volumetric gas sorption analyzer (Autosorb-1 MP, Quantachrome Instruments). ~ 100 mg of sample was prepared by outgassing under vacuum at 120°C overnight.

Inductively-coupled plasma optical emission spectroscopy

Catalyst leaching was determined by ICP-OES using a SPECTRO ARCOS EOP ICP: 150 ppm of ⁴MnO_x was added to a 23 mL sealed vial containing 0.5 mM Ru(bpy)₃Cl₂·6H₂O and 20 mM Na₂S₂O₈ in 10 mL of pH 7 bicarbonate buffer. After two hours of illumination the catalyst was removed from the solution by centrifugation. The resulting supernatant was collected and diluted to 20 mL with DI water. An aliquot of the solution was then acidified with nitric acid (2%) and injected into the instrument.

X-ray photoelectron spectroscopy

A Thermo K-Alpha XPS was used with charge compensation to measure the surface elemental composition of the catalysts. Solid samples were fixed on carbon tape and a beam of $150 \text{ }\mu\text{m}$ diameter was focused on an area covered by the powdered sample. In order to deconvolute the Mn 2p_{3/2} spectra, we followed the precedent set by Nesbitt and Banerjee, which are based on free ion calculations reported by Gupta and Sen.¹¹²⁻¹¹³ Each oxidation state of Mn results in a set of five multiplets (15 total); relative peak intensities and differences in binding energies ($\Delta \text{ eV}$) from peak to peak were set as fixed values (the highest energy multiplet of Mn⁴⁺ was allowed variable intensity) based on the values used in their study and those calculated by

Gupta and Sen. The lowest energy Mn^{4+} multiplet was used as a reference point to set the binding energy of the lowest energy Mn^{3+} and Mn^{2+} multiplets at fixed values. The other four higher energy multiplets of each group were set at a specific Δ eV from the lowest energy peaks, but were allowed a 0.2 eV variance. These same Δ eV values were used for each sample measured. The full widths at half max (FWHM) were constrained to a specific value for each sample (30% Lorentzian/70% Gaussian), ranging from 1.16 eV to 1.23 eV. The initial peak position for Mn^{4+} was determined from our reference sample, $\beta\text{-MnO}_2$, and the O1s spectra peak maxima was used to calibrate the Mn^{4+} position for the other samples. Survey scans were also taken for each sample and suggest overall MnO_2 stoichiometry in each case – the excess oxygen in HexBir AR likely arises from incomplete washing and the presence of CO_3^{2-} , as suggested by the abundance of carbon present.

Synchrotron powder X-ray diffraction and pair distribution function analysis

High energy X-ray scattering data suitable for PDF analysis was collected on beamline 11-ID-B at the Advanced Photon Source (APS) at Argonne National Laboratory. Dried samples were contained within polyimide capillaries of ~ 1 mm diameter. Monochromatic X-rays ($\lambda = 0.2128$ Å, ~ 58 keV) were combined with a large Perkin-Elmer amorphous silicon-based area detector to collect data to high value of momentum transfer (Q). The two dimensional scattering images were reduced to one dimensional intensity data as a function of scattering angle within fit2D. The PDFs were extracted within PDFgetX2 using data up to $Q_{\text{max}} = 23$ Å⁻¹ and were corrected for background scattering, Compton scattering, and oblique incidence. The PDF data was fit within PDFgui by a real space structural model corresponding to a monoclinic birnessite structure ($R \sim 27\%$; $C2/m$; $a = 4.97$ Å, $b = 2.84$ Å, $c = 7.29$ Å; $\beta = 98.7^\circ$).¹¹⁴ The lattice parameters, atomic positions (as constrained by the $C2/m$ symmetry) and atomic displacement parameters for the model MnO_2 layers were structurally refined using a large value of the atomic displacement parameter normal to the layer direction (U_{33}); U_{33} was constrained to be a factor of

20 times larger than $U_{11} = U_{22}$. Maximum particle size was constrained to 50 nm. The original sub-cell used for refinement has the unit cell parameters, $a = 5.175 \text{ \AA}$, $b = 2.850 \text{ \AA}$, $c = 7.337 \text{ \AA}$, $\beta = 103.18^\circ$.

Raman spectroscopy

Raman measurements were collected using a Thermo-Fisher Nicolet Almega XR Dispersive Raman spectrometer equipped with a 50x objective microscope. A 532 nm solid state laser was used for excitation; the output power was reduced to 1% (0.117 mW) and the acquisition time varied from 5 to 10 min to avoid sample decomposition or phase transition induced by laser heating. The spectra were obtained from 50 to 2000 cm^{-1} . For $\text{Mn}_4\text{-MOF}$, the bands at 1595 and 1040 cm^{-1} are due to the $\nu(\text{C}=\text{C})$ and $\beta(\text{C-H})$ vibrations of the ring modes, while the 1397 cm^{-1} band is ascribed to the $\nu_s(\text{COO}^-)$ units coordinated to metal ions in MOF structure. Ring deformation modes δ_{6a} and δ_{6b} are observed at 848 and 614 cm^{-1} , mixed with the $\delta(\text{COO})$ vibration.¹¹⁵⁻¹¹⁶

High-resolution field emission transmission electron microscopy

Particle morphology and lattice images were taken using a JEOL 2010F field emission TEM operating at 200 kV. A suspension of $^4\text{MnO}_x$ in water was sonicated and allowed to stand for 24+ hours. Aliquots were drawn from the top of the vial, diluted with water, and a single droplet was placed onto a carbon coated copper grid and dried under vacuum overnight.

Thermogravimetric Analysis (TGA)

The water content of $^4\text{MnO}_x$ and $^5\text{MnO}_x$ was determined using thermogravimetric analysis. Measurements were performed using a TA Q5000 Thermogravimetric Analyzer with a temperature ramp of 1 $^\circ\text{C}/\text{min}$ from room temperature to 600 $^\circ\text{C}$ under nitrogen gas flow.

2.2.4 Mn content via XPS and TGA data

⁴MnO_x: after XPS deconvolution, the following approximate atomic percentages were obtained: 28.7% Mn, 48.1% O_{MnO}²⁻, 2.9% O_{nic}²⁻, 8.0% OH⁻, 22.9% C, 1.4% N, and 2.1 % Na. The 1.4% N content was used to determine the contribution of C (8.4%) and O (2.8%) from nicotinic acid within the structure. The XPS O1s water contribution was ignored due to the high vacuum conditions, and H₂O_{interlayer} was instead measured using slow ramp (1 °C/min) TGA (Figure 2.0). The ~ 8 % weight loss up to 100 °C is attributed to surface adsorbed water; the approximate amount of H₂O_{interlayer} (weight loss from 100 – 280 °C) is ~ 8 %. Notably, there is an additional 6.6% weight loss at ~ 325 °C likely from nicotinic acid (autoignition temperature ~ 365 °C) and is commensurate with the XPS data (both methods result in ~ 0.05 nic per formula unit. Finally, an approximated structural formula for the material based on this data is: Na⁺_{0.07}MnO_{1.67}(OH)_{0.29} • 0.42 H₂O • 0.05 nic (101.86 g/mol). **⁵MnO_x**: in contrast to ⁴MnO_x, no Na⁺ or N was detected by XPS, indicating that no nicotinic acid or sodium was present within the material. The XPS survey scan results in ~ 24.4% Mn, 53.1% O, and 20.5% carbon, indicating MnO₂ stoichiometry (86.94 g/mol). The TGA data for this sample shows ~ 5% total weight loss up to 300 °C, suggesting minimal interlayer water content. This is consistent with the lack of any ordered stacking observed in the PXRD pattern at 2θ ≈ 12.5° and 25°. There is a weight loss (~ 22%) that begins at about 280 °C, and can possibly be attributed to a phase transformation to a more reduced state coupled with the release of oxygen. **HexBir**: the structural formula was adopted from previous studies: K⁺_{0.231}Mn³⁺_{0.077}(Mn⁴⁺_{0.885} □_{0.115})O₂ • 0.60 H₂O (104.68 g/mol).¹¹⁰

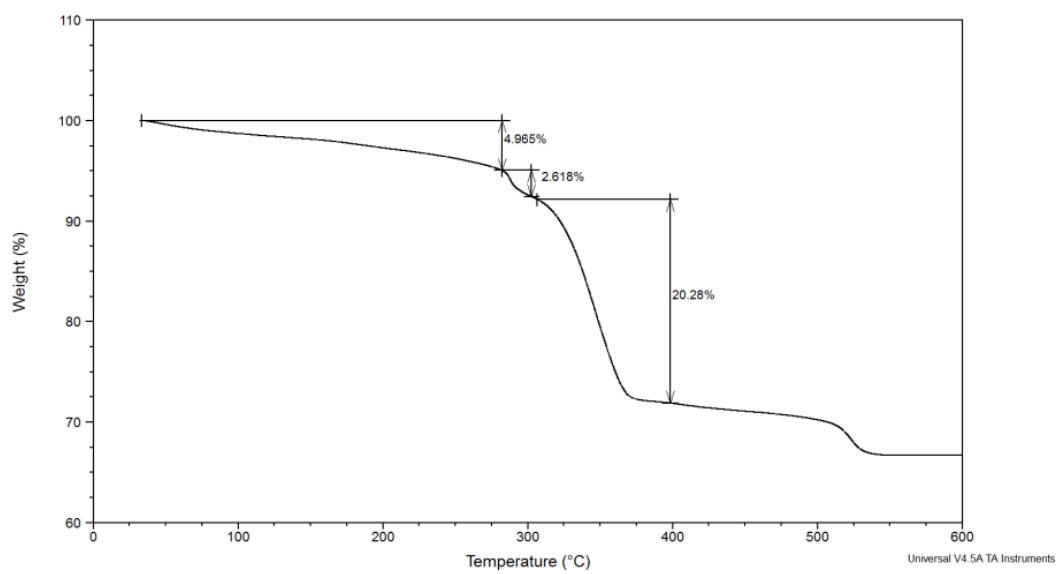
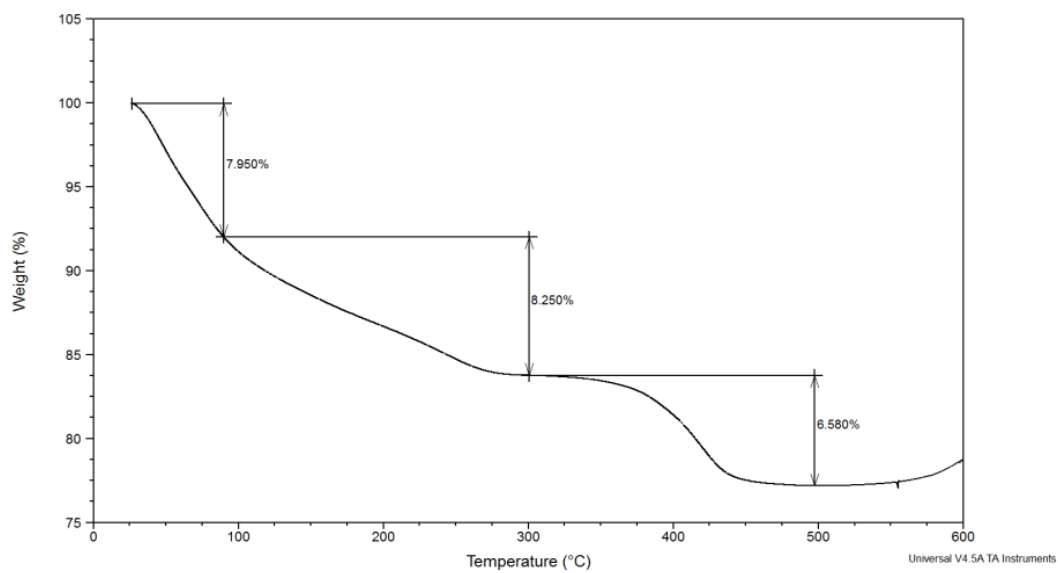


Figure 2.0. TGA curve for ${}^4\text{MnO}_x$ (top) and ${}^5\text{MnO}_x$ (bottom).

2.3 Results and Discussion

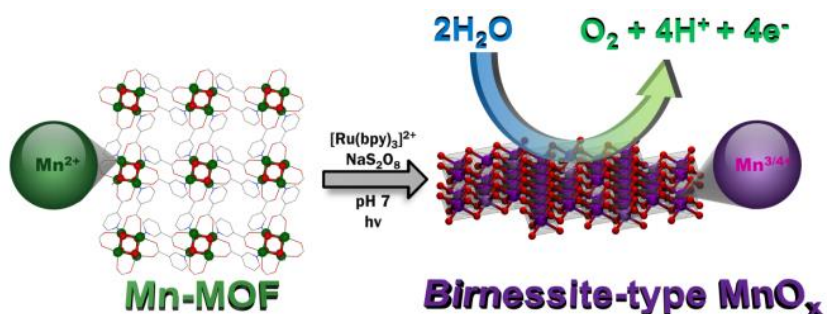


Figure 2.1 Conceptual drawing of the conversion of $\text{Mn}_4(\mu_3\text{-OMe})_4(\text{nic})_4$ to $^4\text{MnO}_x$ with subsequent catalytic water oxidation.

For facile characterization of active Mn-oxides generated *in-situ* during water oxidation, we developed a precursor method employing photocatalytic conditions to convert an Mn^{2+} cube bearing MOF, $\text{Mn}_4(\mu_3\text{-OMe})_4(\text{nic})_4$ ($\text{Mn}_4\text{-MOF}$, nic = nicotinate), to an active MnO_x material (Figure 2.1).¹⁰⁸ Amber crystals of as-synthesized $\text{Mn}_4\text{-MOF}$ were obtained using the reported synthesis method (Figure 2.2a and 2.2c) and phase purity was confirmed *via* PXRD (Figure 2.3a, green trace). The as-made crystals were ground and added to a visible-light driven water oxidation assay using $[\text{Ru}(\text{bpy})_3]^{2+}$ photosensitizer and $\text{Na}_2\text{S}_2\text{O}_8$ sacrificial oxidant in pH 7 NaHCO_3 buffer. O_2 evolution was monitored using a Clark-type electrode and four white LEDs as the light source (see Figure 2.4 for luminescence profile). Upon illumination, the system gradually changed colour from orange to brown and subsequently began generating a significant amount of O_2 after an initial lag period of ~ 1 minute (Figure 2.5a, green trace). The catalyst was recovered by centrifugation, which had changed from amber crystals into black powder termed $^4\text{MnO}_x$ (Figure 2.2b and 2.2d). When the experiment was repeated with $^4\text{MnO}_x$, the same rate of oxygen evolution was measured, except without a significant lag period (Figure 2.5a, black trace). We ascribe the difference in catalytic onset time to the time for conversion of $\text{Mn}_4\text{-MOF}$ to $^4\text{MnO}_x$. Based on these initial results, a scale-up procedure was devised to convert $\text{Mn}_4\text{-MOF}$ into

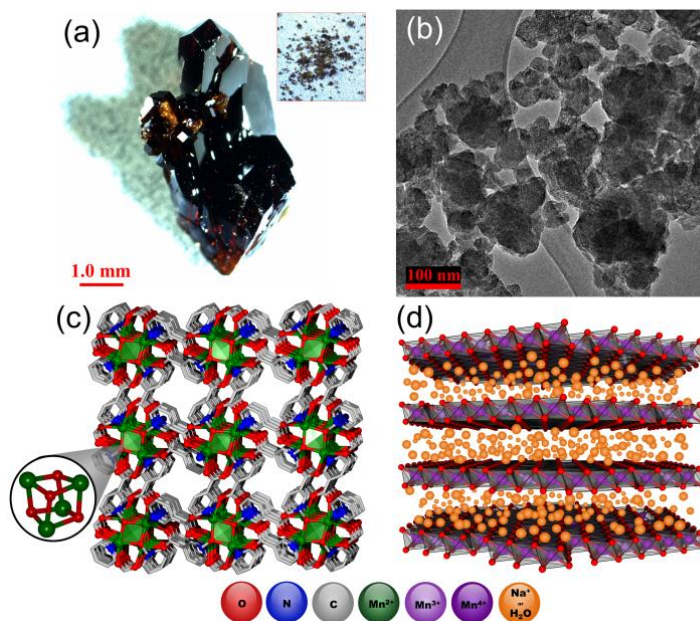


Figure 2.2. (a) Microscope image of as-synthesized $\text{Mn}_4\text{-MOF}$ (inset shows bulk synthesis product, scale = 1.0 mm); (b) zoom out HR-TEM image of catalyst $^4\text{MnO}_x$; (c) structure-plot of $\text{Mn}_4\text{-MOF}$ (green polyhedrons represent cube-shaped SBU); (d) generic conceptual drawing of layered MnO_2 (triclinic-type) with disordered interlayer.

the catalyst particles for further study (see experimental section for details). Initial PXRD analysis revealed that the $\text{Mn}_4\text{-MOF}$ is oxidized to a manganese oxide, characterized by the presence of low intensity broad peaks, indicative of semi-crystallinity and small particle size (Figure 2.3a, black trace). The peaks can be roughly indexed to those of birnessite-type MnO_2 , and look reminiscent of turbostratic-type patterns.⁹³ The peak positions at $\sim 2\theta = 12.5^\circ$ and 25° correlate well to the $00l$ reflections (001 and 002 using a single layer model), while the main peak at 37° can be indexed to 100 layer reflections. The BET surface area of the catalyst was measured to be $216 \text{ m}^2/\text{g}$, which is among the highest reported values for these types of materials and likely contributes to its high performance. When reevaluated in the photoassay using 125 ppm concentration (Figure 2.3b, black trace), an approximate initial O_2 evolution rate of $\sim 0.84 \text{ mmol}$

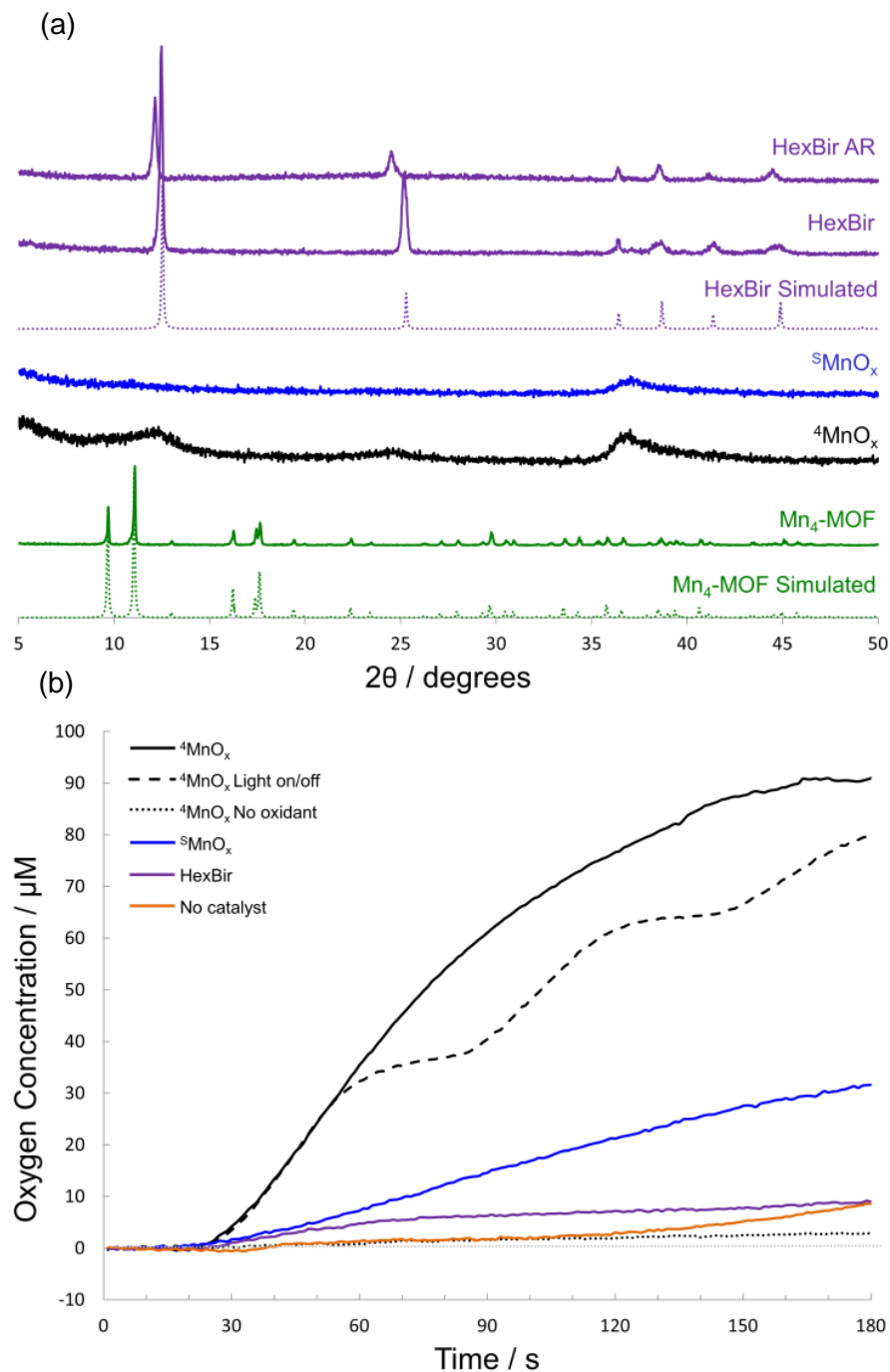


Figure 2.3. (a) Simulated and measured PXRD patterns for $\text{Mn}_4\text{-MOF}$ (green), $^4\text{MnO}_x$ (black), $^5\text{MnO}_x$ (blue), and HexBir (purple). (b) Dissolved oxygen concentration measured by Clark-type electrode at 20 °C using 125 ppm catalyst concentration in 2 mL bicarbonate buffer (pH 7) with 0.5 mM $\text{Ru}(\text{bpy})_3\text{Cl}_2 \cdot 6\text{H}_2\text{O}$ and 10 mM $\text{Na}_2\text{S}_2\text{O}_8$. Illumination begins at time $t \approx 25$ s.

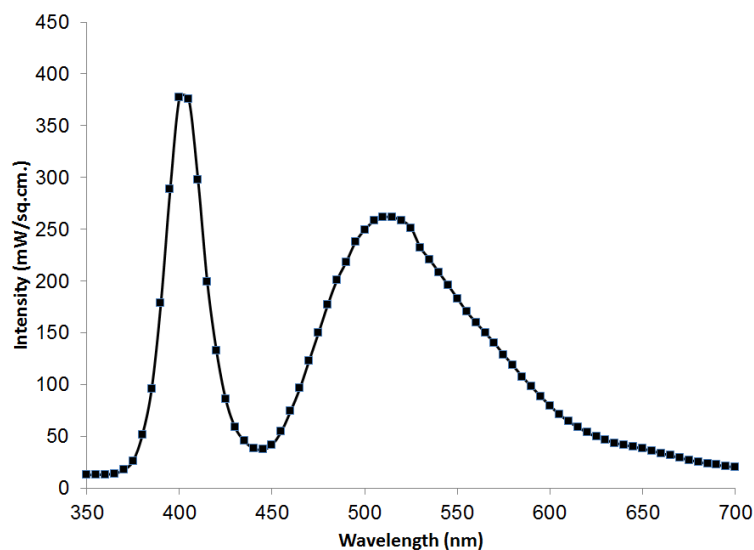


Figure 2.4. Emission profile for the WLED lamps.

O_2 mol $\text{Mn}^{-1} \text{sec}^{-1}$ was calculated based on the slope of the linear region from 30 - 60 (see 2.2.4 for Mn content approximation). We also confirmed the photocatalytic nature of O_2 production by performing intermittent 30 sec exposures to the light source. In the absence of light the O_2 curve leveled off, which was recovered by turning the lights back on again (Figure 2.3b, dashed trace). In the absence of $[\text{Ru}(\text{bpy})_3]^{2+}/\text{S}_2\text{O}_8^{2-}$, little to no oxygen was generated (Figure 2b, dotted trace). Further experiments were performed in the absence of catalyst. The system was nitrogen purged and the Clark electrode showed minimal O_2 production (Figure 2.5b, orange trace). Our previous work has shown that in the absence of catalyst in unpurged $[\text{Ru}(\text{bpy})_3]^{2+}/\text{S}_2\text{O}_8^{2-}$ systems, an O_2 consumption trace results that is ascribed to oxidation of $[\text{Ru}(\text{bpy})_3]^{3+}$.¹¹⁷ However, the presence of an active catalyst helps to inhibit the decomposition of the photosensitizer, as previously described by Hill and coworkers.¹¹⁸ To confirm these findings, reactions for $^4\text{MnO}_x$ were performed in both purged and unpurged solutions (Figure 2.5b). Similar results were obtained for both measurements, confirming that oxygen consumption *via* $[\text{Ru}(\text{bpy})_3]^{3+}$ oxidation is negligible in the presence of an active species.

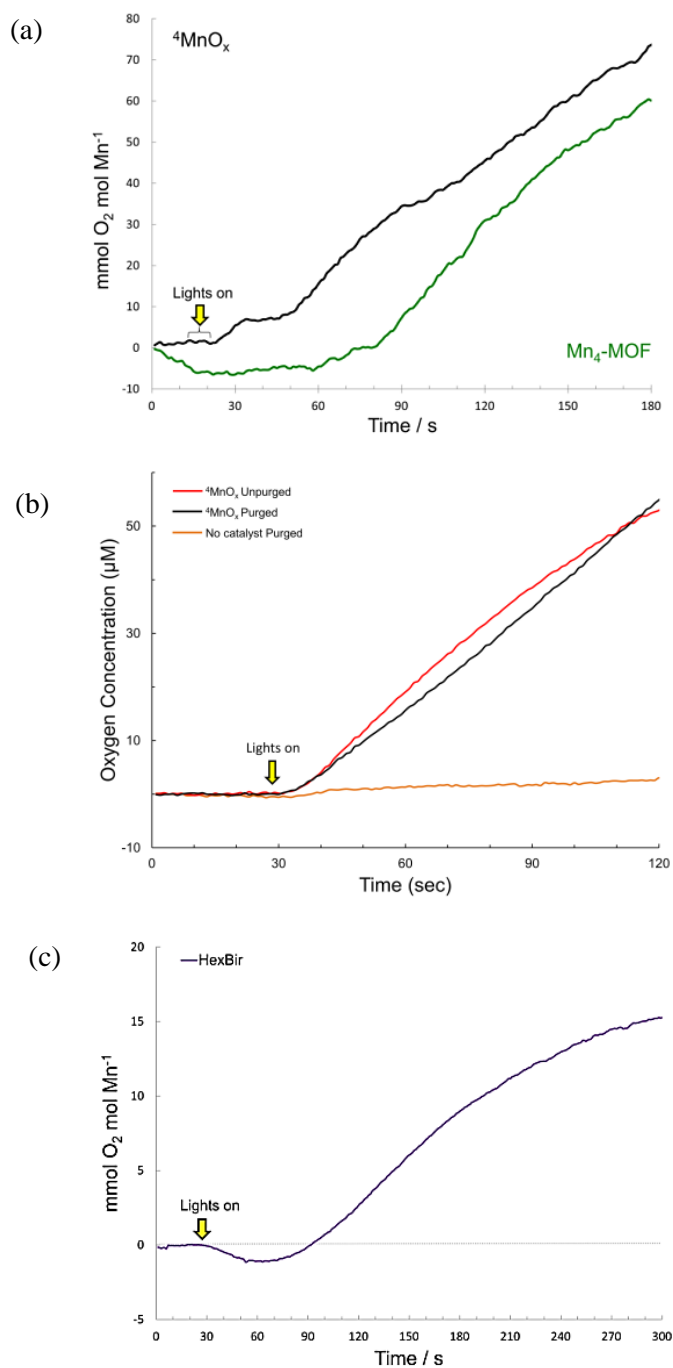


Figure 2.5. Dissolved oxygen concentration measured by Clark-type electrode at 20 °C in 2 mL pH 7 bicarbonate buffer. (a) 100 ppm of $\text{Mn}_4\text{-MOF}$ (green) and 50 ppm of 4MnO_x (black). (b) ~100 ppm of 4MnO_x in purged (black) and unpurged (red) solution. (c) 1100 ppm of HexBir (purple).

The long term stability and catalytic nature of ${}^4\text{MnO}_x$ was confirmed by performing six sequential one hour long reactions monitored by gas chromatography (GC) using 150 ppm of catalyst, which was recovered and reused for each trial (see experimental section for details). It is known that this system is not suitable for determining long term catalytic performance due to sacrificial reagent degradation, however we employed this method to confirm that the catalyst does not deactivate under these conditions. Virtually the same amount of O_2 was produced in each trial (1st = 0.0060 mmol, 6th = 0.0058 mmol), with the total amount of oxygen (~ 0.072 mmol) exceeding the amount of oxygen present in ${}^4\text{MnO}_x$ (~ 0.029 mmol). The approximate TON over these six trials is $2448 \text{ mmol O}_2 \text{ mol Mn}^{-1}$. Inductively-coupled plasma with optical emission spectrometry (ICP-OES) conducted on the supernatant solution after the first and last reactions show negligible Mn leeching (<0.01 ppm and <0.02 ppm, respectively). The deviation between the O_2 yield predicted by the initial rate of the Clark data and the yield measured by GC can be attributed to degradation/consumption of the sacrificial reagents during the hour long reactions.

We also studied the precursor role of the $\text{Mn}_4\text{-MOF}$ as compared to Mn^{2+} salt; under the same conditions used to generate ${}^4\text{MnO}_x$ (see experimental section), the salt also resulted in an active Mn-oxide (${}^5\text{MnO}_x$). In contrast to ${}^4\text{MnO}_x$, the PXRD pattern shows only a single broad peak at $2\theta = 37^\circ$ (Figure 2.3a, blue trace) and lacks the low angle peaks associated with ordered stacking in birnessites. Additionally, ${}^5\text{MnO}_x$ results in a lower level of catalytic activity when evaluated in the photoassay; an approximate initial O_2 evolution rate of $\sim 0.15 \text{ mmol O}_2 \text{ mol Mn}^{-1} \text{ sec}^{-1}$ (Figure 2.3b, blue trace) was calculated assuming MnO_2 stoichiometry (see 2.2.4). The BET surface area for ${}^5\text{MnO}_x$ was measured to be $80 \text{ m}^2/\text{g}$. When comparing catalytic performance relative to surface area, ${}^4\text{MnO}_x$ still results in a higher level of activity ($0.038 \text{ } \mu\text{mol O}_2/\text{m}^2$ vs. $0.021 \text{ } \mu\text{mol O}_2/\text{m}^2$). Hence, the crystalline MOF serves as a valuable precursor for the synthesis

of high-surface area, partially ordered Mn oxides with high catalytic activity for photocatalytic OER.

2.3.1 Models for Performance of $^4\text{MnO}_x$

We compared oxygen evolution to a well characterized model hexagonal-type K^+ birnessite (HexBir). There is significant difficulty in structurally characterizing birnessites unambiguously due to vast structural diversity, small particle sizes, and semicrystallinity.⁸⁸ The HexBir used for this study is a rare case of an extremely well-studied and characterized polymorph *via* synchrotron microdiffraction and XANES analysis.¹¹⁰ Lanson et al. report the structural formula of this material to be $\text{K}^{+}_{0.231}\text{Mn}^{3+}_{0.077}(\text{Mn}^{4+}_{0.885} \square_{0.115})\text{O}_2 \cdot 0.60 \text{H}_2\text{O}$, where \square represents lattice vacancies. This phase was obtained using the reported synthesis method and confirmed by PXRD (Figure 2.3a, purple trace); the BET surface area was measured to be $5 \text{ m}^2/\text{g}$.^{109, 119} When evaluated as an OER catalyst in the nitrogen purged photoassay using the same mass loading as $^4\text{MnO}_x$ and $^5\text{MnO}_x$ (125 ppm), very little oxygen was produced (Figure 2.3b, purple trace). However, the O_2 level above the catalyst-free run prompted us to increase catalyst loading to probe if the low activity was due to HexBir's very low surface area, which could limit the availability of reactive sites. When using 1100 ppm of catalyst, O_2 evolution was observed after short lag time (Figure 2.5c), with an initial rate corresponding to $\sim 0.08 \text{ mmol O}_2 \text{ mol Mn}^{-1} \text{ sec}^{-1}$. While this rate is much lower than either $^4\text{MnO}_x$ or $^5\text{MnO}_x$ on a per Mn basis, normalizing to surface area results in a much higher apparent level of activity ($0.15 \text{ } \mu\text{mol O}_2/\text{m}^2$), suggesting the importance of high surface area for layered Mn-oxides in the $[\text{Ru}(\text{bpy})_3]^{2+}/\text{S}_2\text{O}_8^{2-}$ driven systems.

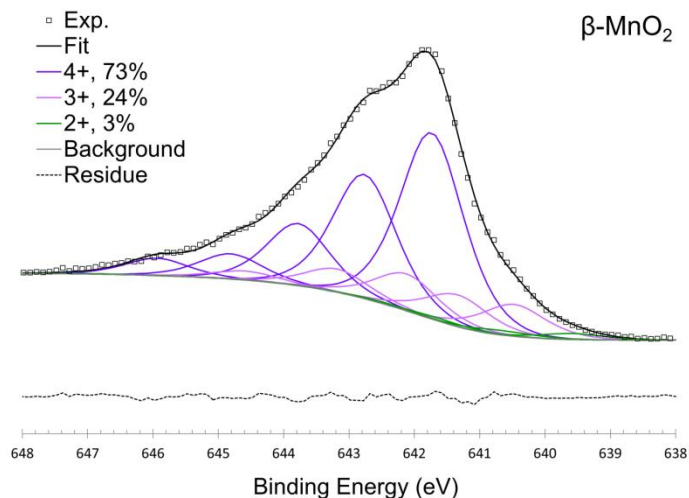
To probe the fate of the bulk structure during the reactions, PXRD measurements were made after 1 hour of reaction time (HexBir AR, Figure 2.3a). Using the two-layer model proposed by Lanson et al., the peak positions of HexBir at $\sim 2\theta = 12.5^\circ$ and 25° correlate to 002 and 004 reflections arising from layer stacking along the crystallographic c-axis, representing

distances of ~ 7.12 and 3.56 Å, respectively (Figure 2.3a, purple trace).¹¹⁰ For HexBir AR, both of these peaks shift to lower angles relative to the higher angle peaks (2-D in plane layer reflections), suggesting that the layer-to-layer spacing increases. Additionally, the peak intensities relative to the higher angle peaks are reduced, suggesting diminished stacking order and may correspond to the exchange of K^+ for Na^+ and H^+ as charge balancing species, as indicated by XPS measurements (Table 2.2). We note the interlayer spacing (~ 5 Å) is not large enough allow entry of $[Ru(bpy)_3]^{2+}$ oxidant molecules (~ 10.2 Å), thereby limiting any activation to the surface and leaving the bulk phase unaffected.

2.3.2 XPS Surface Investigation

XPS spectra of the catalysts were measured after the OER and the Mn $2p_{3/2}$ core levels were analyzed using a strict set of protocols to estimate the oxidation state of Mn at the active surface regions. Following the precedent set by Nesbitt and Banerjee, and based on the multiplet structure calculation by Gupta and Sen, the Mn $2p_{3/2}$ core levels were deconvoluted into five multiplets for each oxidation state of Mn according to the method described in the experimental section.¹¹²⁻¹¹³ A set of exact parameters used can be found in Table 2.1. It needs to be noted that the values obtained using this method are best described as close estimates, however using the same strict parameters for each sample allows for relative comparisons and observation of trends. Rarely are Mn $2p_{3/2}$ spectra for birnessite catalysts analyzed in detail, and none that we are aware of have attempted to deconvolute the region into their multiplet and satellite peaks.

The overall fit for Mn^{4+} is characterized by a peak maximum near 641.9 eV with a shoulder peak on the high energy side at about 642.5 eV, and is readily apparent from the deconvoluted β - MnO_2 reference spectra (Figure 2.6). This general shape dominated all spectra except 5MnO_x , which also has a pronounced shoulder on the low energy side (641 - 642 eV). The main contribution to the Mn $2p_{3/2}$ spectrum of 4MnO_x (Figure 2.7a) is Mn^{4+} , while Mn^{3+} and Mn^{2+} are in lower quantities, resulting in an average surface oxidation state of ~ 3.5 . As Mn^{2+} has

Figure 2.6. $\beta\text{-MnO}_2$ Mn $2p_{3/2}$ spectraTable 2.1. Multiplet Fitting Parameters for Mn $2p_{3/2}$ Spectra

	Gupta-Sen Free Ion Calculation ¹¹³	Nesbitt- Banerjee Birnessite Thin Film ¹¹³	$\beta\text{-MnO}_2$	$^4\text{MnO}_x$	$^5\text{MnO}_x$	HexBir	HexBir AR	Peak Intensity
FWHM (eV):	1*	0.87	1.16	1.16	1.23	1.16	1.16	(% of lowest energy multiplet per oxidation state)
Multiplet Binding Energies (eV)								
Mn^{4+}	641.90	641.90	641.74	641.78	642.40	642.35	642.00	100
Mn^{4+}	642.90	642.92	642.76	642.80	643.38	643.28	643.03	66.7
Mn^{4+}	643.80	643.75	643.78	643.69	644.45	644.15	643.97	33.3
Mn^{4+}	644.80	644.78	644.81	644.60	645.48	645.11	645.08	13.5
Mn^{4+}	646.80	645.80	645.94	645.56	646.41	646.17	646.10	satellite
Mn^{3+}	640.70	640.65	640.48	640.52	641.14	641.09	640.74	100
Mn^{3+}	641.40	641.35	641.35	641.41	641.64	641.72	641.49	100
Mn^{3+}	642.30	642.16	642.12	642.19	642.64	642.40	642.39	135
Mn^{3+}	643.10	643.18	643.18	643.21	643.83	643.62	643.47	70
Mn^{3+}	644.90	644.55	644.58	644.44	645.09	644.92	644.67	30
Mn^{2+}	640.00	639.75	639.58	639.62	640.24	640.19	639.87	100
Mn^{2+}	641.30	640.95	640.66	640.91	641.24	641.34	640.90	75
Mn^{2+}	642.40	641.75	641.61	641.72	642.04	642.03	641.90	50
Mn^{2+}	643.10	642.65	642.43	642.33	643.34	643.29	642.75	25
Mn^{2+}	647.60	644.15	647.13	646.92	647.56	647.77	647.29	15

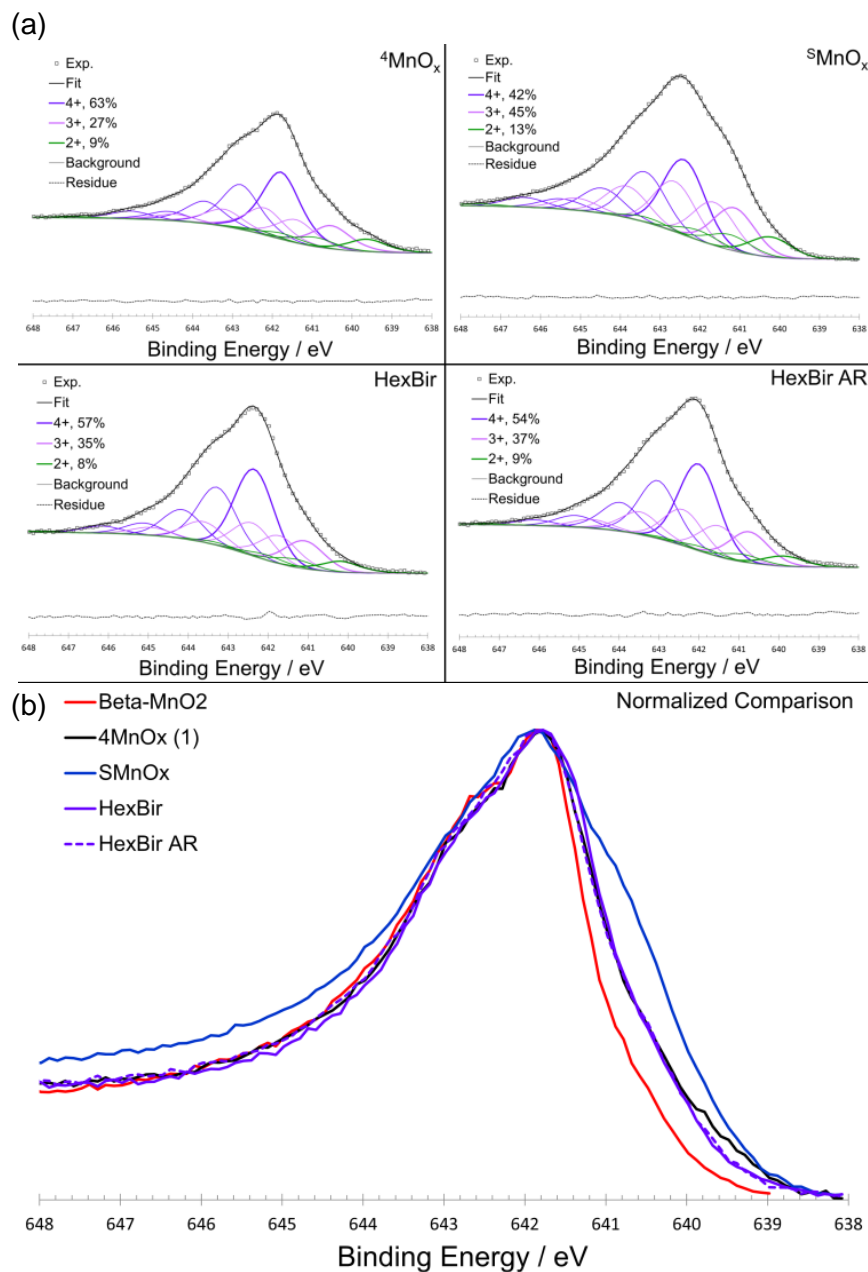


Figure 2.7. Mn $2p_{3/2}$ XPS spectra. (a) Deconvoluted spectra for $^4\text{MnO}_x$ (top left), $^5\text{MnO}_x$ (top right), HexBir (bottom left), and HexBir AR (bottom right). Traces: experimental data (boxes), overall fit (black), Mn^{4+} (purple), Mn^{3+} (pink), Mn^{2+} (green), residual (grey dash below spectra). (b) Intensity and binding energy normalized Mn $2p_{3/2}$ spectral data overlay (experimental). $\beta\text{-MnO}_2$ (reference sample, red), $^4\text{MnO}_x$ (black), $^5\text{MnO}_x$ (blue), HexBir (purple), and HexBir AR (purple dashed).

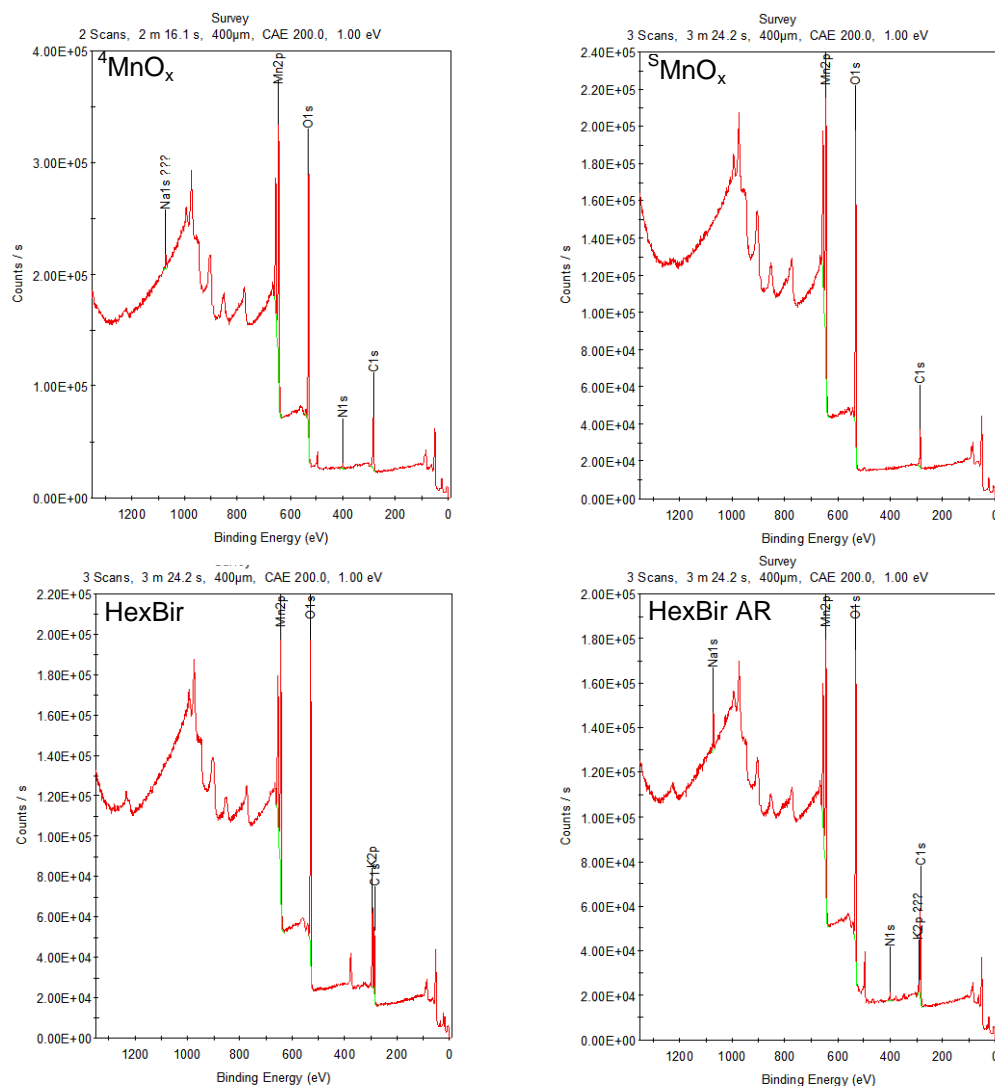


Figure 2.8. XPS survey scans.

Table 2.2. XPS Survey Scan Atomic Percentages

XPS survey scan atomic percentages					
	β -MnO ₂ (not shown)	⁴ MnO _x	^S MnO _x	HexBir	HexBir AR
Mn2p	21.32	21.14	26.39	20.47	16.35
O1s	56.31	46.80	53.07	49.75	43.65
K2p	-	-	-	9.58	0.87
C1s	14.87	27.96	-	20.2	32.47
Na1s	2.17	1.82	20.54	-	3.99
N1s	-	2.29	-	-	2.67
S2p	5.33	-	-	-	-

$\sim 45\%$ larger atomic radii than Mn^{4+} , it is unlikely that it resides within the octahedral sheets, but rather exists as a charge balancing species on the surface or in the interlayer. Mn^{3+} has been found to exist within the layer as well as occupying vacant Mn^{4+} sites, which may contribute to layer disorder and possibly promotes layer flexibility (atomic radii: $\text{Mn}^{2+} = 0.972 \text{ \AA}$, $\text{Mn}^{3+} = 0.785 \text{ \AA}$, $\text{Mn}^{4+} = 0.670 \text{ \AA}$).¹¹³ The presence of Na^+ ($\sim 2\%$) was also detected by our survey scan, and is likely acting as a charge balancing species. In contrast, the Mn $2p_{3/2}$ spectrum for $^5\text{MnO}_x$ (Figure 2.7a) shows a lower surface oxidation state (~ 3.3) and the main contributor to spectrum is Mn^{3+} , which can be viewed as an increase in the low energy shoulder at $\sim 641.5 \text{ eV}$. The lack of any ordered stacking apparent from the low angle region of the PXRD pattern for this sample suggests a mainly amorphous oxide material, which may be comprised of 2-D sheets. The lack of any Na^+ signal from our survey scan may suggest the importance of an interlayer region for the presence of charge balancing group 1 cations.^{99, 120-121}

Mn $2p_{3/2}$ Spectra for HexBir and HexBir AR show minimal change between the two samples (Figure 2.7a). In both cases, features from Mn^{4+} dominate the spectra and show an estimated surface oxidation state of ~ 3.5 . There appears to be a very slight increase in Mn^{3+} relative to Mn^{4+} in the HexBir AR sample, which can be observed as a slight decrease in the shape of the high energy shoulder at $\sim 643 \text{ eV}$ and an increase in the low energy shoulder between $\sim 641 \text{ eV}$. The observed increase in surface Mn^{3+} , although subtle, may suggest a pathway for activation *via* photoreduction and subsequent ejection of an $\text{Mn}_{\text{layer}}^{4+}$ atom to an Mn^{3+} occupying the newly formed vacancy as very recently described by Peña et al.¹²², or surface disproportionation/comproportionation equilibria. Survey scans of both samples suggest an exchange of K^+ during the reaction for Na^+ and H^+ to maintain charge neutrality (Table 2.2). This is not surprising considering reaction conditions (0.1 M NaHCO_3) and the tendency of these materials to undergo cation exchange.⁸⁸

To compare the spectra directly, the Mn 2p_{3/2} regions were normalized and overlaid (Figure 2.7b). From this figure, the surface Mn oxidation state similarity between ⁴MnO_x and HexBir is apparent. The main difference lies in the shapes of the spectra; ⁴MnO_x has a better defined high energy shoulder (~ 642.5 - 643 eV) and a slightly narrower profile, however the differences are minimal and better expressed with deconvolution of the original spectra. We were surprised to find that any surface Mn²⁺ persists through the oxidizing conditions and might question the validity of this assumption if not for the comparison to the β-MnO₂ reference, which shows minimal Mn²⁺ contribution (~ 3%). We note that catalytic activity does not appear to scale with total surface Mn³⁺ content, as suggested by the performance of ⁵MnO_x.

Table 2.3. Estimated relative abundances of Mn oxidation states on catalyst surfaces from XPS measurements.

Sample	Mn ⁴⁺ (%)	Mn ³⁺ (%)	Mn ²⁺ (%)	FWHM (eV)
β-MnO ₂	73	24	3	1.16
⁴ MnO _x	63	27	9	1.20
⁵ MnO _x	42	45	13	1.25
HexBir	57	35	8	1.19
HexBir AR	54	37	9	1.25

2.3.3 ⁴MnO_x Structural Characterization

Bulk structural analysis of the most active catalyst, ⁴MnO_x, was performed to better understand the nature of the material. High energy PXRD with PDF analysis has emerged as a powerful total scattering technique for collecting detailed local and long range structural information for poorly crystalline or nanoscale materials.¹²³⁻¹²⁷ The PDF, $G(r)$, reports all atom-atom distances in a sample as a weighted histogram, with peaks observed at r -values

corresponding to well-defined bond lengths and atom distances within the material. This method, as noted in previous work, provides similar information as EXAFS except covers the full range of atom-atom distances and is free of Debye-Waller effects (peak broadening at longer distances), resulting in more reliable distances past the first coordination shell and higher resolution. PDF has proven valuable in elucidating minor structural features in cobalt oxide WOCs.¹²⁸

Although broad, the most intense peaks in the high-energy diffraction data for $^4\text{MnO}_x$ correspond to the principal diffraction features for birnessite-type MnO_2 (Figure 2.9). The corresponding PDF data (Figure 2.10, black line) was fit within PDFgui by a real space structural model corresponding to a refined monoclinic birnessite structure ($R \sim 27\%$; $C2/m$; $a = 4.97 \text{ \AA}$, $b = 2.84 \text{ \AA}$, $c = 7.29 \text{ \AA}$; $\beta = 98.7^\circ$) (Figure 2.10, red line).¹¹⁴ There was no evidence of other semi-crystalline manganese oxide phases, even as a minor component. Atom-atom correlations within individual layers of edge-sharing MnO_6 octahedra were well-defined and dominated the PDF data, however correlations between atoms in different layers or interstitial species were not clear, suggesting a large distribution/disorder in the interlayer structure. Bond lengths were determined by fitting Gaussian functions to peaks in the PDF within Fityk (nonlinear curve fitting and data analysis software).¹²⁹

The average Mn-O bond length for $^4\text{MnO}_x$ was determined to be 1.912 \AA , but a small shoulder peak is observed at $\sim 2.15 \text{ \AA}$, possibly arising from Jahn-Teller elongated axial Mn(III)-O bonds present in Mn(III)O_6 octahedra.⁹¹ The most intense peak at 2.868 \AA corresponds to di- μ -oxido bridging between Mn atoms and is common for birnessites. The other bond lengths illustrated in Figure 2.10 occurring at 3.455 , 4.461 , 4.943 , 5.682 , and 6.046 \AA are commensurate with common intralayer distances. Notably, $^4\text{MnO}_x$ shows the most significant intensity misfit at $\sim 3.5 \text{ \AA}$, which can be assigned to triple corner sharing $\text{Mn}_{\text{interlayer}}^{3+}$ (Figure 2.11) located above or below layer vacancies. The model used to fit the data was refined from a monoclinic-type birnessite structure, characterized by rows of $\text{Mn}_{\text{layer}}^{3+}$, minimal lattice vacancies, and thus a

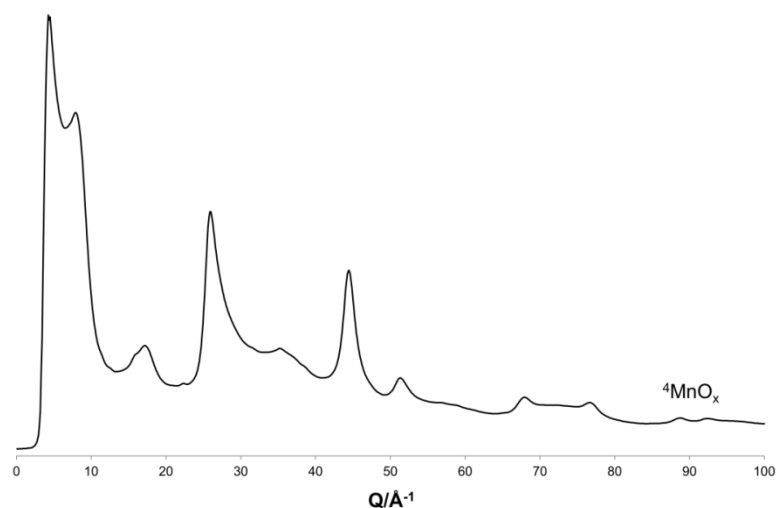


Figure 2.9. Synchrotron PXRD pattern for ${}^4\text{MnO}_x$.

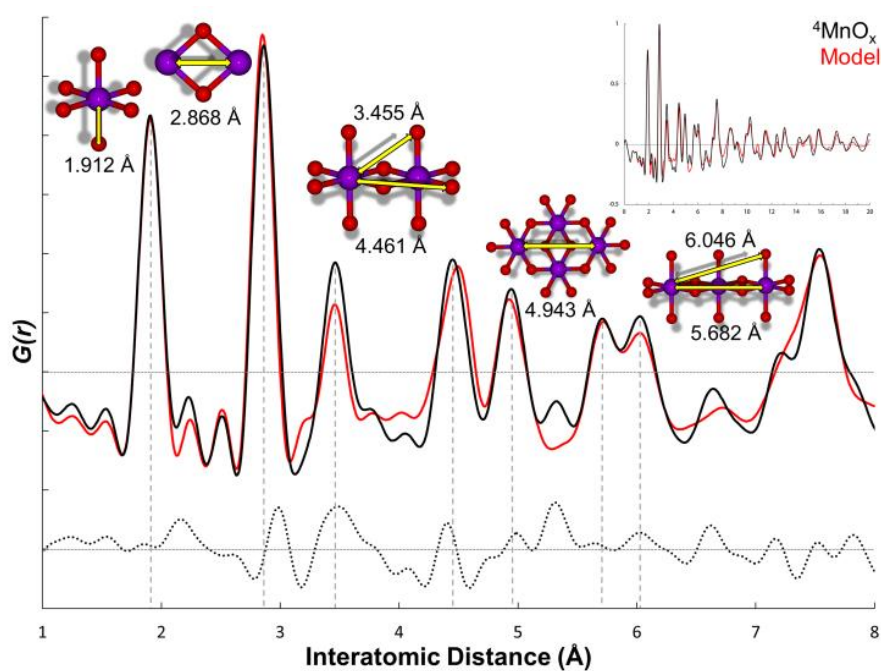


Figure 2.10. Comparison of the experimental $G(r)$ obtained for ${}^4\text{MnO}_x$ (black) with the calculated $G(r)$ for the refined birnessite structure model (red). Illustrations correlate distances obtained by the PDF study with distances found within a single birnessite layer. Inset shows PDF data expanded to 20 Å and the dashed line shows the residual pattern.

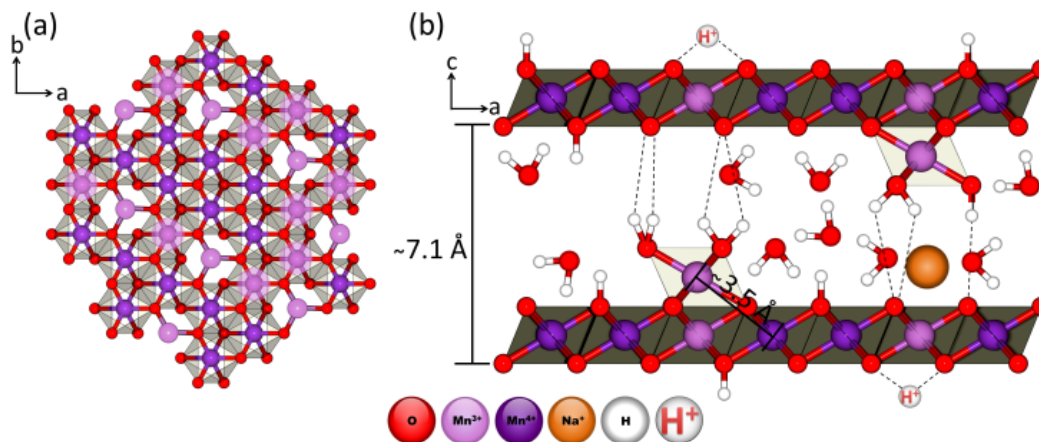


Figure 2.11. Idealized conceptual drawing of 4MnOx along the crystallographic c-axis (a) and b-axis (b). Interlayer/surface Mn³⁺ species over vacant sites are represented as the triply bonded species Mn atoms in (a) and as the Mn octahedra out of the layer plane in (b).

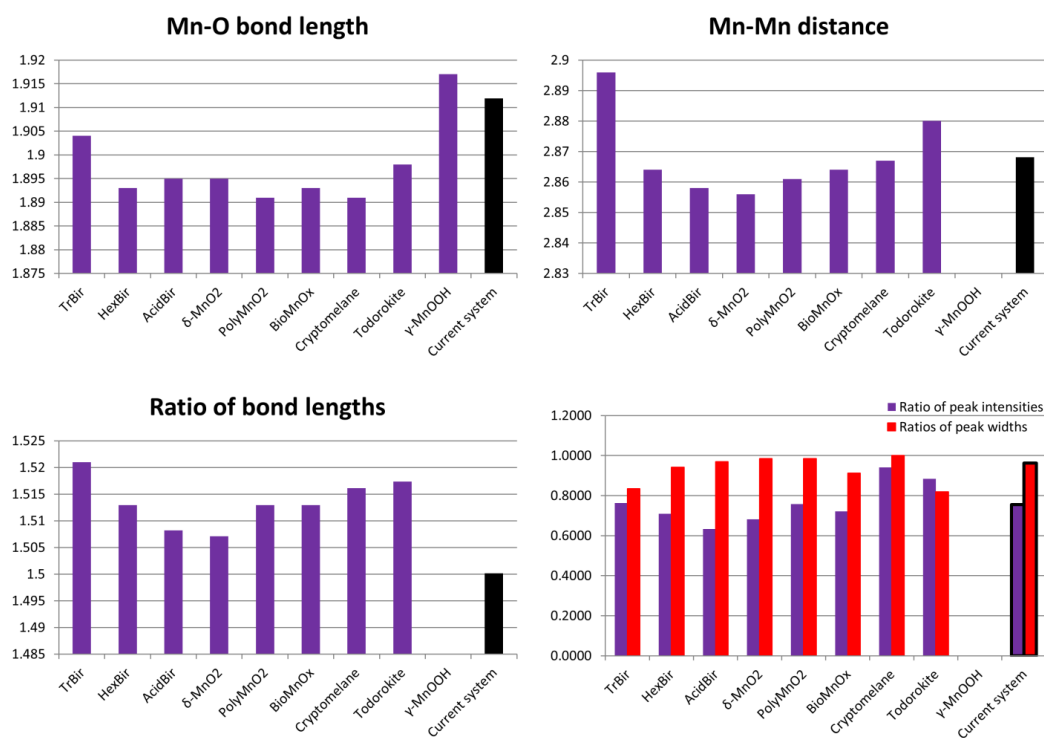


Figure 2.12. Comparison of PDF bond parameters resulting from current study to those of Zhu et al.¹³⁰ (a) Mn-O bond length; (b) Mn-Mn distance (u₃-O bridged); (c) ratio of Mn-Mn:Mn-O distance; (d) ratios of Mn-O:Mn-Mn peak intensities and peak widths.

minimal $\text{Mn}_{\text{interlayer}}^{3+}$ contribution, which helps to explain the misfit at this distance. The caption image in Figure 2.10 shows the shows atomic distances expanded to 20 Å, and matches well with the refined model. Both the average Mn-O bond length and the Mn-Mn distance are similar to those reported by Lanson et al. for the HexBir sample used in this study (1.914 and 2.84 Å, respectively).¹¹⁰ They also show that the average $\text{Mn}_{\text{interlayer}}^{3+}$ - $\text{Mn}_{\text{layer}}^{4+}$ interatomic distance is ~ 3.540 Å, which correlates with the increased peak intensity in our PDF data at this value.

Our results can be compared to those of Dau, Kurz and coworkers, who studied the bond lengths of a number of synthetic birnessite catalysts using EXAFS.^{67, 69} Compared to their work, the current system shows a slightly longer average Mn-O bond length (1.912 vs 1.89 Å) and a similar Mn-Mn distance (2.868 vs 2.88 Å). They attribute bonding features occurring at about 3.3 Å to the presence of cubane-like motifs arising from triple-corning sharing interlayer cations, such as Sr^{2+} and Ca^{2+} , which act as charge balancing species for $\text{Mn}_{\text{layer}}^{3+}$. This particular feature was discussed in terms of possible catalytic reaction sites, owing to structural similarity to the naturally occurring OEC.⁶⁹ In contrast, $^4\text{MnO}_x$ has a very minor charge balancing contribution from Na^+ (~ 0.07 per MnO_2), and instead $\text{Mn}_{\text{interlayer}}^{3+}$ acts to balance $\text{Mn}_{\text{layer}}^{4+}$ vacancies. As also suggested by Suib and coworkers, we speculate that this feature may be contributing to the observed catalytic activity through coordinatively unsaturated oxygen atoms which can assist in proton coupled electron transfer (PCET) through intermediate $\mu\text{-OH}$ units.⁶⁸ Additionally, HexBir structural studies by Lanson et al. show that $\text{Mn}_{\text{interlayer}}^{3+}$ coordinate as many as 0.24 of the 0.60 structural water molecules, suggesting that these sites may have an additional role to play in binding water molecules during catalysis (see Figure 2.11).

We compared the PDF data with those of Sparks and coworkers, who performed similar analysis on a variety of birnessites (Figure 2.12).¹³⁰ $^4\text{MnO}_x$ shows a similar ratio of Mn-O to Mn-Mn peak intensities and widths (reflects vacancy concentration) to ‘hexagonal birnessite’ (also

notated as HexBir in Figure 2.12, not to be confused with the HexBir used in our study), indicating a high fraction of lattice vacancies. In contrast, $^4\text{MnO}_x$ has a longer Mn-O bond length than any of their studied birnessites. For example, their hexagonal birnessite was reported to have an average Mn-O bond length of only 1.893 Å, which is significantly shorter than $^4\text{MnO}_x$ and the reported distance for HexBir by Lanson et al.¹¹⁰ Instead, our average Mn-O bond distance is more akin to their triclinic (TrBir, 1.904 Å) or manganite (γ -MnOOH, 1.917 Å) distances. This is possibly due to differences in sample preparation methods, as birnessites are known for their vast structural diversity arising from even minor differences in synthetic conditions.

Additional structural studies were carried out using Raman spectroscopy. Raman has been noted as an excellent technique to study the structure of amorphous materials due to its sensitivity to short range order.¹³¹⁻¹³² Spectra were collected for the parent MOF structure, $^4\text{MnO}_x$, and a birnessite formed under alkaline conditions whose Mn^{3+} content is mostly limited to the layer and that we have characterized previously (δ -MnO₂, Figure 2.13).^{71, 133} Both $^4\text{MnO}_x$ and δ -MnO₂ show features common to birnessite-type MnO₂.¹³¹ The three main features are the weaker peak at ~ 475 -510 cm^{-1} and two stronger peaks at ~ 550 -570 and 620-650 cm^{-1} . The band at 650 cm^{-1} is the most notable; it is assigned to the symmetric stretching mode $\nu_2(\text{Mn-O})$ perpendicular to the chains of MnO₆ octahedra. The peak at ~ 575 cm^{-1} is assigned to the $\nu_3(\text{Mn-O})$ stretching in the basal plane and is similar for both $^4\text{MnO}_x$ and δ -MnO₂. Compared to the spectrum of δ -MnO₂, the $\nu_2(\text{Mn-O})$ mode in $^4\text{MnO}_x$ shifts to a higher wave number and intensity relative to the peak at 575 cm^{-1} , which can be viewed as reflecting lattice vacancy concentration and layer-layer interactions. Chen et al. showed that as Na-birnessite interlayer sodium atoms were replaced by water, the ν_2 mode shifted to a higher wavenumber and became more intense relative to the ν_3 mode, which is consistent with our results.¹³² These results are also consistent with those of Pereira-Ramos et al., who demonstrate similar findings when comparing Li-Bir (similar to δ -MnO₂, ordered interlayer) to SG-Bir (HexBir-like).¹³¹ We assign the weak double peak at the

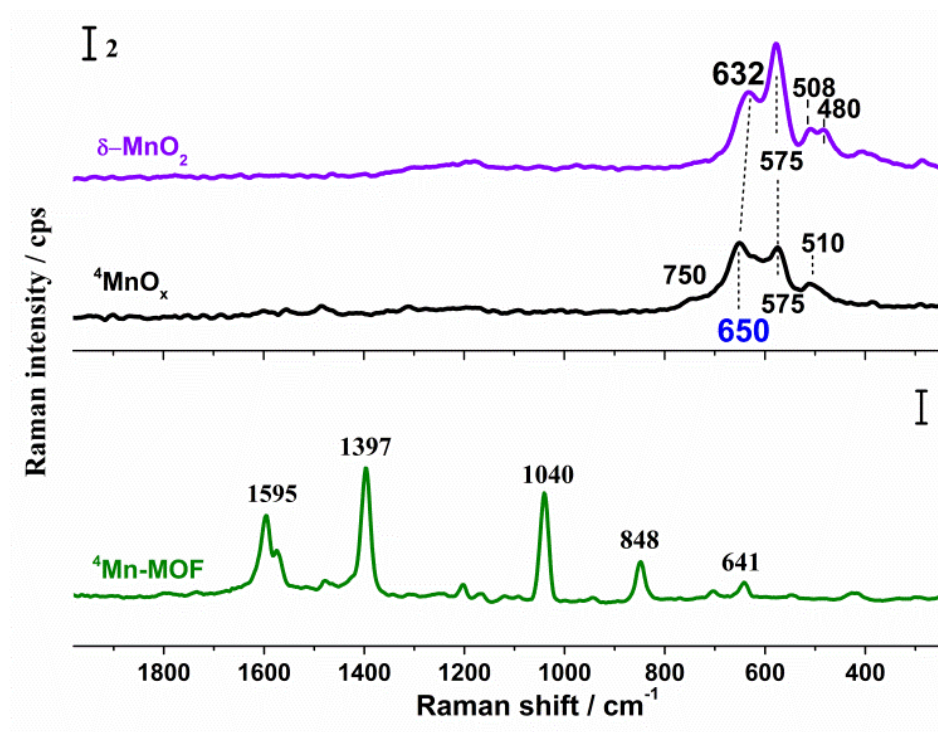


Figure 2.13. Raman spectra of Mn₄-MOF (green), 4 MnO_x (black), and δ -MnO₂ (purple).

lower wave numbers (480, 508 cm⁻¹) to interlayer ordering and guest identity/binding modes; as interlayer species changes, the distinctive features of this region change in response. Pereira-Ramos et al. show very distinctive separated sharp peaks when Li⁺ is the guest, as opposed to our double peak in the case of Mn³⁺ or Na⁺, the double peak is lost and instead a largely featureless single peak is obtained.

Finally, the morphology and lattice disorder of 4 MnO_x was studied using HR-TEM. The zoom-out images in Figure 2.2b depict pebble/flake-like morphology ranging from ~ 30 - 100 nm in size. Each flake is comprised of multiple layers/sheets (Figure 2.14a). The lattice images (Figures 2.14b and 2.14c) depict a highly disordered and flexible layer structure; a SAED (selected area electron diffraction) pattern was unobtainable due to the level of disorder. The inset image in Figure 2.14b shows MnO₆ octahdra lattice fringes, which were measured to be ~ 2.8 Å and is commensurate with our PDF data. There appears to be regular disruption of the fringes,

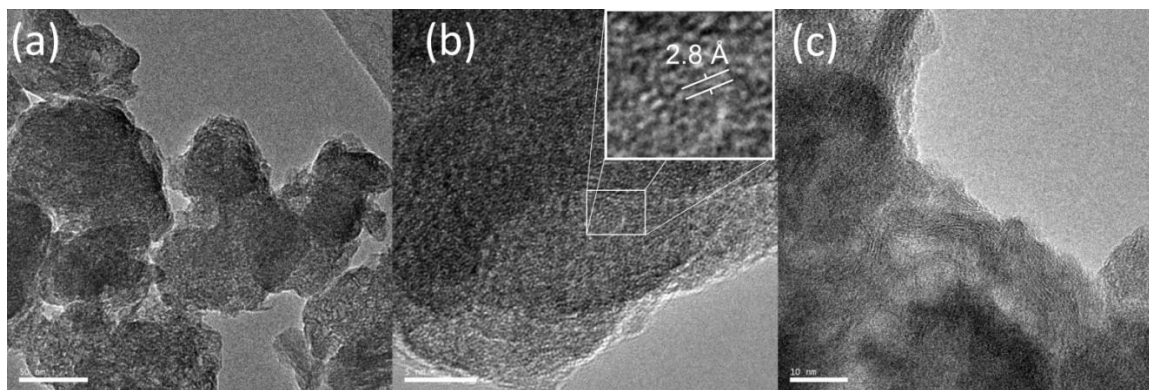


Figure 2.14. HR-TEM images of ${}^4\text{MnO}_x$. (a) 50 nm scale showing layered flake-like morphology; (b) 5 nm scale showing disordered basal plane, the inset is a magnification of the indicated region showing ~ 2.8 Å lattice fringes; (c) 10 nm scale showing lattice fringe curvature.

resulting in the disordered appearance of the layer and is a likely cause for the deviation from the typical crisscross pattern expected for crystalline birnessite.¹¹⁴ These features may be a combined result of random locations of both $\text{Mn}_{\text{layer}}^{3+}$ atoms and $\text{Mn}_{\text{layer}}^{4+}$ vacancies. Lattice fringe curvature is observed in Figure 2.14c, as there appears to be entire semi-ordered regions that curve/flex throughout the edge region of the flake. We speculate that these may correspond to flexible regions dominated by $\text{Mn}_{\text{layer}}^{3+}$, where the columns form to minimize lattice strain caused by Jahn-Teller distortion.

2.3.4 ${}^4\text{MnO}_x$ Formation

Oxidation of Mn^{2+} in solution has been previously studied by Hem and Lind, whereby various manganese oxides were precipitated *via* bubbling air through dilute (0.01 M) solutions of MnX_y ($X = \text{Cl}^-$, NO_3^- , SO_4^{2-} , or ClO_4^-).¹³⁴ They found that depending upon the pH, temperature, and counter-ion, that metastable forms of Mn^{3+} species could be expected. In turn, Mn^{3+} disproportionates into MnO_2 and Mn^{2+} , but pH and ligand environment can control the extent of this disproportionation. For instance, oxidation of Mn^{2+} is known to proceed fully to MnO_2 at alkaline pH and in the presence of weak field ligands (e.g., NO_3^- , Cl^-). On the other

hand, strong field ligands have been observed to stabilize Mn^{3+} in other systems, and both pyrophosphate and sulfate anions have been observed to favor the formation of MnOOH .¹³⁵⁻¹³⁷ We suspect this complex equilibrium accounts for the variety of Mn oxidation states observed by XPS, and the high degree of disorder found across both of the *in-situ* generated materials.

2.4 Conclusion

Catalytically active MnO_x species were found to form under commonly used photocatalytic water oxidation conditions for the first time. Using an Mn_4 -MOF precursor results in the most active material studied in this work, $^4\text{MnO}_x$. Detailed structural analysis suggests that $^4\text{MnO}_x$ is similar to hexagonal birnessite-type MnO_2 , and can be characterized by the presence of $\text{Mn}_{\text{layer}}^{3+}$, $\text{Mn}_{\text{interlayer}}^{3+}$ species, as well as and $\text{Mn}_{\text{layer}}^{4+}$ vacancies, giving rise to layer disorder and possible flexibility. There are multiple reports of OER activity on MnO_x materials prepared using a variety of methods and comparing the activity of these various materials to one another is difficult due to variations in reaction conditions and methods. With that said, $^4\text{MnO}_x$ is on the high end of the performance range typically reported for MnO_x catalysts evaluated in the $[\text{Ru}(\text{bpy})_3]^{2+}/\text{S}_2\text{O}_8^{2-}$ /visible light driven systems,⁹⁴ which may be partially attributed to its very high surface area ($216 \text{ m}^2/\text{g}$). In contrast, the $^5\text{MnO}_x$ catalyst formed from Mn^{2+} salt shows a lower average surface oxidation state, lower surface area ($80 \text{ m}^2/\text{g}$), apparent lack of ordered stacking, and a lower level of activity, even when surface area normalized. Both materials show significantly higher levels of activity than crystalline hexagonal K^+ birnessite when employed in the same photoassay.

The surface Mn oxidation states of the MnO_x catalysts were studied using XPS and compared to those of hexagonal-type birnessite before and after reaction. All species showed enriched Mn^{3+} and Mn^{2+} content near the surface that be possibly attributed to surface comproportionation/ disproportionation equilibria of MnOOH species. PDF analysis results in

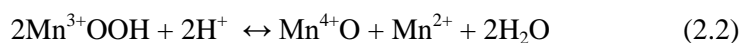
highly resolved ${}^4\text{MnO}_x$ bond distances and indicates the presence of $\text{Mn}_{\text{interlayer}}^{3+}$ occupying layer vacancies, highlighting this technique as an alternative to EXAFS for studying semi-crystalline materials. The description of ${}^4\text{MnO}_x$ as hexagonal-birnessite like was further confirmed through the use of Raman spectroscopy, and disordered flexible layers were illustrated *via* HR-TEM. This work supports our previous finding that proposes catalysis is promoted by structural flexibility and Mn^{3+} content. Finally our study suggests that many Mn^{2+} species have potential form similar active MnO_x materials under photocatalytic water splitting conditions, and that rigorous post catalytic analysis is necessary to confirm the active species.

2.5 Collaborative Follow-Up Study on Manganite as a Water-Oxidation Catalyst¹³⁸

[ACS Catal., 2016, 6 (3), pp 2089–2099]

The following is a brief summary of collaborative work resulting in publication in ACS Catalysis, first authored by Paul Smith of the Dismukes research group at Rutgers University; the dissertation author was second author on the publication. The dissertation author's contribution was the original concept, PXRD measurements, XPS deconvolution, and structural illustrations. The following is a brief summary of the motivation for the work and a summary of results. Besides electrochemical data, all included illustrations are the original work of the dissertation author.

Based on the structural evaluation of ${}^4\text{MnO}_x$, our findings support the idea that the origin of activity in layered Mn-oxides is triple corner sharing $\text{Mn}_{\text{interlayer}}^{3+}$ atoms residing in layer superficial positions located over $\text{Mn}_{\text{layer}}^{4+}$ lattice vacancies, originally proposed by Dau and coworkers. Additionally, it is well documented that equilibrium exists between MnO_2 and MnOOH *via* equation 2.2. It may not then be coincidence that the triple-corner sharing tunnel



structure of γ -MnOOH shares similar structural features arising from the $\text{Mn}_{\text{interlayer}}^{3+}$ atoms in layered MnO_2 (Figure 2.14). In fact, when we originally performed XPS measurements on $^4\text{MnO}_x$, the survey scan appeared very similar to that of manganite. We hypothesized that if the triple-corner sharing $\text{Mn}_{\text{interlayer}}^{3+}$ species was largely contributing to the apparent activity of the disordered birnessite materials, then it was quite possible that manganite, which had yet to be reported as a WOC, would also show activity due to having nearly identical coordination

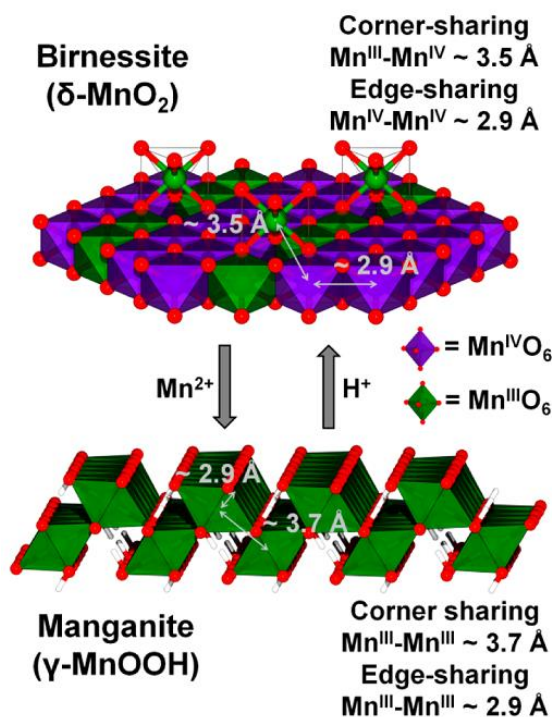


Figure 2.15. Structural illustration of the equilibrium between $\delta\text{-MnO}_2$ and $\gamma\text{-MnOOH}$.

environment.

Both photochemical and electrochemical water oxidation experiments were performed on freshly prepared samples of $\gamma\text{-MnOOH}$. The results demonstrate that manganite does indeed have activity, and in fact has the second lowest overpotential for water oxidation of all reported manganese oxides (bixbyite, Mn_2O_3 is the lowest). The overpotential at 10 mA/cm^2 was 530 mV in 1 M NaOH at pH 14, and 680 mV in phosphate buffer at pH 7. Mn^{3+} was confirmed as the

active phase by comparing electrocatalytic performance to pyrolusite (β - MnO_2), which shares a similar tunnel structure to γ - MnOOH but is composed entirely of Mn^{4+} (Figures 2.16 and 2.17). Under both neutral and basic conditions β - MnO_2 fails to show any significant catalytic response. Additionally, no preoxidation wave was observed in the CVs of fresh samples of manganite, confirming Mn^{3+} as the active oxidation state. However, the material deactivates during bulk electrolysis after 4 e^-/Mn of charge have passed. PXRD measurements of the catalyst after electrolysis show loss of characteristic peaks, indicating severe structural degradation, which was confirmed by HR-TEM. Furthermore, XPS measurements with $\text{Mn}2\text{p}_{3/2}$ peak deconvolution post electrolysis indicate significant formation of Mn^{4+} , which has proven to be largely electrochemically inactive (Figure 2.18). Despite this deactivation, these findings strongly support that $\text{Mn}^{3+}_{\text{interlayer}}$ are the active sites of $\gamma\text{-MnO}_x$.

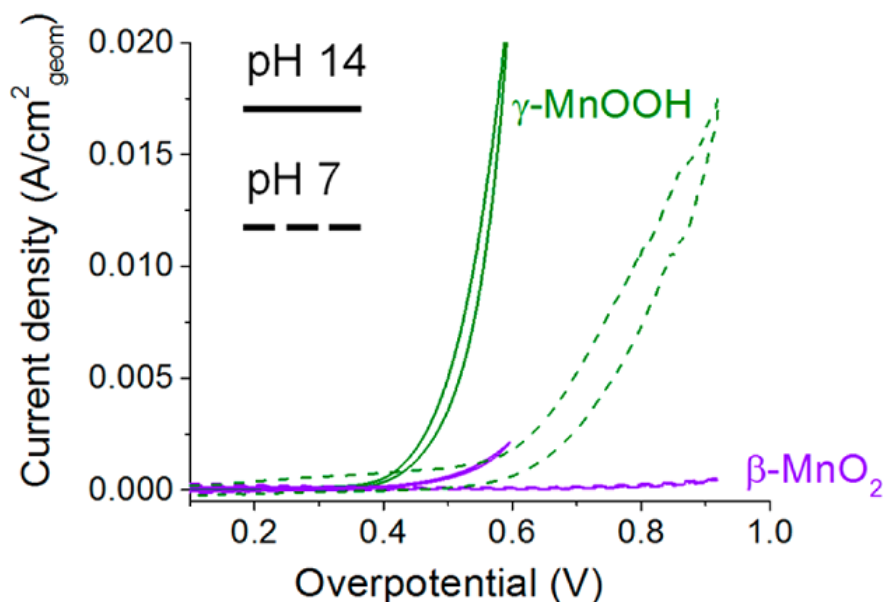


Figure 2.16. “Cyclic voltammograms (10 mV/s, iR corrected) for the 1×1 tunnel manganese oxides of Figure 1 in 1 M NaOH or 1 M phosphate buffer, with loading $0.5 \text{ mg}/\text{cm}^2$. Conditions: 5 mm glassy-carbon working electrode, Ti counter electrode, reference electrodes Hg/HgO (pH 14, $E_{\text{ref}} = +0.100 \text{ V}$ vs NHE) and Ag/AgCl (pH 7). The silver reference electrode was externally

calibrated vs SCE ($E_{\text{ref}} = +0.240 \text{ V vs NHE}$). Overpotentials are corrected for the pH dependence of water oxidation and given relative to each reference electrode using the expression $(\text{measured potential}) - (1.23 \text{ V} - (0.059 \times \text{pH}) - E_{\text{ref}})$. The current is normalized to the geometric electrode area.”¹³⁸

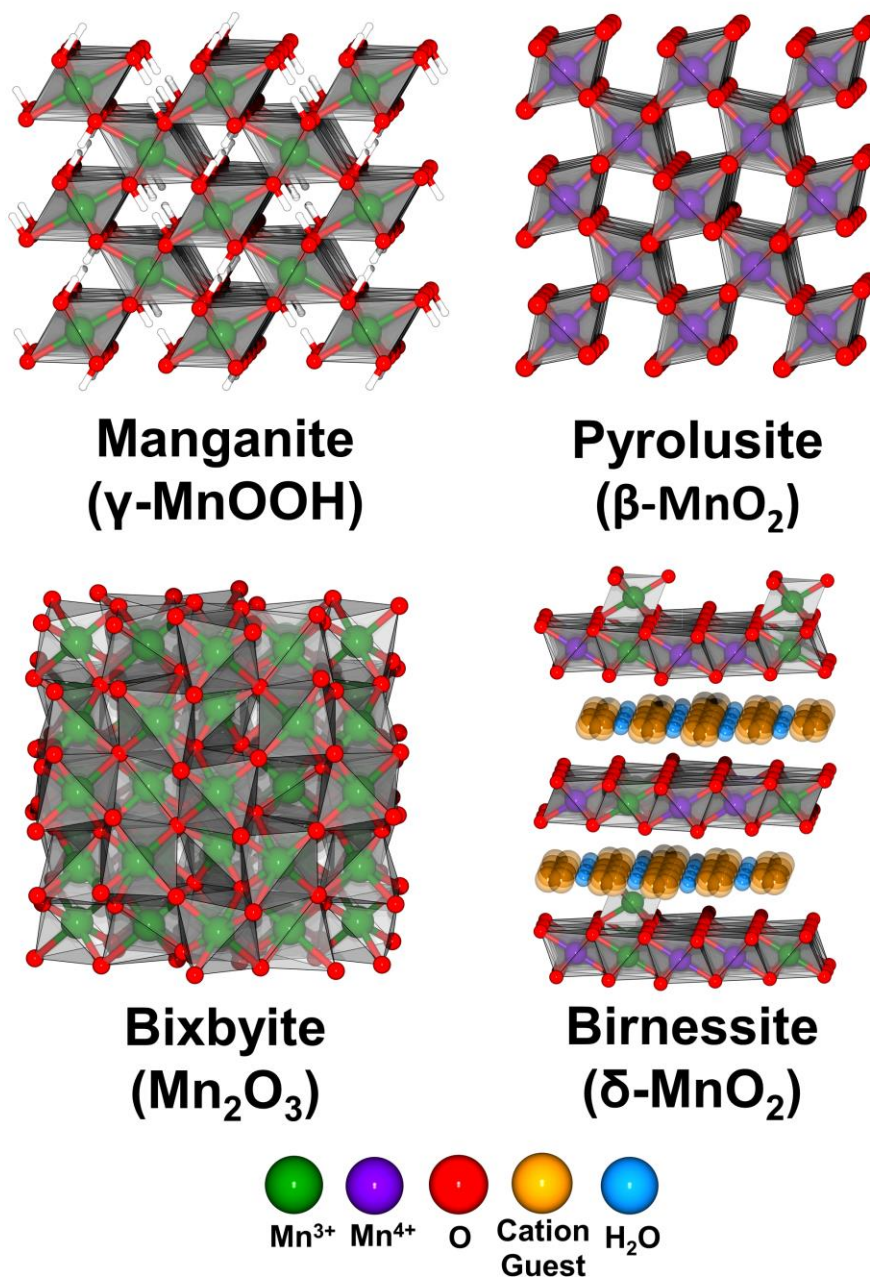


Figure 2.17. Crystal structure illustrations of various tested phases of manganese-oxide.

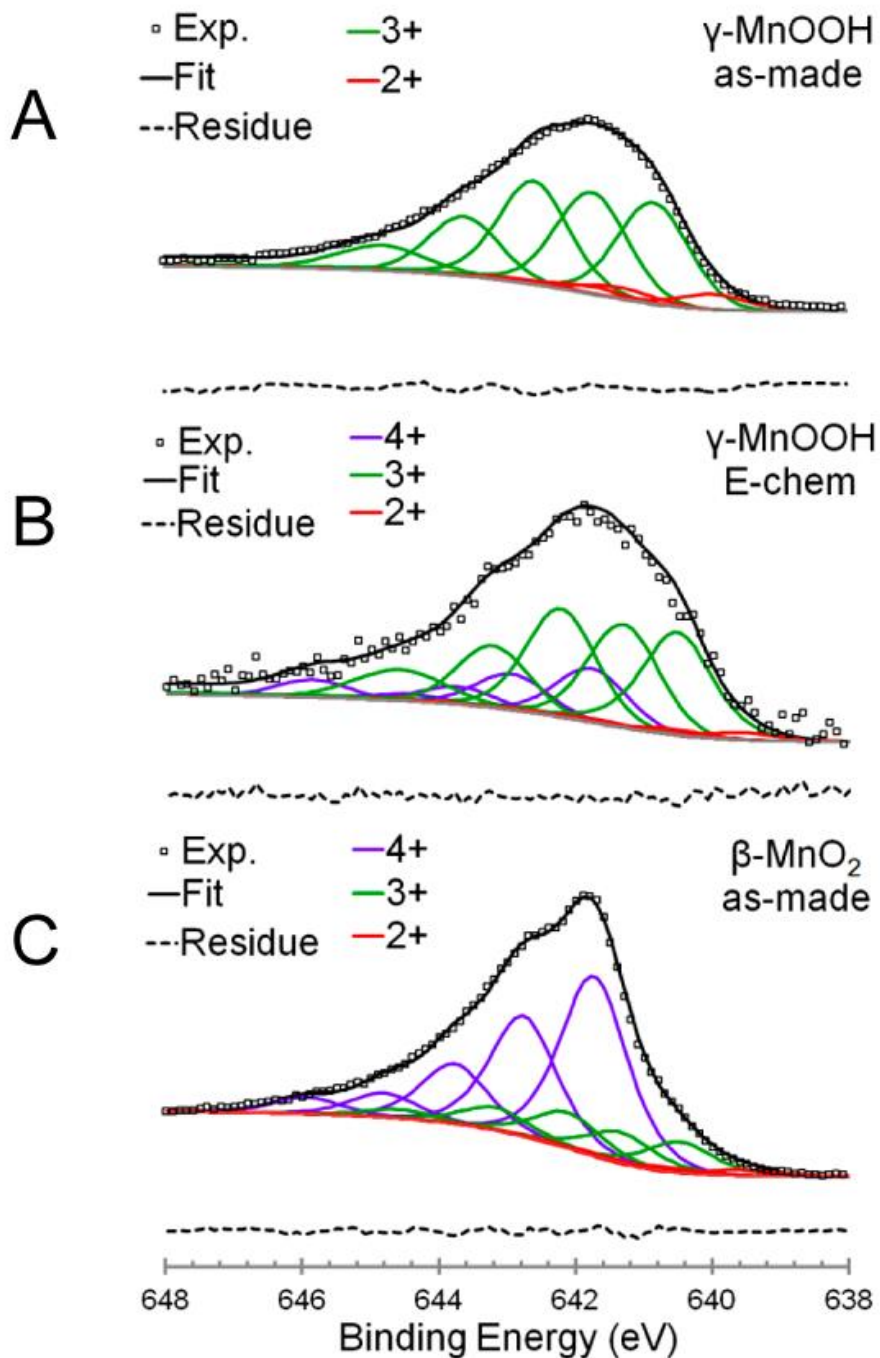


Figure 2.18. “Mn $2p_{3/2}$ region of XPS spectra comparing γ -MnOOH (A), β -MnO₂ (C), and electrochemically oxidized γ -MnOOH (B). These spectra are deconvoluted into contributions from Mn^{4+} (purple), Mn^{3+} (green), and Mn^{2+} (red) via the method of Nesbitt and Banerjee as described previously.”¹³⁸

CHAPTER 3. Distinct Reversible Colorimetric and Fluorescent Low pH Response on a Water-Stable Zirconium-Porphyrin Metal-Organic Framework⁵⁰

[*Chem. Commun.*, **2014**, 50, 9636-9639] – Accepted as Front Cover Article

3.1 Introduction

Metal-organic frameworks (MOFs) have been under intense investigation since their popularization around the turn of the millennium for a wide variety of potential applications.^{102-105, 139-151} The immobilization of organic linker ligands to metal ions or metal clusters not only gives rise to a vast number of fundamentally interesting porous crystalline structures, but also opens up the possibility of converting homogenous systems into heterogeneous analogues capable of emulating or surpassing the original properties of the parent molecule(s).¹⁵²⁻¹⁵³ The rational design of MOF chemical sensors build on this premise; the systematic ordering and immobilization of fluorescent organic ligands into MOF structures often enhances and optimizes the original optical properties of the ligand, as well as providing a stable and porous manifold to function within.^{139, 147-148} As such, it is no surprise that MOFs are being so widely investigated for chemical sensing. An idealized MOF sensor will demonstrate at minimum the following attributes: selective interaction with the analyte, a distinct fluorescent or colorimetric response, a high degree of stability in the analyte media, and a high degree of recyclability.

The fluorescent and colorimetric properties of tetrapyrrolic macrocycles (porphyrin derivatives) is a vast and rich field containing innumerable entries.¹⁵⁴⁻¹⁶³ However, their appearance as linkers in MOF structures is relatively new, and while there are a number of porphyrin MOFs reported, their properties have been investigated to a much lesser extent.¹⁶⁴⁻¹⁷⁰ Recently, Hong-Cai Zhou's group reported a zirconium-porphyrin MOF (PCN-225) capable of fluorescent pH sensing through luminescent emission enhancement in basic solution, demonstrating the feasibility of pH fluorescent sensing with these materials. The material was found to have the most sensitive response in the range of pH 7 - 10.¹⁶⁸

Herein we report an idealized case of MOF chemical sensing through the reversible colorimetric and fluorescent pH response of the reported zirconium-porphyrin MOF, PCN-222, in the range of pH 3 - 0.¹⁶⁷ This MOF contains a $\text{Zr}_6(\mu_3\text{-OH})_8(\text{OH})_8(\text{CO}_2)_8$ secondary building unit (SBU), where $(\text{CO}_2)_8$ correspond to the carboxylate groups from eight meso-tetra(4-carboxyphenyl)porphyrin (H_2tcpp) ligands.

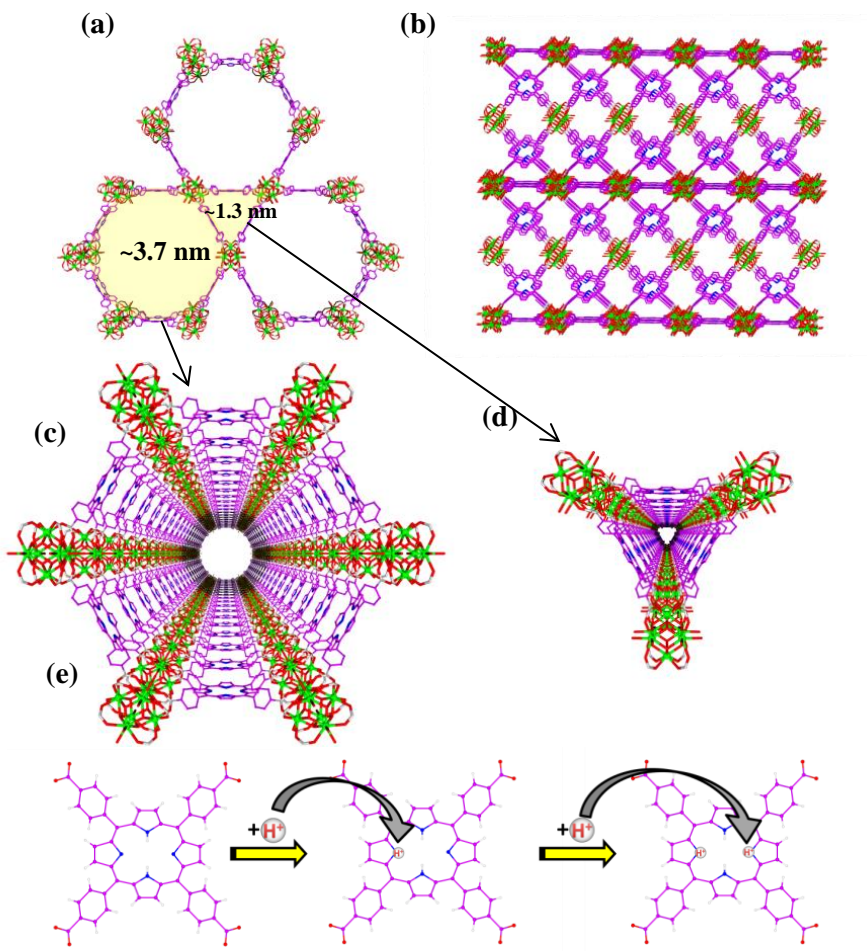


Figure 3.1. Structural drawings of PCN-222 along the crystallographic c axis (a), and a axis (b); images showing the accessibility of the porphyrin linker from inside the ~3.7 (c) and ~1.3 (d) nm diameter pores; protonation of the H_2tcpp linker (e).

The MOF also contains one dimensional open channels of 3.7 and 1.3 nm diameter lined by the porphyrin moieties that allows for easy passage of analyte or substrate molecules as well as direct

interaction with the porphyrin subunits (Figure 3.1). It is worth noting that PCN-222 can be constructed using metallated tcpp (M-tcpp), however for this study the metal free ligand was chosen.

3.2 Experimental Details

All chemicals used for this study were purchased from commercial sources and used without further purification. Zirconium chloride (99+%), benzoic acid (99%), N,N-diethylformamide (DEF, 99%), acetic acid (99 %), hydrochloric acid (36.5-38%, for concentrated solutions only) were purchased from Alfa Aesar, hydrochloric acid (0.1 N) from Electron Microscopy Sciences, sodium hydroxide (0.1000 N) from VWR, N,N-dimethylformamide (DMF, 99+%) from Oakwood Products Inc, and H₆tcpp (>97 %) from Tokyo Chemical Industries (TCI).

3.2.1 Material Synthesis

Crystalline product was obtained using the reported synthesis method. H₆tcpp (50 mg) was added to a 30 mL glass vial containing benzoic acid (2.7 g) as a modulating acid. Zirconium chloride (75 mg) was added to the vial last followed by the immediate addition of N,N-diethylformamide (8 mL). The reaction vial was capped, sonicated for ~3 mins (Branson 2510) and heated at 120°C for 48 hours. Product was collected by vacuum filtration and washed with DMF and acetone. The product was then soaked in DMF for three days, replacing with fresh DMF daily to remove residual modulating agents and unreacted ligand. Product yield was 79.2% (0.1014 g) based on zirconium chloride.

3.2.2 Sample Preparation

The as synthesized sample was further prepared for study by soaking in DMF (40 mL) and 8 M HCl (1.5 mL) at 120°C for 24 hours. At the end of this time, the DMF/HCl mixture was carefully decanted off and replaced with 40 mL of acetone. Fresh acetone was replaced daily for three days. The product was again vacuum filtered and washed once with DMF and acetone and

dried in a vacuum oven at $\sim 100^{\circ}\text{C}$ under vacuum overnight. At this point the first PXRD measurement was taken ("activated PCN-222").

3.2.3 Experimental Methods

Double sided tape was applied to a quartz slide and a background measurement was taken. A thin coating of sample (~ 0.01 g) was applied to the tape and spread evenly with excess sample being removed by friction using both standard weighing paper and lens tissue. At this time measurements were taken on the film. Three to four drops of HCl solution were applied to the surface of the film and allowed to equilibrate with the sample, at which time the excess solution was blotted off with lens tissue and corresponding UV-Vis and PL measurements were taken. In order to reverse the effect of the acid, the film was washed thoroughly with water by immersion, followed by a drop-wise application of DMF to a kimwipe while covering the surface of the film.

3.2.4 Instrumental Details

All powder X-ray diffraction data were collected using a Rigaku Ultima-IV diffractometer. The patterns were collected between 3° and 40° of the 2θ at a scan speed of $1.5^{\circ}/\text{min}$. The optical absorption spectra of solid samples were collected on a Shimadzu UV-3600 spectrophotometer at room temperature. The baseline was taken on a BaSO_4 standard with a quartz slide with double-sided tape applied. Diffuse reflectance measurements were then taken, converted to the Kubelka-Munk Function and normalized. Photoluminescence measurements were carried out on a Varian Cary Eclipse spectrophotometer at room temperature on a quartz slide with double sided tape and sample evenly applied with excess sample removed by friction (see experimental details, Section 1). All data except for the excitation spectrum was normalized to emphasize the "turn-off-turn-on" response.

3.3 Results and Discussion

Single phase crystalline product was obtained and activated using the reported hydrothermal method and confirmed by powder X-ray diffraction (PXRD) (Figure 3.2).¹⁶⁷ To evaluate the potential of the material to serve as a reversible and stable material for pH sensing, the MOF was exposed to HCl and NaOH solutions varying in concentration to span the pH range of -1 (concentrated HCl) to ~12 (0.01 M NaOH). In regards to the materials' aqueous stability, it is worth pointing out that a sample of PCN-222 was immersed in water for a period of nine months, after which time a PXRD measurement was made showing that the structure is still largely intact compared to the simulated pattern; the subtle differences in the patterns are due to impurities that were present in the original sample. After this time the material took on a charcoal grey color, which is likely a result of replacing residual N,N-dimethylformamide (DMF) solvent molecules with water. While the material proves to be exceedingly stable in aqueous acidic conditions, a feature quite rare for MOFs, it was found that dissolution occurs somewhere between pH 11 - 12, which is consistent with the original report. In addition, we noted that when exposed to pH 2 solutions and lower, a very distinct color change from purple to green occurs (Figure 3.3a). While there is still a color change that occurs at pH 3 and upwards, it is less noticeable to the naked eye. Further study reveals that not only is the color change from purple to green instant and reproducible, but that it is also completely reversible. Below pH 0, no additional change occurs besides the intensifying of the green color. As seen in Figure 3.3a, in the case of PCN-222, the response is instant and pronounced. When PCN-222 was exposed to glacial acetic acid, which has a known pH of 2.4, the colorimetric response mimics that of the 0.01 M HCl (~ pH 2) solution, showing that this sensing effect is indeed due to pH and is both reversible and reproducible.

When the same set of experiments was performed using just the H₆tcpp ligand there was little initial response. This is likely due to the insolubility of H₆tcpp in aqueous acidic solution

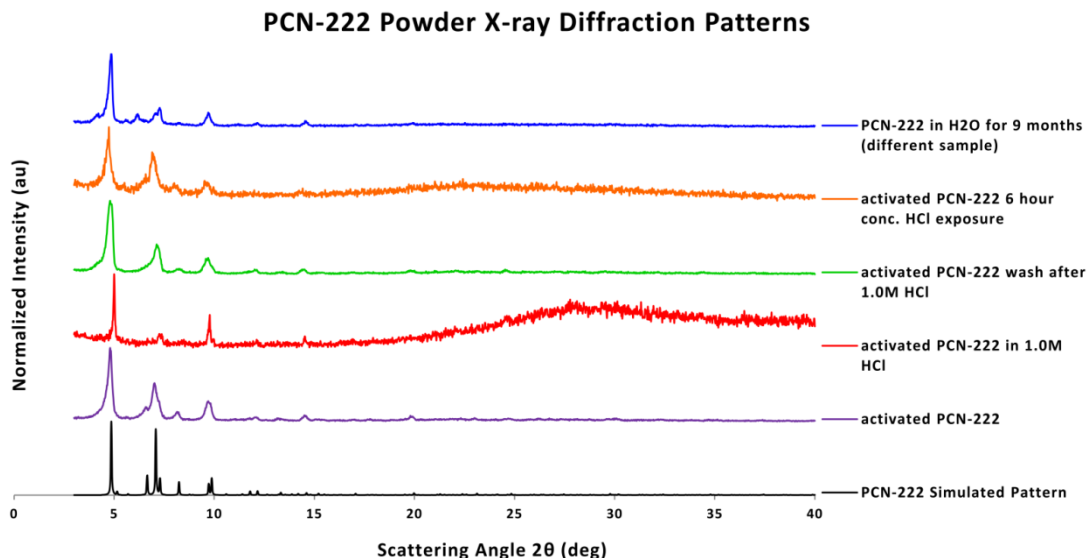


Figure 3.2. PXRD patterns: simulated pattern for PCN-222(Fe) (black); activated PCN-222 sample (purple); activated PCN-222 sample while immersed in 1.0M HCl (red); recovered 1.0M HCl sample washed with H₂O/DMF/acetone (green); recovered sample soaking in conc. HCl for 6 hours then washed with H₂O/DMF/acetone (orange); older/different sample of PCN-222 soaked in H₂O for 9 months (blue).

paired with its comparatively low available surface area, thereby limiting the protons' access to the majority of the nitrogen Lewis basic sites (LBSs) on the tetrapyrrolic macrocycle.¹⁵⁴ Eventually after thoroughly rubbing the acid solution into the sample, some small color change occurred in the case of 1.0 M HCl. Based upon previous studies of tetraphenyl porphyrin and its ability to act as a pH sensing molecule, we believe that this effect is also due to protonation of the nitrogen LBS present on the H₂tcpp linker.^{154, 159, 168} Upon photoexcitation, the porphyrin macrocycle can undergo both S₂ and S₁ transitions from a doubly-degenerate set of HOMOs and LUMOs resulting in the UV-Vis absorption Soret band, which occurs at ~450 nm for H₆tcpp, and the Q bands, which are the four smaller bands ranging ~520-660 nm (Figure 3.4).¹⁵⁵ It stands to reason that if this conjugated π system is perturbed, the molecule's UV-Vis spectrum will change

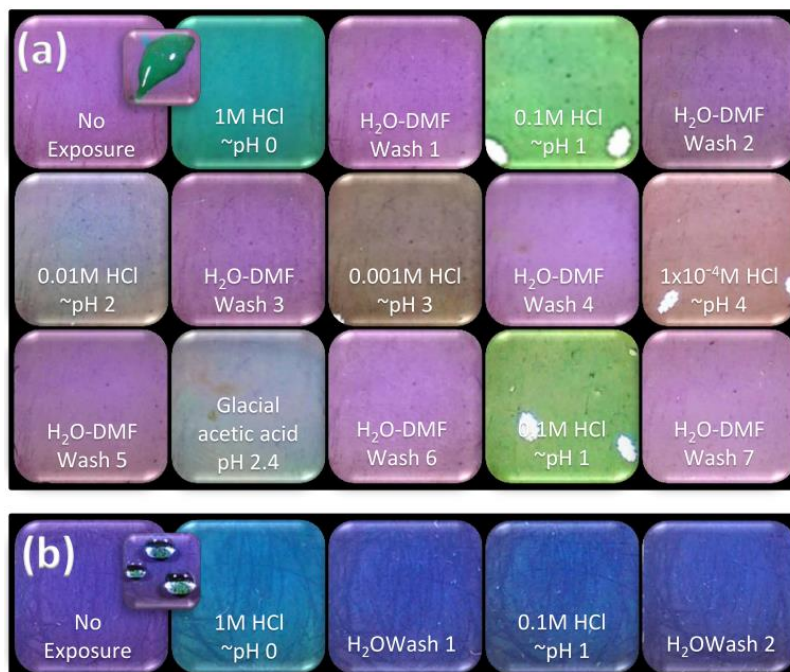


Figure 3.3. Photographs of PCN-222 samples (a) and ligand H_6tcpp (b) under ambient light. These samples are exposed to acidic solutions at various concentrations, followed by reversal washes in between each exposure; exposures were made in the order in which they appear from top left to bottom right. Caption photos are intended demonstrate responsiveness.

accordingly.

In order to verify that perturbation of the macrocyclic π system is responsible for the visible response, solid state UV-Vis reflectance measurements were taken on both the ligand (Figure 3.4) and the MOF before and after (Figure 3.5) acid exposure. In between each different pH exposure, PCN-222 was washed once with water and DMF in order to reverse the effect of the acid, resulting in a full return of the original purple color. In the event that the MOF is washed with just water alone, the material maintains a grey/brown color, the same color witnessed from pH 4 - 11, however DMF washing was omitted for the ligand due to its solubility in the

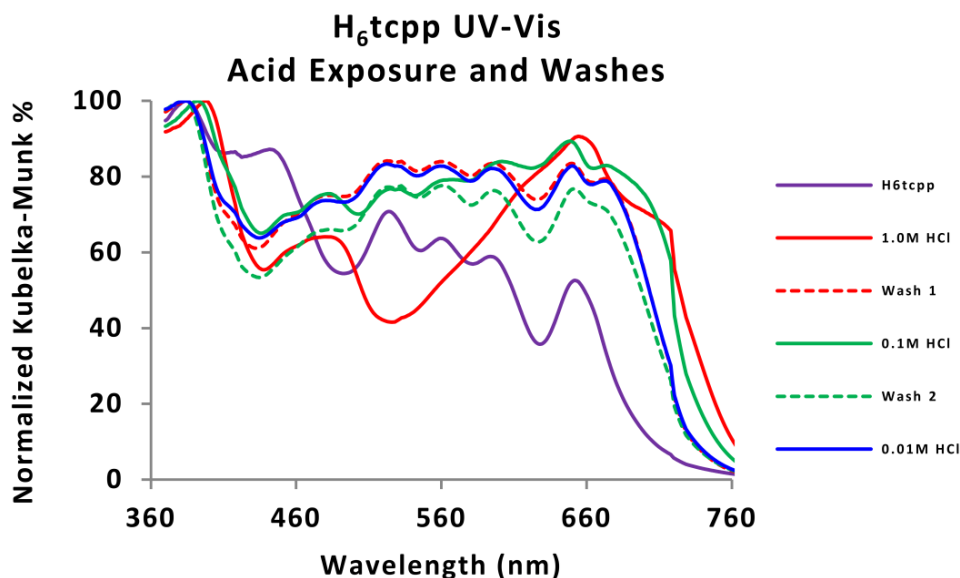


Figure 3.4. Solid state UV-Vis data for H_6tcpp collected after exposure to varying concentrations of HCl and reversal washes with H_2O .

solvent. As the results in Figure 3.5 demonstrate, as the acidity of the test solution increases, absorption corresponding to the high energy Soret band (~ 460 nm) and the lowest energy Q band (~ 660 nm) dramatically increase and are red shifted relative to the other three Q bands. These shifts correlate to the band-gap of PCN-222 decreasing from ~ 1.85 to ~ 1.7 eV (Figure 3.6). The net effect is that the material absorbs more red and blue light over a wider range resulting in a combination of orange and teal reflectance, which produces a greenish color when combined. Starting at 1.0 M HCl the three higher energy Q bands associated with the H_2tcpp are all but invisible from the absorption spectrum. Because these Q bands are a product of the different S_1 transitions of the porphyrin unit, protonation of the macrocycle results in a disturbance of the conjugated π electron system. This finding supports the reasoning that the color change effect arises from the degree of protonation and subsequent deprotonation of the H_2tcpp macrocycle within the structure. After exposure to 8.0 M HCl solution, there is a broadening of

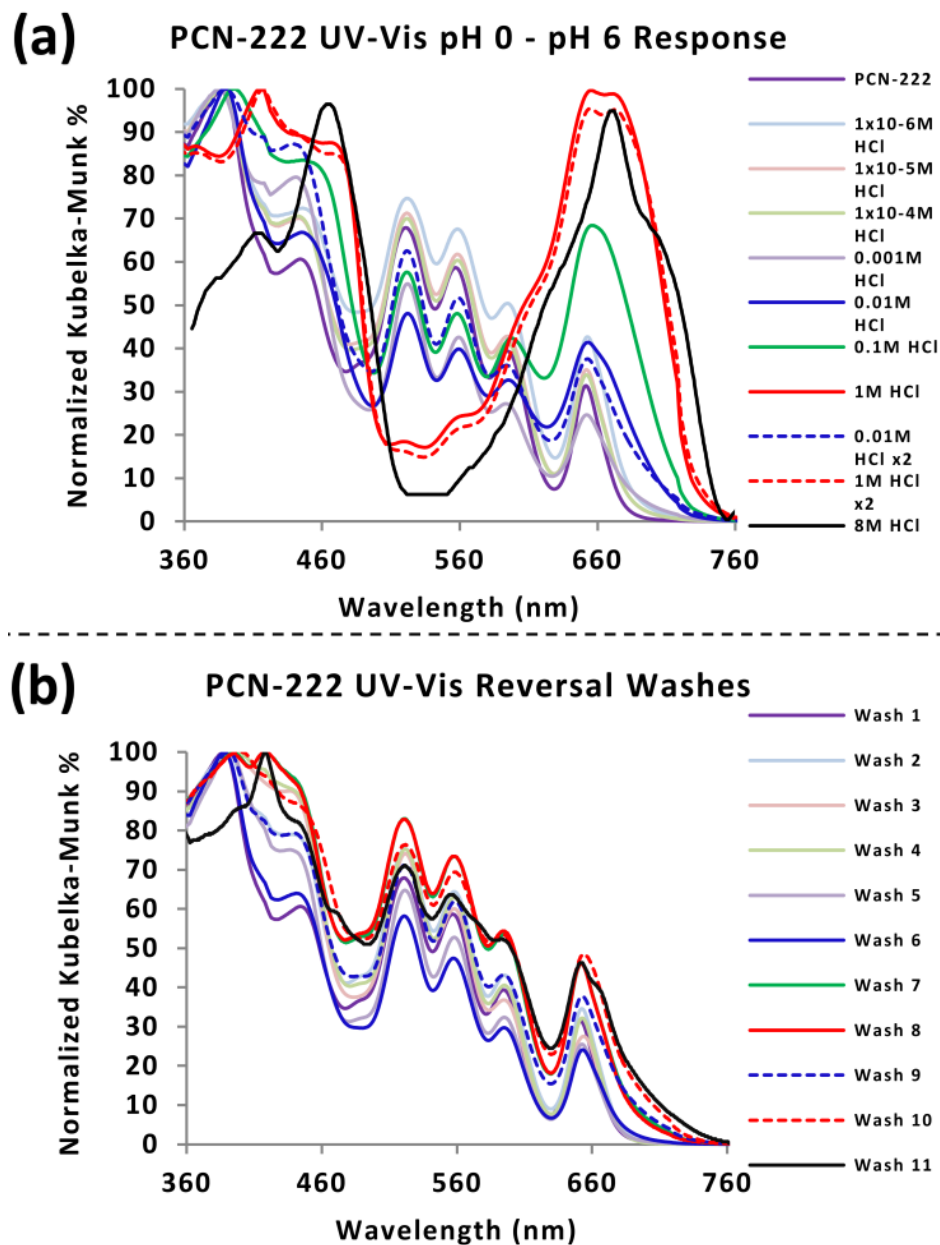


Figure 3.5. UV-Vis spectra for PCN-222 after exposure to varying concentrations of HCl solution (a) and after reversing the effect by washing with H₂O and DMF (b). Measurements were made in the order in which they appear in the legend from top to bottom, where Wash 1 corresponds to washing PCN-222 with no acid exposure.

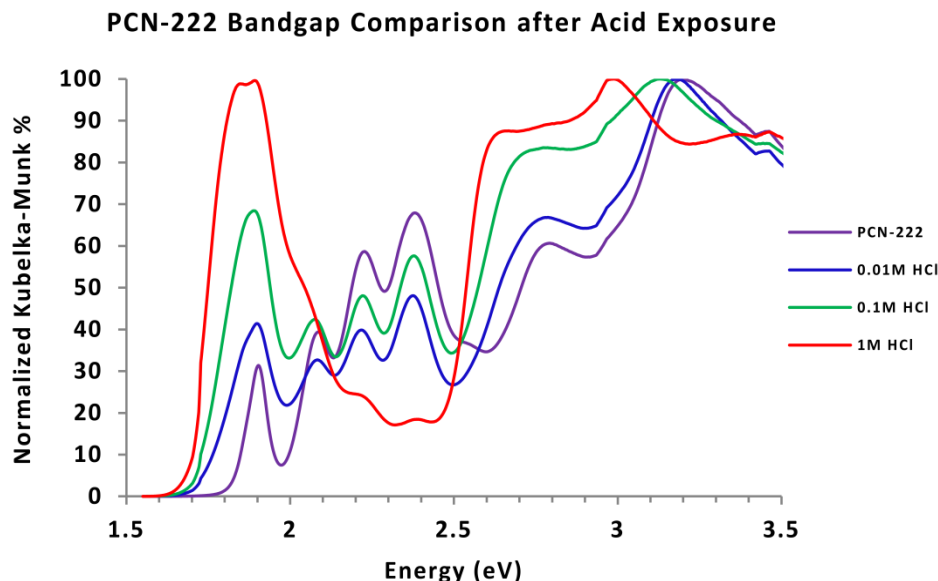


Figure 3.6. Solid state UV-Vis data for PCN-222 comparing bandgap energies after exposure to varying concentrations of HCl.

the low energy band from 690 nm to ~715 nm that persists even through washing. This effect is likely due to incomplete washing of the highly concentrated acid resulting in residual protonation.

To further investigate the colorimetric response, photoluminescence (PL) measurements were also taken (Figure 3.7) in a similar fashion to the UV-Vis measurements (370 nm excitation, Figure 3.8). These data show a very distinct "turn-off-turn-on" effect as a result of two separate phenomena. Significant quenching of the low energy emissions from about 645-760 nm results in a "turn-off" effect after exposure to < 0.01 M HCl solution. The UV-Vis absorption in this region (610-760 nm, Figure 3.5) is also increased accordingly. The purple color can be thought of arising from a combination of the green/blue high energy emission and red low energy emission, and as the low energy emission is quenched upon exposure to acid, only the high energy emission from about 450-560 nm is observed, hence the greenish blue color arises when exposed to 0.01 M HCl solution or glacial acetic acid (Figure 3.3). At low pH, from pH 0 (1.0 M HCl) downwards, two additional "turn-on" peaks are observed. The maximum peak at 490 nm shifts to 500 nm, and the

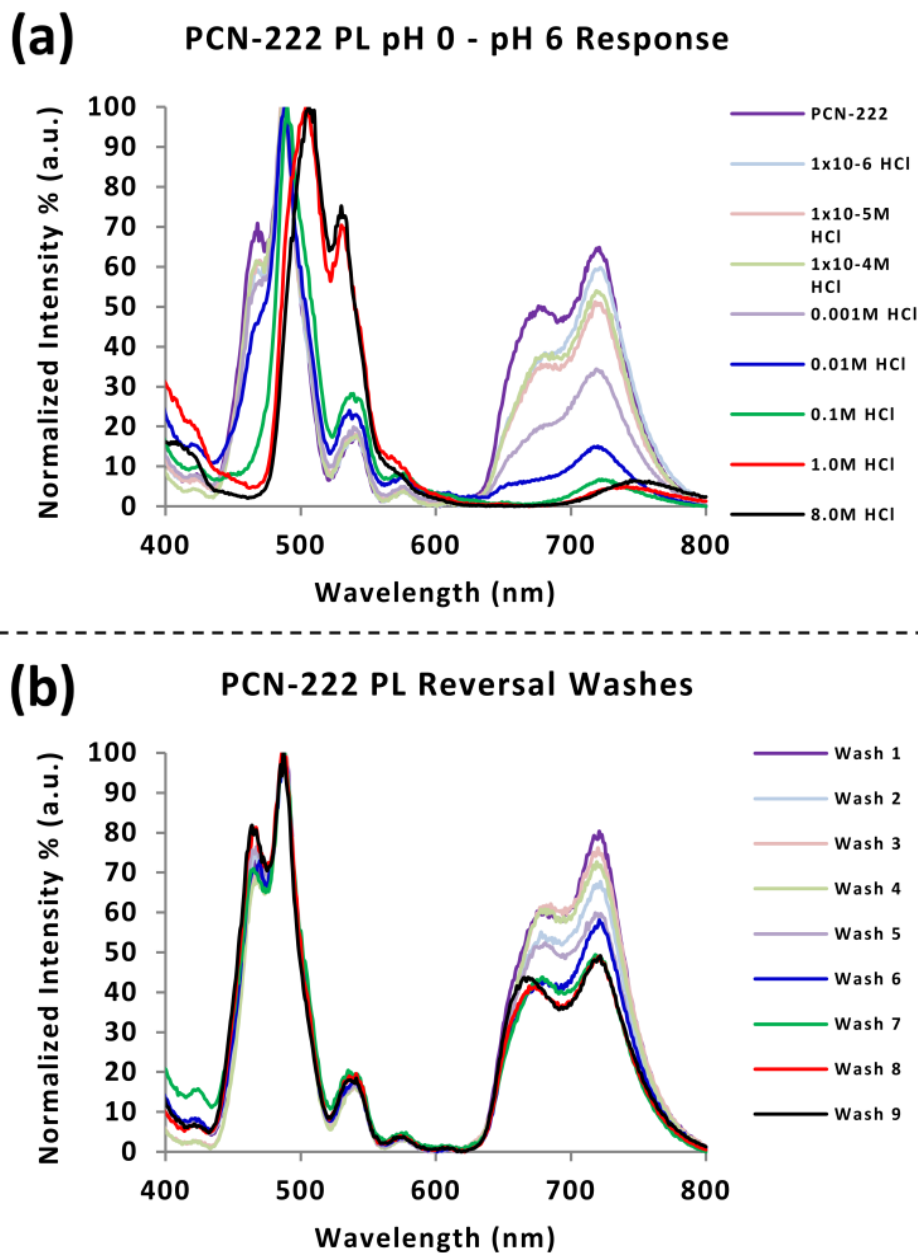


Figure 3.7. Photoluminescence data for PCN-222 after exposure to varying concentrations of HCl solution (a) and after reversing the effect by washing with H₂O and DMF (b). Measurements were made in the order in which they appear in the legend from top to bottom, where Wash 1 corresponds to washing PCN-222 with no acid exposure.

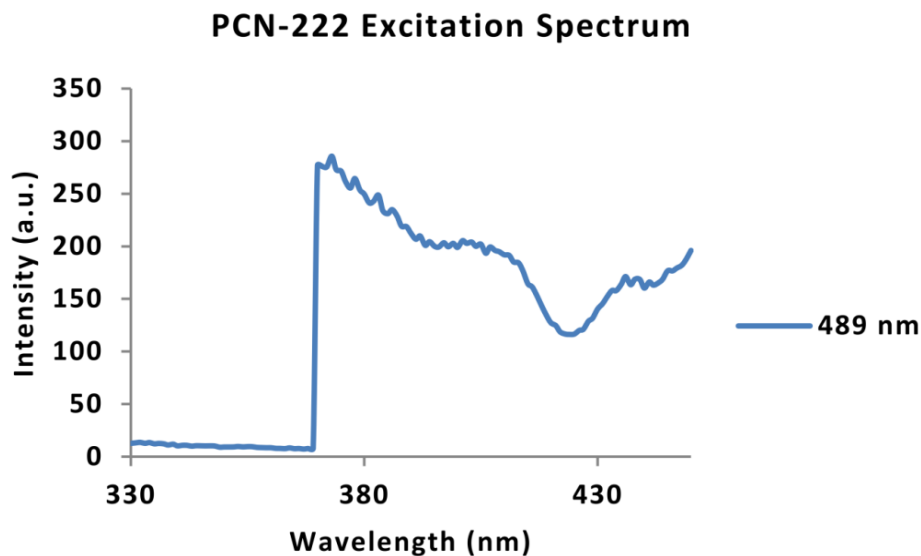


Figure 3.8. PCN-222 fluorescence excitation spectrum; monitored at 489 nm emission.

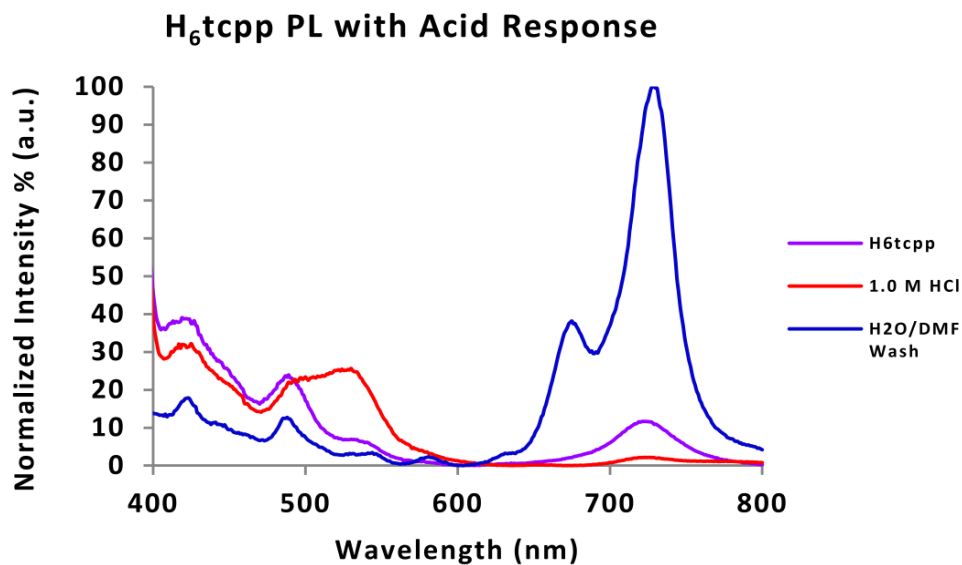


Figure 3.9. H₆tcpp solid state emission spectrum. Slide sample was prepared using the same method as for PCN-222.

peak at 525 nm is significantly enhanced in conjunction with the disappearance of the shoulder peak at 465 nm; at this point the material appears to be entirely green to the naked eye. Similar to

the UV-Vis measurements, the effect was completely reversed in between each different exposure (Figure 3.7b). In order to further support the claim that the color change is an effect of protonation/deprotonation of the H₂tcpp moiety, similar PL measurements were taken on a film comprised of just the H₆tcpp molecule (Figure 3.9). While the PL spectra are different from one another as expected, the response of H₆tcpp to acid exposure is similar in nature to PCN-222 (Figure 3.7a), with red shifting peaks in the high energy region and quenching in the low energy region. The PL data for the free ligand in the solid state also suggests activation of a new emission peak at ~675 nm after washing once with H₂O and DMF. It should be noted that while H₆tcpp is hydrophobic to the aqueous acid solutions, it dissolves freely in DMF. Due to the nature of the way the sample was washed, minimal dissolution occurred, but it may have been enough to disrupt any long range order within the free ligand, as the PL spectrum looks more similar to that of H₆tcpp when in solution. It should also be pointed out that when the H₆tcpp²⁺ diacid form of the ligand is dissolved in solution (through the use of co-solvents) it forms dimers and aggregates at low pH values.¹⁵⁴ The immobilization of the porphyrin unit within PCN-222 prevents formation of such aggregates and thus provides unique UV-Vis and PL optical responses.

3.4 Conclusion

In summary, we have shown that by incorporating the H₂tcpp moiety into the mesoporous crystalline framework, PCN-222, the sensitive optical response properties of the soluble porphyrin-derivative molecular species can be realized in an easily accessible and stable, solid state single phase bulk material and without the formation of aggregates.^{154, 159} Additionally, we have shown that the material has the advantage of full reversibility and reusability that outperforms its molecular analogues and is highly suitable to act as both a luminescent as well as colorimetric solid-state sensor for the low pH values covering a relatively wide pH range.

3.5 Preliminary Results of PCN-222 Photocatalytic CO₂ Reduction

The preceding work in Chapter 3 was discovered when PCN-222 was being prepared for evaluation as a photocatalytic CO₂ reduction catalyst. As the pioneer in the Jing Li research group with respect to catalytic CO₂ reduction, much time was spent establishing experimental methods, as well as sourcing and setting up instrumentation. By the time the catalytic study was underway, an almost exact mirror of our study was published in the Journal of the American Chemistry Society.⁴² For this reason, work on this particular project was terminated and instead, following reports of potential catalytic activity of Bi³⁺, work began on developing the bismuth based MOFs described in the following chapters.

CHAPTER 4. High-Performance Blue-Excitable Yellow Phosphor Obtained from an Activated Solvochromic Bismuth-Fluorophore Metal–Organic Framework ³⁵

[*Cryst. Growth Des.*, **2016**, 16 (8), pp 4178]:*Project coauthored by Ever Velasco; Appendix II

3.1 Introduction

Luminescent metal-organic frameworks (LMOFs) are currently being studied for use in multiple luminescence-based applications, including chemical sensing, biosensing and biomedical imaging, thermometry, and general lighting.^{43, 50, 140, 142, 171-175} Our group's recent work has established that LMOFs with strong yellow emission are potentially suitable to serve as the yellow phosphor in commercial blue light driven phosphor-converted white light-emitting diodes (PC-WLEDs),⁴⁴⁻⁴⁵ which are rapidly replacing traditional lighting technologies (incandescent, compact fluorescent), thanks to their lower energy consumption and longer lifetime.¹⁷⁶ A common type of PC-WLEDs utilizes a blue LED to excite a yellow phosphor, such as yttrium aluminum garnet doped with cerium (YAG:Ce³⁺), resulting in white light through the combination of the blue and yellow emissions.¹⁷⁷⁻¹⁷⁸ Most commercial yellow phosphors are based on rare-earth elements (REE), which are of limited supply yet rising demand, owing to their importance in numerous applications.¹⁷⁹ It is anticipated that over time both their demand and price will continue to rise. Thus, the development of alternative yellow phosphors that are free of REEs is highly desirable.¹⁸⁰

One approach to designing strongly emissive LMOFs is to integrate a strong organic fluorophore with desired optical properties along with a complementary metal. Previous work reveals that structures based on the tetraphenylethylene core, which has minimal fluorescence in solution but undergoes aggregation induced emission (AIE), show strong photoemission in the blue-yellow range when bound to a framework.^{44-46, 181-184} Further, our studies have shown that the 4', 4'', 4''', 4''''- (ethene-1,1,2,2-tetrayl) tetrakis((1,1'-biphenyl)-4-carboxylic acid)) (H₄tcbpe,

Figure 4.1) derivative has strong blue-excitable yellow emission (~ 550 nm), and has proven a prime candidate to construct blue-excitable yellow phosphors.⁴⁵ LMOFs constructed with tcbpe show higher internal quantum yields (QY) and improved chemical and thermal stability compared to the ligand.

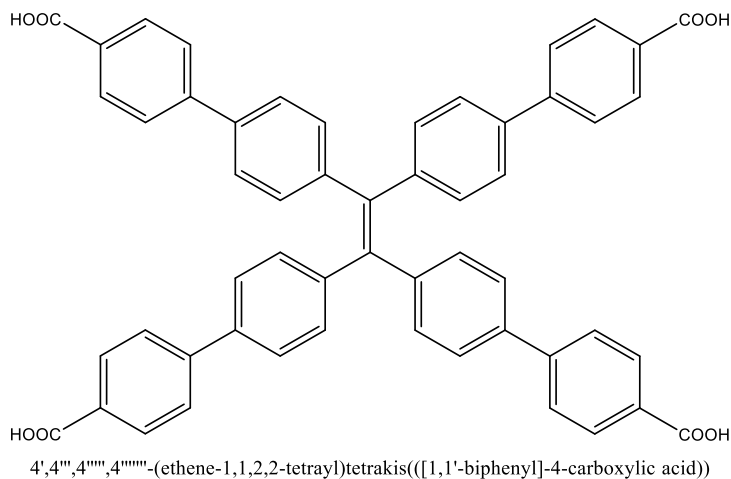


Figure 4.1. Structure of H_4tcbpe ligand.

Bismuth-based materials have previously gained attention for potential use in photoluminescence (PL) related fields.¹⁸⁵⁻¹⁸⁸ Currently, Bi has few commercial applications; it is used mainly in pharmaceuticals and as metallurgical additives. Bismuth is the only non-toxic heavy metal, and is most commonly obtained as a byproduct during Pb, Cu, W, and Sn ore refining.¹⁸⁹ Despite being the last radioactively stable element on the periodic table, the cost of bismuth is relatively low. According to the 2015 Mineral Commodities Survey by the U.S. Department of the Interior, the average price of Bi from 2010 to 2014 was $\sim \$22/\text{kg}$, which was about the same as the cost of Ni and about 50% cheaper than Co for the same time period. In comparison, the average costs of 1 kg of Ce_2O_3 , Eu_2O_3 , and Tb_2O_3 were $\sim \$25$, $\$1530$, and $\$1215$, respectively.¹⁹⁰

Bi^{3+} has a stereoactive lone-pair of $6s^2$ electrons, resulting in flexible and often hemidirected coordination geometry.¹⁹¹⁻¹⁹² Despite rich existing Bi-complex chemistry, and

fifteen-plus years of rapid MOF development with thousands of reported structures, there are still only a handful of reported bismuth based MOFs (we were able to establish < 20).¹⁹³⁻²⁰⁷ Notably, zur Loye and coworkers have reported a number of Bi coordination polymers and their fluorescence properties using pyridine dicarboxylate as ligand.²⁰⁷⁻²¹¹ Stock, Cheetham and coworkers have also reported a small variety of interesting Bi-MOFs.^{195-197, 201-202} We ascribe the scarcity of reported Bi based MOFs to a few factors: 1) flexible coordination geometry of Bi^{3+} , with the lone pair often resulting in hemidirected coordination polyhedra and densely packed 1-D and 2-D coordination polymers, 2) tendency of Bi^{3+} to form anionic frameworks as Bi has up to ten coordination sites, 3) hydrolysis reactivity of Bi^{3+} to form oxides and hydroxides, and 4) limited solubility of Bi^{3+} salts.

With these factors considered, we sought to optimize reaction conditions towards growing Bi-MOFs integrating the H_4tcbp e linker. By employing the large tetracarboxylate linker, void space between Bi^{3+} nodes is maximized allowing for more flexible ligand positioning and promoting the formation of 3-D structures. Potassium salt added during synthesis provides +1 charge balancing cations in the event of anionic framework formation. To slow both hydrolysis of the Bi^{3+} cation and MOF crystal growth, we use a significant excess of a competing carboxylate species (modulator). The utilization of mono-carboxylate species, such as benzoic acid and acetic acid, has proven a critical method for obtaining single crystals in MOF synthesis; this has proven especially effective in the case of zirconium based MOFs.²¹² Finally we use a bismuth cluster as the metal source in place of commonly utilized $\text{Bi}(\text{NO}_3)_3 \cdot 5\text{H}_2\text{O}$ to address solubility and hydrolysis concerns. Utilizing this synthetic strategy, a new BiK-tcbp e (**1**) LMOF was obtained and its optical properties were studied.

4.2 Experimental Details

Unless otherwise stated, all starting chemicals used in this study were reagent grade (>97%) and purchased from commercial sources. Except for benzoic acid, chemicals were used

as received without further purification. Benzoic acid was recrystallized in a hot 1:1 mixture of ethanol (EtOH) and deionized (DI) water.

4.2.1 Ligand Synthesis

The 4',4''',4''''',4''''''-(ethene-1,1,2,2-tetrayl)tetrakis((1,1'-biphenyl)-4-carboxylic acid) (H_4tcbpe) ligand was prepared using the reported method with slight modifications, as briefly outlined below.⁴⁵

Preparation of tetra-(4-bromo-phenyl)ethylene (tpe-Br)

Tetraphenylethylene (tpe, ~6.0g) was stored on a watch glass in a small glass desiccator over liquid Br_2 for one week in a fume hood (liquid Br_2 is particularly reactive and corrosive) with occasional careful mixing of the tpe powder and adding additional Br_2 if necessary. The crude orange product was recrystallized by dissolving in dichloromethane (DCM), followed by forced precipitation with methanol (MeOH), and was filtered and washed with additional MeOH.

Suzuki coupling between tpe-Br and 4-(methoxycarbonyl)phenylboronic acid

90 mL of tetrahydrofuran (THF) and 15 mL of 3 M aqueous K_2CO_3 were charged to a three neck round bottom flask. 2.85 g (4.4 mmol) of tpe-Br and 5.00g (27.8 mmol) of 4-(methoxycarbonyl)phenylboronic acid were added to the flask along with a condensing column and rubber septum, and was nitrogen purged multiple times. 0.20 g (0.2 mmol) of $Pd(Ph_3)_4$ was weighed in a glove box and stored in a vial with a septum under inert atmosphere. 10-15 mL of THF was used to dissolve the Pd catalyst, which was then injected to the purged reactor through the rubber septum and refluxed at 90 °C for 3 days with constant stirring (Note: $Pd(Ph_3)_4$ is very air sensitive). After cooling to room temperature, the crude ester product was extracted with DCM a minimum of three times, washed with water, dried over anhydrous magnesium sulfate and rotovapped to dryness. The crude product was then purified via flash chromatography using a

1:29 mixture of ethyl acetate:DCM as the mobile phase. The obtained purified ester is a green-yellow solid.

Base hydrolysis and acidification of the tcbpe-ester to form H₄tcbpe

2.43 g (2.8 mmol) of the tcbpe ester was dissolved in 30 mL of THF in a round bottom flask; 30 mL of 3 M KOH was then added and heated to reflux (90 °C) with vigorous mixing. After a minimum of 6 hours of reflux, the reaction was cooled to room temperature and concentrated via rotary evaporation to remove organic solvent. The remaining reaction slurry was added dropwise to 6 M HCl, resulting in precipitation of the carboxylic acid which was then filtered and washed with DI water until pH neutral and dried under vacuum. The final product was confirmed by NMR. Note: if HCl was added to the reaction slurry for the acid workup, often the ligand will crash out of solution as the potassium salt form, which is a white powder with blue PL emission. Adding the slurry to an acid solution prevents this from occurring.

4.2.2 Bi₄O₂(Hsal)₈·2MeCN Synthesis

The tetranuclear bismuth cluster Bi₄O₂(Hsal)₈·2MeCN (H₂sal = salicylic acid) was prepared at room temperature following the reported conditions.²¹³ 0.11 g (0.25 mmol) of triphenyl bismuth and 0.10 g (0.75 mmol) of salicylic acid were added to a 20 mL scintillation vial and dissolved in 1.4 mL of acetonitrile (MeCN) with sonication. The solution was then left undisturbed for a few days while crystal clusters of the product formed. The reaction supernatant was decanted and the crystalline product was washed with toluene (3x). Phase purity was confirmed via PXRD.

4.2.3 [BiK(tcbpe)(DMF)₂]_xDMF Synthesis

Single crystals of [BiK(tcbpe)(DMF)₂]_xDMF suitable for diffraction studies were obtained solvothermally. Bi₄O₂(Hsal)₈·2MeCN (10.0 mg, 0.005 mmol), H₄tcbpe (20.0 mg, 0.025 mmol), KCl (3.0 mg, 0.040 mmol) and benzoic acid (200 mg, 1.64 mmol) were added to a 20 mL

scintillation vial with 2 mL of DMF and sonicated for 2 mins. The reaction vial was placed in a pre-heated 100 °C oven for 5 days. Plate-like colorless crystals were collected via vacuum filtration and washed with DMF. The product yield based on Bi is ~77.1%. This reaction was also scaled up with similar yields by doubling reactant quantities in 3 mL of DMF. Decreasing the quantity of benzoic acid slightly improves the reaction yield and results in smaller particle sizes. When $\text{Bi}(\text{NO}_3)_2$ or BiPh_3 were used directly in place of the cluster as the metal source, mixed phases and different products were obtained, respectively.

4.2.4 Activation Procedure and Solvochromic Studies for the Transformation of **1** to **1A**

The solvochromic properties of **1** were studied through incremental desolvation with corresponding TGA, PXRD and optical measurements. The TGA weight loss from ~50-160 °C was used to calculate the average DMF content per formula unit, including coordinated DMF. The ~5% weight loss observed in the TGA profiles after 170 °C is attributed to ligand degradation, and is also observed in the TGA profile of the pure H_4tcbpe ligand. We describe here the exact methods used to obtain the varying degrees of desolvation.

As-made samples were kept in a vial with a small tissue dampened with DMF to prevent drying and chromic shifts; TGA shows an approximate DMF content of 5.3 (per formula unit) with a 26.7% weight loss at this state. By allowing the sample to sit in open-air for less than one hour, the DMF content decreases to ~5.1. After continued exposure to ambient lab conditions, the DMF content further reduces to ~3.7 and ~3.1 after 20 and 40 hours, respectively. To obtain additional states of desolvation, samples of **1** were heated to 90 °C for varying times using the isotherm function of the TGA. Following each heating period, a full TGA measurement was made to establish the remaining DMF content. Specifically, heating ~2 mg samples of **1** using this method for 13, 20, 24, 27, 34, and 800 minutes result in approximate DMF contents of 2.3, 1.8, 1.5, 1.1, 0.9, and 0.3, respectively. To fully activate the sample (henceforth denoted as **1A**), **1**

was simply placed on a watch glass in a 90 °C oven for five days, at the end of which point the estimated DMF content is 0.0.

1 can also be activated to **1A** through solvent exchange and removal of volatile solvents. After soaking samples of **1** overnight in acetone, dichloromethane, ethanol, methanol, and acetonitrile, the solvents were decanted and the powder was allowed to dry. The TGA profile for the CH₂Cl₂ is the same as for the 5 day 90 °C treated sample, and the PL QY was as high as 76% at 455 nm excitation. This also suggests that the effect of heating **1A** for 5 days at 90 °C on PL QY is minimal (74% @455 nm). **1** was immersed in H₂O overnight, which results in instantaneous transformation to yellow emission (69% @455 nm QY), but the PXRD pattern is lacking the two characteristic peaks of **1A**.

4.2.5 PC-WLED Coating

~ 10 mg of **1A** was gently ground in a mortar and pestle and added to a scintillation vial; 0.5 mL of CH₂Cl₂ was added and the mixture was sonicated for two minutes. The suspension was drop-cast onto the surface of the LED and was allowed to dry in between coatings. The 10 W 450-455 nm LED chip was powered by a 12V DC power supply at a bias of ~9V.

4.2.6 Instrumental Details

Single Crystal X-ray Diffraction (SXRD) and Powder X-ray Diffraction (PXRD)

Single crystal diffraction data for **1** was collected at 100 K on a Bruker APEXII CCD diffractometer using the synchrotron source ($\lambda = 0.77490 \text{ \AA}$) at the Advanced Light Source 11.3.1 Chemical Crystallography beamline. The refinement method used was full-matrix least-squares on F². PXRD patterns were recorded on a Rigaku Ultima IV X-ray diffractometer with Cu K α radiation ($\lambda = 1.5406 \text{ \AA}$). A graphite monochromator was used and the generator power settings were set to 40 kV and 44 mA. Data were collected between 3-35° 2 θ with a step size of 0.02° and a scan speed of 1.5 deg/min.

Thermogravimetric Analysis (TGA)

Measurements were performed using a TA Q5000 Thermogravimetric Analyzer with a temperature ramp of 10 °C/min from room temperature to 600 °C under nitrogen gas flow (20 mL/min). For sample activation, the isotherm setting of the TGA was used to hold the sample at a specified temperature for set durations under nitrogen flow.

Ultraviolet-visible (UV-Vis) Spectroscopy

The optical absorption spectra of solid samples were collected on a Shimadzu UV-3600 spectrophotometer at room temperature. The baseline was taken on a BaSO₄ standard. Samples were prepared on a quartz sample holder and diffuse reflectance measurements were converted to absorption using the Kubelka-Munk Function.

Photoluminescence (PL) Spectroscopy

PL excitation and emission spectra were measured on a Varian Cary Eclipse spectrophotometer at room temperature. A quartz slide was used as the sample holder. Emission spectra were first collected using an excitation wavelength of 360 nm. The emission maximum was set as the monitored emission wavelength for the corresponding excitation spectra.

Internal Quantum Yield (QY) Measurements

The fluorescence internal quantum yields were measured on a Hamamatsu C9220-03 system with a 150 W xenon monochromatic lamp and an integrating sphere. Sodium salicylate (60% QY) and yttrium aluminum garnet doped with cerium (YAG:Ce³⁺, 95% QY) were used as standards at 360 and 455 nm wavelengths, respectively.

4.3 Results and Discussion

Single crystals of [BiK(tcbpe)(DMF)₂] \cdot xDMF (**1** or **LMOF-401**, Figure 1a, DMF = dimethylformamide), were obtained solvothermally in DMF (100 °C, 3 days) with excess

benzoic acid added as a synthetic modulating agent (see Experimental Details for synthetic conditions). A Bi-salicylate cluster was selected as the metal source, owing to its ease of preparation, air stability, and solubility in DMF.²¹³ Reactions using $\text{Bi}(\text{NO}_3)_3$ or BiPh_3 as the metal source in place of the cluster resulted in mixed phases and different products, respectively. **1** crystallizes in a monoclinic crystal system with a C2/c space group (Table 4.1); the asymmetric unit has one K^+ , Bi^{3+} , tcbpe and two DMF molecules. The Bi^{3+} building unit is coordinated to nine oxygen atoms with hemidirectional coordination geometry owing to bismuth's lone pair (Figure 4.2). Four carboxylates from four tcbpe linkers form bidentate coordination bonds to Bi^{3+} , with the last oxygen from coordinated DMF. The overall structure can be described as two interpenetrated 4,4-connected anionic 3-D nets comprised of distorted tetrahedral Bi^{3+} and rectangular tcbpe building units (Figures 4.2b, c and d). The Bi^{3+} building unit has highly distorted hemidirected tetrahedral geometry with respect to linker connectivity (Figure 4.2b). Two planes are formed by two each of the four linkers which extend throughout each net. The large linker size promotes some degree of linker flexibility, as observed by a slight warping of each rectangular tcbpe ligand. Potassium cations residing between Bi^{3+} building units form helical 1-D chains that connect and charge balance the two anionic nets through shared $\mu_3\text{-O}$ carboxylates and coordinated DMF, shown in Figure 4.2a as the yellow polyhedrons (see Figures 4.3 and 4.4 for additional structural depictions).

The observed Bi-carboxylate bonding features align with those reported previously for hemidirected Bi coordination polyhedrons.^{197, 201-202, 207} Each carboxylate pair has one short and one long Bi-O bond, and one of the four carboxylates has slightly longer distances in both cases. The three short Bi-O carboxylate bond distances are 2.245, 2.283 and 2.336 Å, with corresponding longer Bi-O bonds at 2.619, 2.641, and 2.657 Å, respectively. The last carboxylate has longer distances of 2.480 and 2.705 Å. The coordinated DMF is responsible for longest Bi-O bond (2.884 Å) resulting in gyroelongation of the Bi^{3+} polyhedron, and shares a $\mu_3\text{-O}$ bond with

Table 4.1. Crystal data and structure refinement for **1** (LMOF-401).

Identification code	BiK-tcbpe	
Empirical formula	C ₆₀ H ₄₆ Bi K N ₂ O ₁₀	
Formula weight	1203.07	
Temperature	100(2) K	
Wavelength	0.7749 Å	
Crystal system	Monoclinic	
Space group	C2/c	
Unit cell dimensions	a = 32.0791(13) Å	α = 90°
	b = 11.9048(5) Å	β = 99.269(2)°
	c = 37.7384(15) Å	γ = 90°
Volume	14223.9(10) Å ³	
Z	8	
Density (calculated)	1.124 Mg/m ³	
Absorption coefficient	2.793 mm ⁻¹	
F(000)	4816	
Crystal size	0.080 x 0.070 x 0.015 mm ³	
Theta range for data collection	2.112 to 27.898°.	
Index ranges	-38 ≤ h ≤ 38, -14 ≤ k ≤ 14, -45 ≤ l ≤ 45	
Reflections collected	60475	
Independent reflections	13085 [R(int) = 0.0804]	
Completeness to theta = 27.706°	100.0 %	
Absorption correction	Semi-empirical from equivalents	
Max. and min. transmission	0.959 and 0.784	
Refinement method	Full-matrix least-squares on F ²	
Data / restraints / parameters	13085 / 77 / 665	
Goodness-of-fit on F ²	1.023	
Final R indices [I > 2σ(I)]	R1 = 0.0465, wR2 = 0.1112	
R indices (all data)	R1 = 0.0628, wR2 = 0.1168	
Extinction coefficient	n/a	
Largest diff. peak and hole	1.507 and -2.714 e.Å ⁻³	

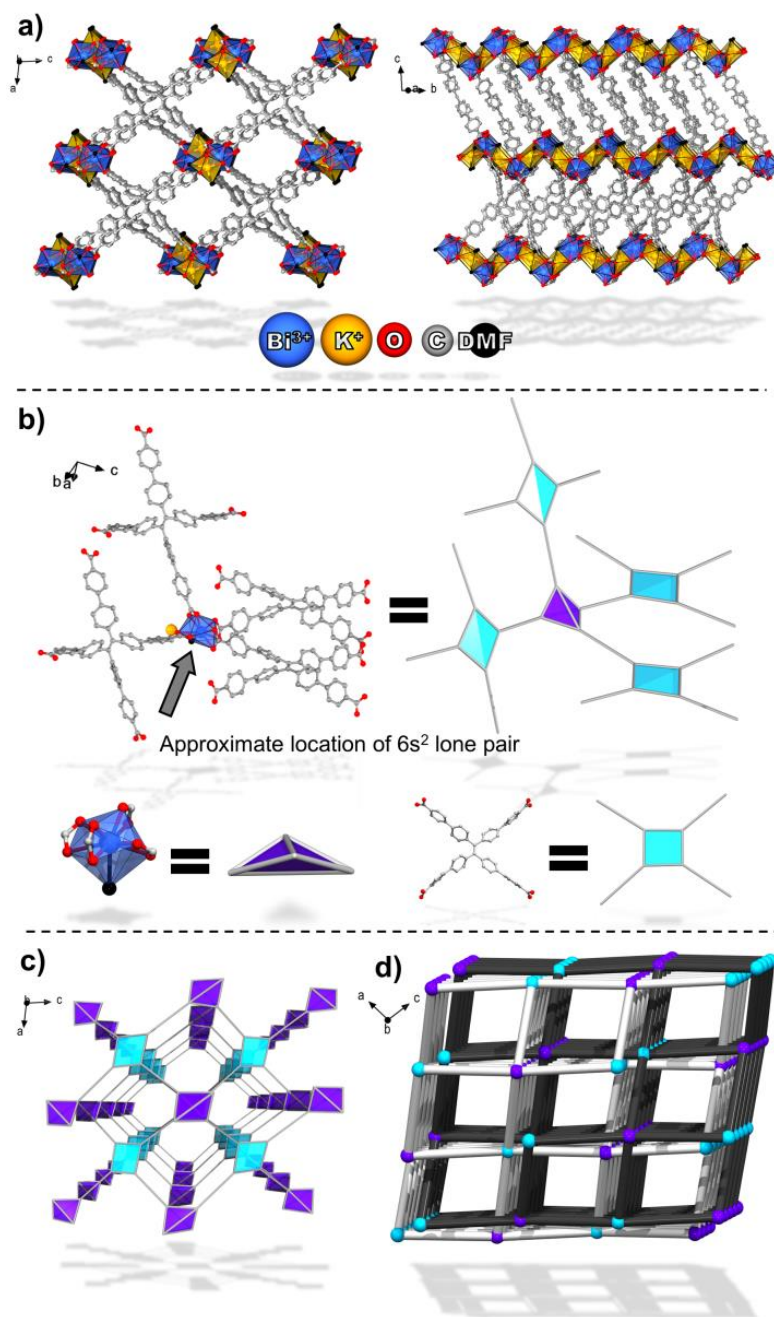


Figure 4.2. a) Structure plots of **1** along the crystallographic b-axis (left) and slightly rotated from the a-axis (right). b) Coordination geometry of Bi^{3+} with approximate location of $6s^2$ lone pair and polyhedral representation. c) Single Bi-tcbpe 4,4-connected net along the b-axis. d) Line connectivity drawing showing the two-fold interpenetration of the Bi-tcbpe nets.

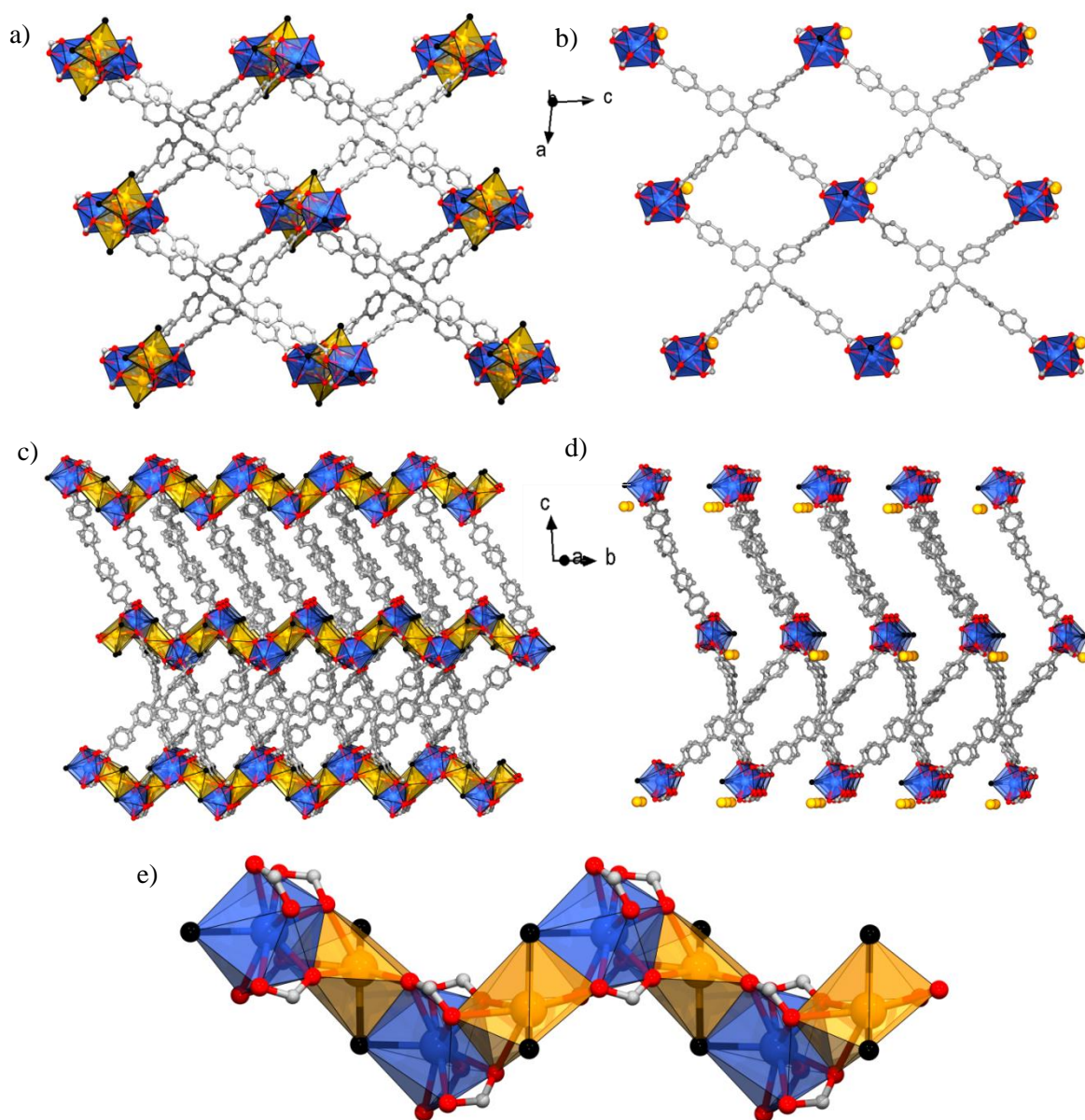


Figure 4.3. Structure plots of **1** along the b-axis (a, b) and a slightly rotated a-axis (c, d); b) and d) show the connectivity of a single Bi-tcbpe net with potassium bonds removed. e) Close-up view of the inorganic Bi-K chain formed through μ_3 -O carboxylate and DMF oxygens (red and black spheres, respectively).

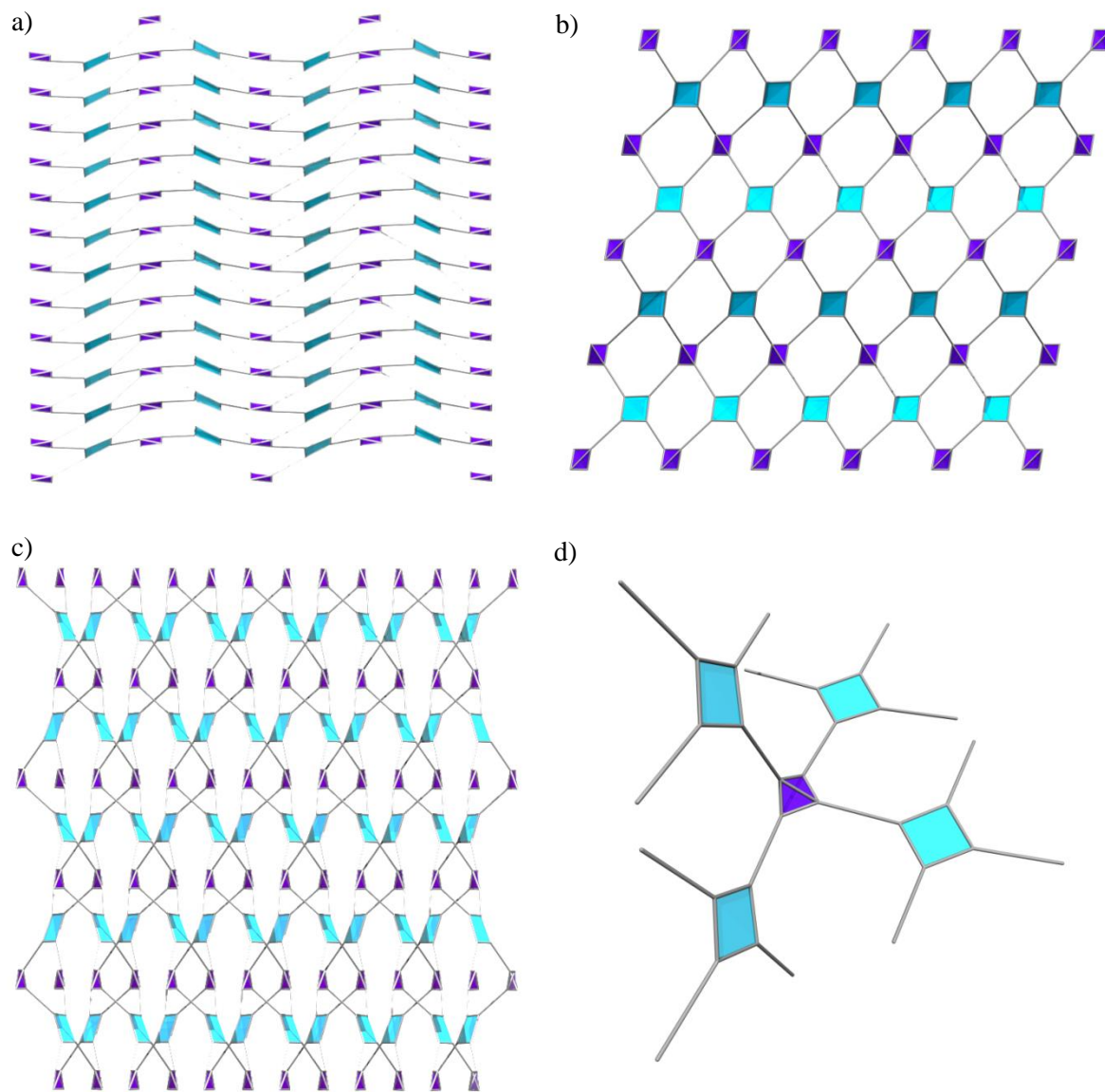


Figure 4.4. Polyhedral representation of the individual Bi-tcbpe nets in **1** as viewed along the crystallographic *a*, *b* and *c* axes (a, b, and c, respectively). d) Connectivity of the highly distorted tetrahedral and rectangular building units.

K^+ (2.663 Å). Potassium coordinates to the other structural DMF molecule through a lone coordination bond (2.639 Å). The rest of the coordination sphere around K^+ is comprised of shared oxygen atoms from the longest five Bi-O carboxylate bonds. The shortest of these K-O interactions (2.600 Å) corresponds to the longest Bi-O carboxylate, with the rest of the bond distances falling between 2.719 and 2.950 Å. Through these shared carboxylate and DMF oxygen atoms, a 1-D helical chain is formed connecting the two interpenetrated Bi-tcbpe frameworks.

Significant changes in the materials' optical absorption and emission properties were observed after desolvation of the framework, resulting in a highly emissive blue-excitable yellow phosphor when fully "activated" (Figure 4.5). This transformation was studied by incrementally desolvating **1** under controlled conditions. The results show evidence of strong solvochromism with respect to DMF content, and irreversible structural and optical changes upon full activation, which likely corresponds to removal of coordinated DMF.

As-made crystals of **1** (Figure 4.5a, left) are near colorless and have an approximate optical band-gap of 2.70 eV, as estimated from the optical absorption spectrum (Figure 4.6). Photoexcitation at 360 nm results in strong blueish PL emission with a peak maximum of 459 nm (Figure 4.5b, black curve, see Figure 4.7 for excitation spectrum) and an internal QY of 57.7% ($\pm 0.3\%$, Table 4.1). The thermogravimetric (TG) data for as-made **1** shows 26.7% weight loss corresponding to ~ 5.3 calculated DMF molecules per formula unit (Figure 4.8). The TG profile has stepwise weight-loss up to ~ 160 °C, which includes both guest and coordinated DMF molecules. As the structure was desolvated incrementally through both ambient exposure and heating under nitrogen flow, changes in solvent content, optical absorption and emission, and structure were monitored (see Experimental Details 4.2.4). Figures 4.5b and 4.7 show the PL emission of **1** at various stages of solvent removal, and corresponding CIE (Commission International de l'Eclairage) coordinate plots are shown in Figure 4.5c. The colored legend at the

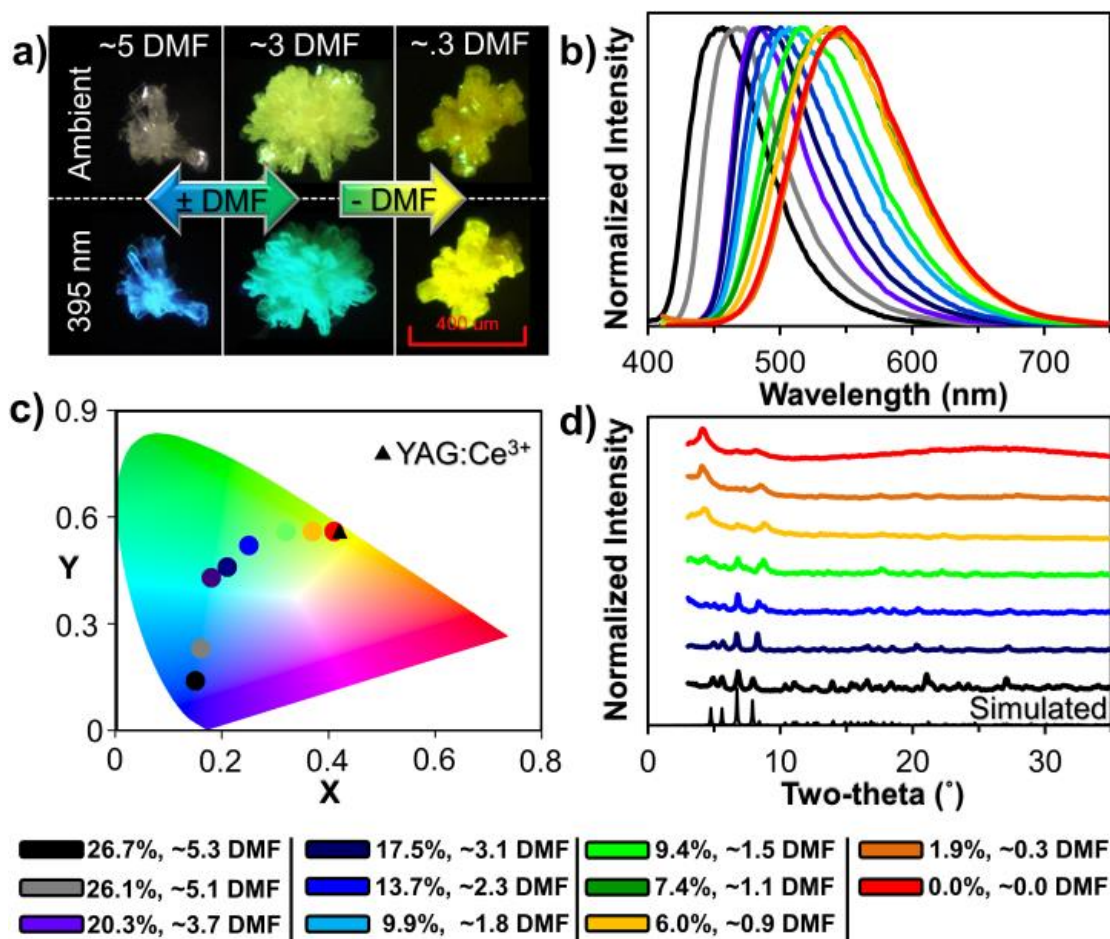


Figure 4.5. Data for 1 at various stages of desolvation. The colored legend lists the percent weight and estimated number of DMF (per formula unit) remaining in the sample. a) Optical micrographs under ambient light (top row) and 395 nm UV light (bottom row). b) Emission spectra, $\lambda_{\text{ex}} = 360$ nm. c) CIE coordinates calculated from the PL spectra. d) PXRD patterns showing structural changes in response to DMF content.

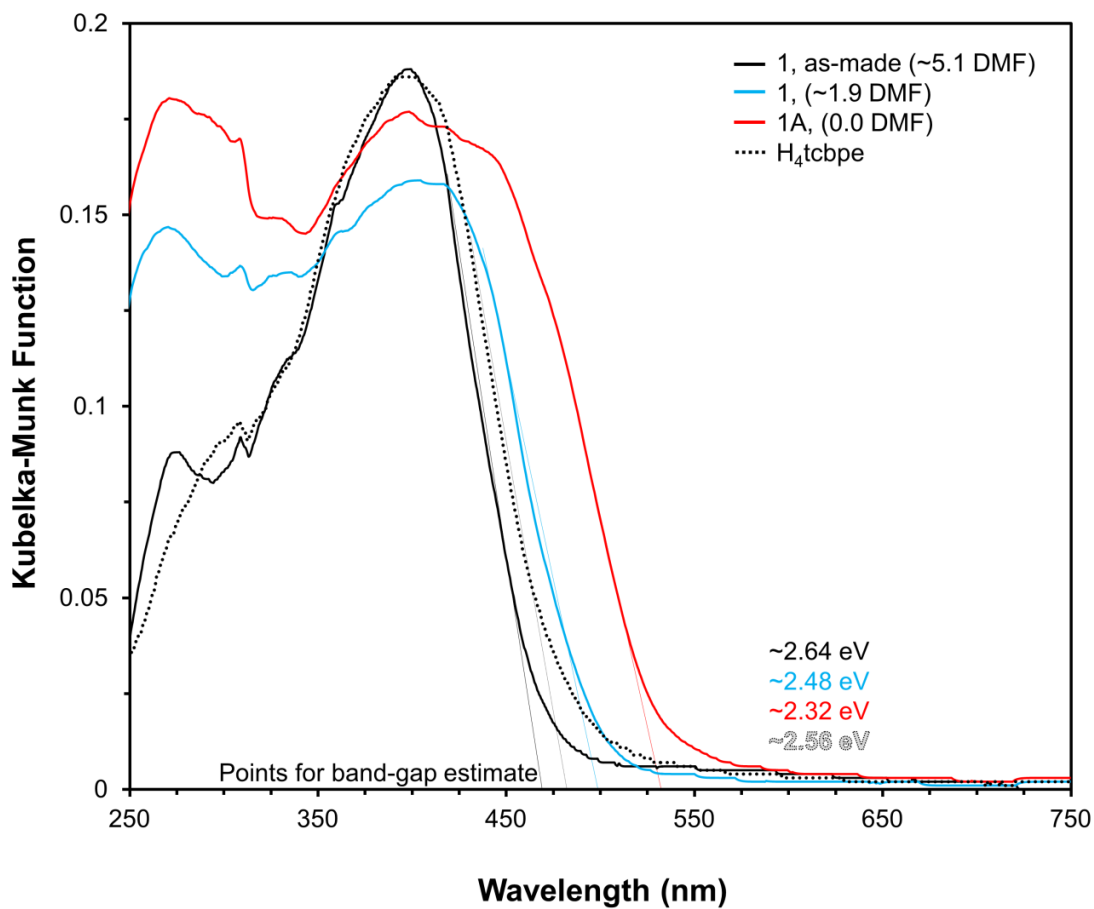


Figure 4.6. UV-Vis spectra of **1** (black), partially desolvated **1** (sky blue), **1A** (red), and H₄tcbpe (dotted black). Corresponding lines were added to show the positions used to estimate the optical band gap, which are listed in the bottom right.

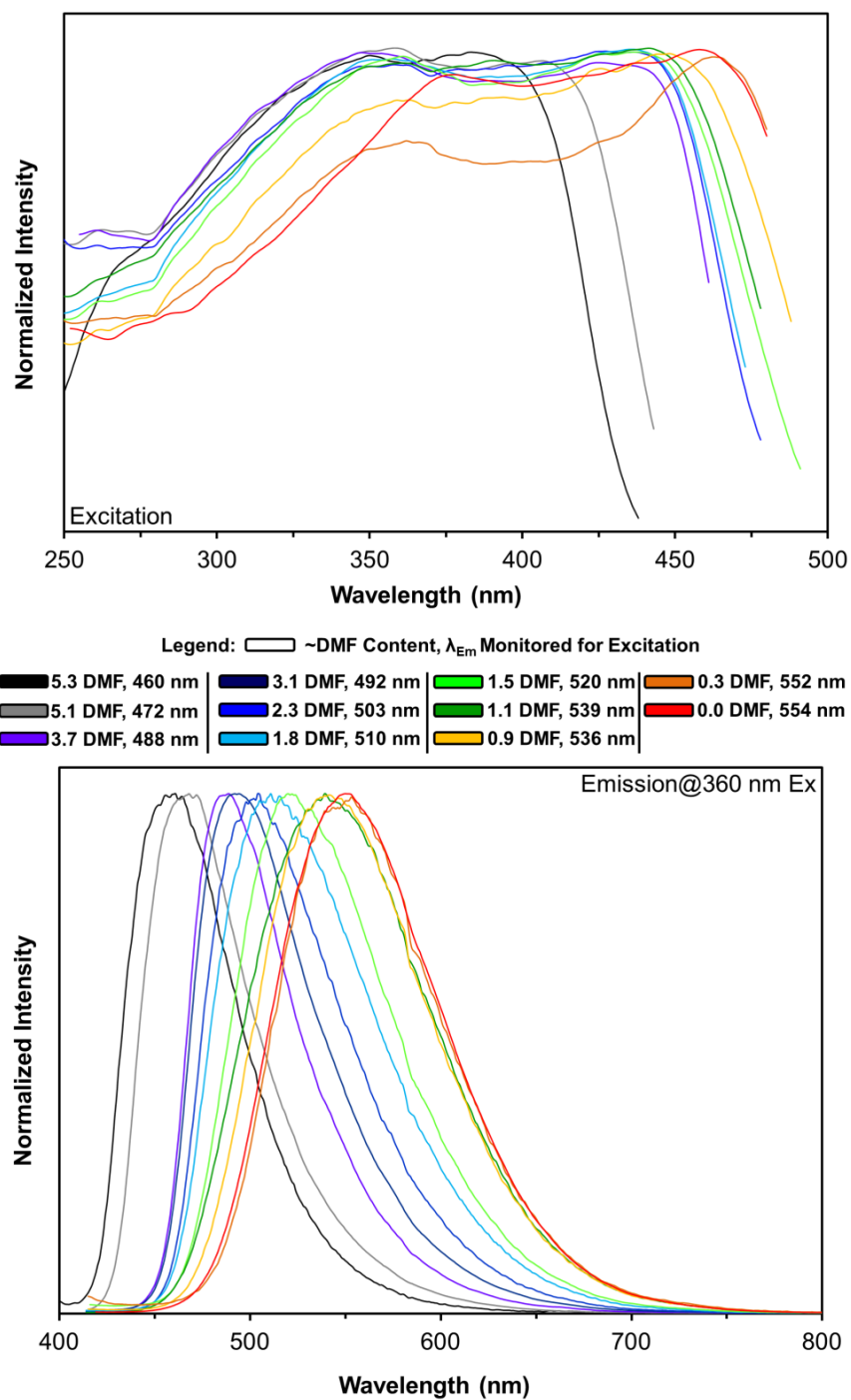


Figure 4.7. PL excitation (top) and emission (bottom) spectra for 1 at various stages of desolvation. The colored legend lists the approximate DMF content per formula unit, and the emission maximum wavelength (λ_{ex} = 360 nm) used for monitoring during excitation measurements.

Table 4.2: Quantum yield values obtained at different excitation energies.

Sample	QY@360 nm ($\pm 0.3\%$)	Avg. λ_{max} (nm)	QY@455 nm ($\pm 0.3\%$)	Avg. λ_{max} (nm)	Activation Procedure
1 , as-made (~5.1 DMF)	57.7	462	-	-	
1A	71.5	544	74.3	554	5d 90°C
1 @acetone	63.6	539	71.9	548	
1 @CH ₂ Cl ₂	63.6	537	76.0	546	
1 @H ₂ O	59.4	539	69.4	555	
H ₄ tcbpe (as-made)	-	-	62.3	556	

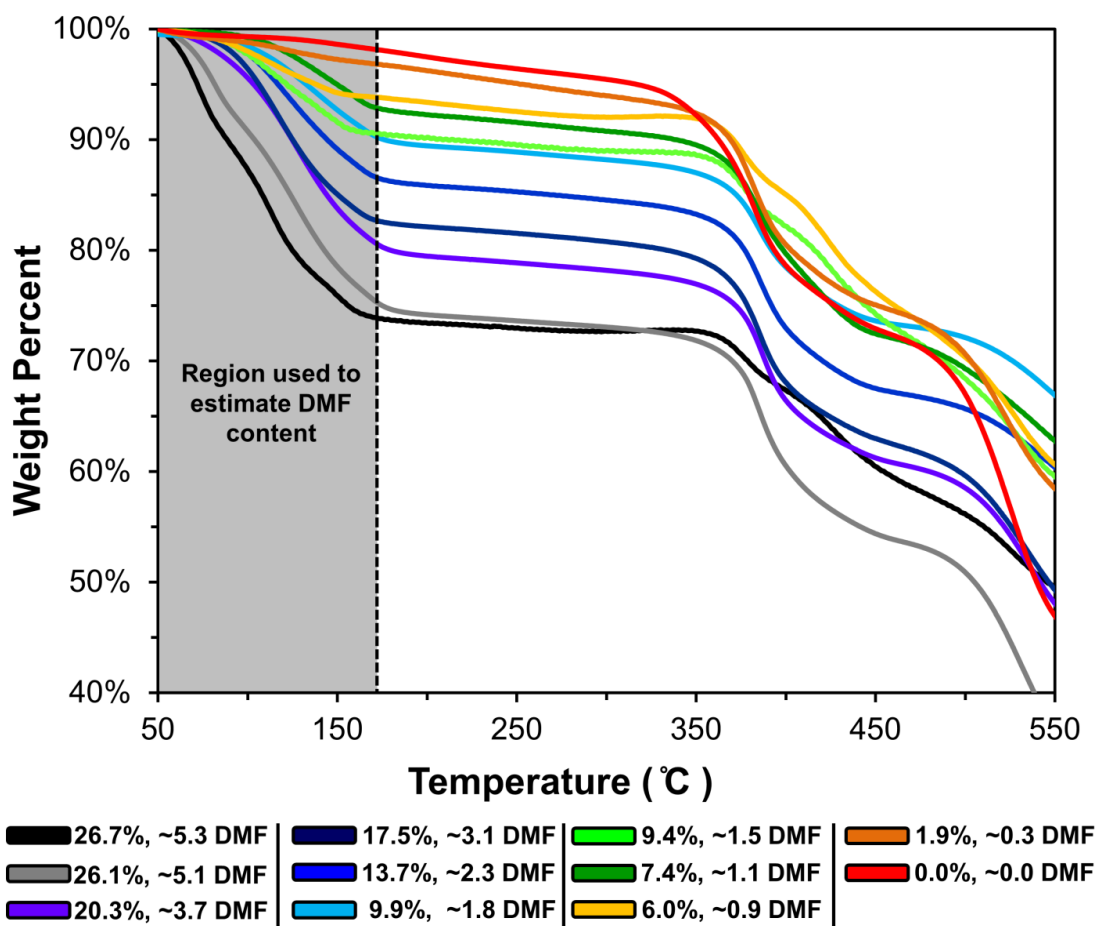


Figure 4.8. TGA profile for samples of **1** at various stages of desolvation. The colored legend at the bottom lists the weight loss in the grey region for each trace, and the corresponding number of calculated DMF molecules per formula unit (including the two coordinated DMF).

bottom of the figure lists the weight of DMF remaining in the sample, which was confirmed by the TG analysis (see TG profile, 50 – 170 °C, Figure 4.8) and the calculated average number of corresponding DMF molecules per formula unit. Changes in the PL excitation and optical absorption spectra were also monitored at various stages and are shown in Figures 4.6 and 4.7.

As shown in Figure 4.5, as DMF evacuates from **1**, incremental PL red-shifting occurs. When the DMF content reaches below ~3.7 DMF molecules per formula unit (Figure 4.5, purple), the high-energy side of the PL emission band undergoes minimal displacement compared to the initial red-shift, and instead, band-broadening is observed through red-shifting of the low-energy side of the band. With an average of ~3.1 DMF (Figure 4.5, navy), **1** appears light-yellow under ambient lighting (Figure 4.5a, center) and has strong greenish PL emission ($\lambda_{\text{max}} = 490 \text{ nm}$), which is still reversible through re-exposure to DMF. The PXRD pattern shows a small lone peak shift from $\sim 8.0^\circ$ to 8.3° . Below ~2.3 DMF (Figures 4.5 and 4.9, blue), two new small peaks in the PXRD pattern are observed at $\sim 4.3^\circ$ and 8.7° signaling the emergence of a new phase (Figure 4.9). At this stage, the emission continues to red-shift mainly through band-broadening, but is no longer entirely reversible presumably due to the new phase being formed. The new PXRD peaks at 4.3° and 8.7° continue to grow in intensity with continued DMF removal, and shift slightly to lower angles. When **1** approaches ~1 DMF, (Figures 4.5 and 4.9, gold) the PXRD peaks corresponding to the original phase are a minor contribution to the pattern, which is dominated by the newly formed phase. The PL band-broadening also stops ~1 DMF per unit cell (Figures 4.5b and 4.7, dark green and gold), at which point the low energy side of the band remains stationary, but the high energy side begins to red-shift again. This trend continues until the estimated DMF content per unit cell is close to zero, at which point **1** is fully activated and now referred to as **1A**. The PL emission of **1A** (Figures 4.5b and 4.7, red trace) has a peak maximum of $\sim 550 \text{ nm}$ and is yellow in color (Figure 4.5c, red circle). The red-shifting trend observed in the PL emission peak of **1** is also observed in the UV-Vis absorption and PL excitation spectra for various stages of

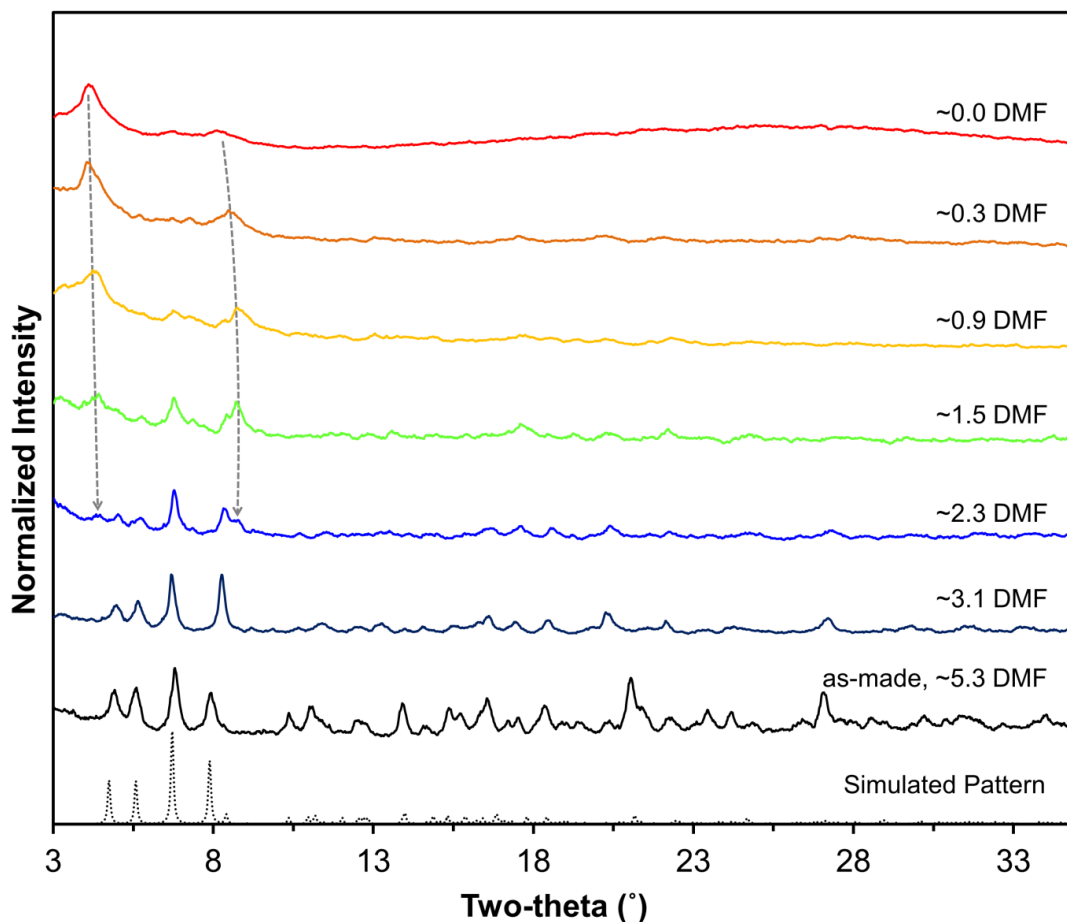


Figure 4.9. PXRD patterns for **1** during various stages of desolvation. The grey arrows mark the appearance and growth of the peaks corresponding to the activated phase.

DMF evacuation (Figures 4.6 and 4.7, top). The irreversible structural changes possibly correspond to departure of coordinated DMF molecules, which play an integral role in linking/stabilizing the two anionic nets through K^+ . As depicted in Figure 4.3, one of the μ_3 -O bridges linking potassium to bismuth is from coordinated DMF; loss of this DMF likely results in destabilization if the 1-D inorganic chain resulting irreversible structural changes.

Following full activation by heating at 90 °C for five days (Figure 4.5, red), the excitation spectra for **1A** (monitored at $\lambda_{em} = 553$ nm) shows a relative maxima plateau across the blue region (400 - 455 nm, Figure 4.10, red dots). The estimated optical bandgap of the activated

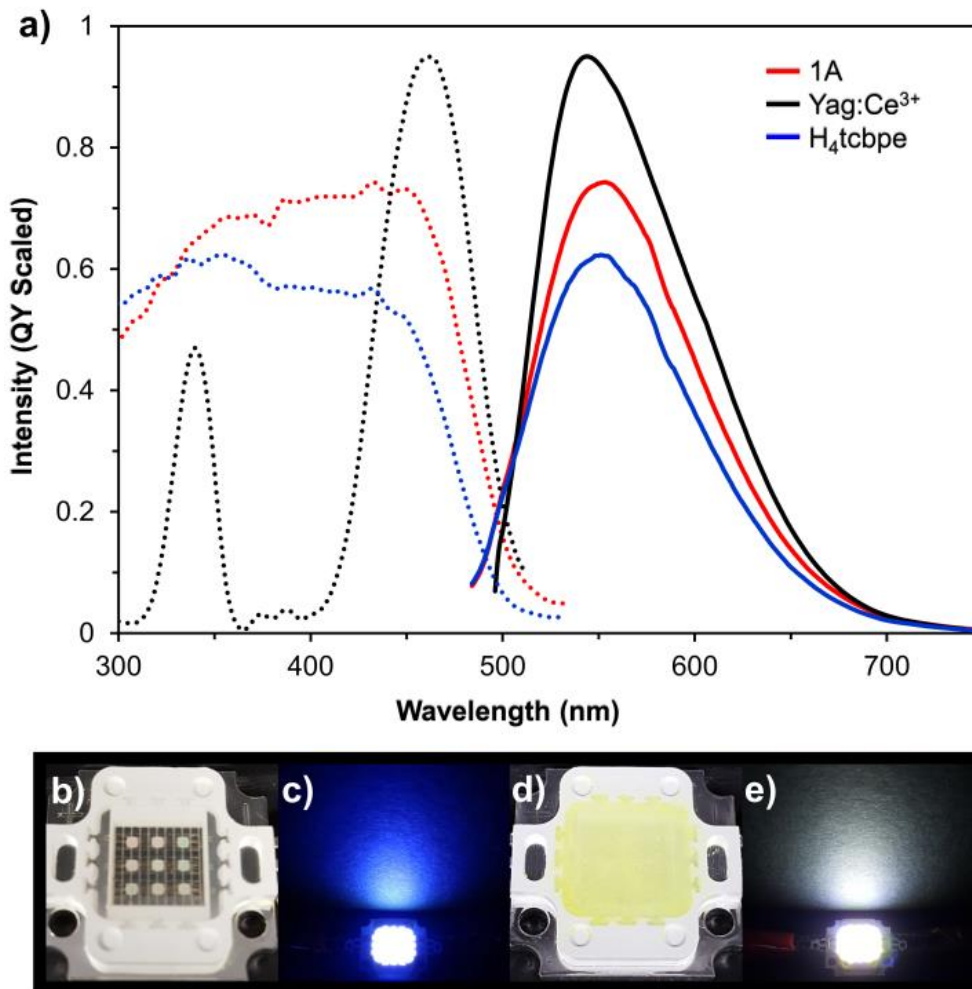


Figure 4.10. a) QY scaled PL excitation (dotted traces) and emission ($\lambda_{\text{ex}} = 455$ nm, solid traces) spectra for **1A** (red), YAG:Ce³⁺ (black) and H₄tcbpe (blue); excitation spectra monitored at 553 nm for **1A**, 543 nm for YAG:Ce³⁺, and 550 nm for H₄tcbpe. b-e) 10W blue LED chip (450-455 nm) uncoated and coated with **1A** under ambient lighting (b,d) and powered on (9V DC) (c, e).

sample is ~ 2.3 eV (Figure 4.6). When excited at 455 nm, **1A** has yellow PL emission ($\lambda_{\text{max}} = 553$ nm, Figure 4.10, solid red curve) with CIE coordinates (0.410, 0.560) (Figure 4.5c), which are comparable to those of YAG:Ce³⁺; CIE coordinates \approx (0.420, 0.560). The emission maximum of **1A** is slightly red-shifted compared to YAG:Ce³⁺, however the band is also slightly broader at the base on the high-energy side, resulting in a slightly cooler emission overall. Notably, while not as high as YAG:Ce³⁺ (QY = 95.0%), when compared to all reported MOF yellow phosphors, **1A** has

the 2nd highest QY of 74.0% (\pm 0.3%, Table 4.1) when excited by blue light (455 nm).⁴⁵ The emission properties of **1A** are similar to that of the pure H₄tcbpe ligand (Figure 3, blue), however with a red-shift in its excitation spectrum, its performance at blue excitation (455 nm) is significantly improved, giving a ~12% increase in QY. The emission profiles for the two are very similar, with **1A** being slightly red-shifted on the high energy side of the emission band. Similarity in their PL profiles suggests that the emission of **1A** is ligand based. A prototype device was fabricated using a 10 W 450-455 nm blue LED to demonstrate the effect of coating with **1A** (Figures 3b - 3e, see Experimental Details 4.2.5 for coating method).

4.4 Conclusion

In summary, a new bismuth-potassium-fluorophore LMOF, [BiK(tcbpe)(DMF)₂] \cdot x DMF, was obtained using carefully considered synthetic conditions, and its structural and optical properties were studied. The new material was found to have highly sensitive solvochromic optical properties with respect to guest DMF solvent. The as-made LMOF has strong blue emission with a QY of ~57% that undergoes significant optical red-shifting upon incremental removal of DMF. Upon loss of structurally critical DMF molecules, irreversible structural changes occur paired with additional optical red-shifting. The fully activated material has strong yellow emission (QY ~74%) when excited by 455 nm blue light, making it a promising candidate as an alternative blue-excitable yellow phosphor totally free of REEs.

CHAPTER 5. Structural Versatility and Electrocatalytic Activity of an Anionic Bi-porphyrin Metal-Organic Framework

Manuscript in preparation.

5.1 Introduction

Human activity is anomalously increasing average global temperatures through the release of greenhouse gases, such as CO₂, CH₄, and NO_x. CO₂ is currently the primary concern as it is the byproduct of all fossil fuel combustion reactions, which make up approximately 80% of global energy-generating technologies.⁸ While CO₂ capture and sequestration from post-combustion effluents is one approach, converting CO₂ into value-added carbon products is more desirable than simply storing it as a waste product. Because this conversion requires significant energy input, the utilization of solar energy is a key element of developing an efficient and sustainable conversion process. This can be achieved either directly with a photocatalyst or indirectly as electrical energy obtained from solar sources with an appropriate electrocatalyst.²¹⁴⁻

²¹⁵ Recent reports have demonstrated that bismuth may have a future role to play in this conversion process as a catalyst capable of selective conversion to carbon monoxide or formic acid, both of which can act as precursors in various chemical processes.²¹⁶⁻²¹⁷ While the reported catalysts are heterogeneous in nature, the exact nature of the catalyst is obscured by lack of well-defined crystal structures. Additionally, one of the most significant drawbacks of traditional heterogeneous catalysts (metals, metal-oxides) is that reactions are limited to surface, as their densely packed nature bars guest entry to the bulk material. Known for both crystallinity and porosity, theoretically metal-organic frameworks (MOFs) can be ideal for catalytic studies.²¹⁸ MOFs can be viewed as metal-oxide nanoparticles that are spatially fixed in a porous matrix, potentially providing substrate access to a larger number of active sites and thereby improving overall atomic efficiency when compared to their metal-oxide analogues. With this in mind, we

sought to study the whether the activity of Bi can be maintained when incorporated into a metal-organic framework (MOF) structure.

Despite over 30,000 existing literature entries containing the topic metal-organic framework, MOFs based on Bi^{3+} are still scarce; a cursory search on SciFinder produces less than 15 reported structures containing a bismuth primary or secondary building unit (PBU or SBU, respectively).^{195, 197-198, 200-203, 205-209, 211, 219-220} Difficulty obtaining pure phase single crystals and the tendency to form densely packed one- and two-dimensional networks due to hemidirected coordination geometry has likely served to stunt the growth of this research area. Bi^{3+} ions contain a stereoactive lone-pair of $6s^2$ valence electrons that occupy a significant portion of the atomic surface, thereby preventing formation of highly symmetrical coordination geometries typical of most transition metals. Lack of predictable coordination geometry or well-established SBU formation further complicates Bi MOF design. When reacted with carboxylic acids, Bi^{3+} PBUs will accommodate up to four coordinating carboxylates, thereby producing a system with overall -1 net negative charge, requiring the presence of charge balancing cations. To date, only four permanently porous Bi-MOFs have been reported.²²¹

Porphyrin derivatives are the focus of an immense amount of research spanning multiple disciplines.²²² These systems are characterized by a tetrapyrrolic macrocycle core having four Lewis basic nitrogen atoms, two of which contain acidic protons. This core is highly conjugated, giving rise to unique UV-Vis and photoluminescent properties; perturbation of this π system results in significant changes to the optical signals.⁴⁸ Additionally, the core's nitrogen Lewis basic sites provide convenient functionality for interactions with guest molecules, and as such, these materials are often exploited for applications in bio-imaging, molecular recognition, and sensing.⁴⁹ The macrocyclic core is capable of housing a guest metal atom via chelation from the N sites. After deprotonation, the core adopts a 2- state, making a natural system to pair with 2+ and 3+ transition metals (in the case of 3+ metals, anions act as charge balancing species). This

chelation is equatorial with respect to the guest metal atoms, leaving coordinatively unsaturated axial positions which are often used as open-metal sites (OMSs) in catalysis chemistry. Of particular interest to us are the reports of catalytic CO₂ reduction on metalloporphyrins. The Co²⁺ and Fe³⁺ variants were reported as CO₂ reduction photocatalysts in the 1970's, and numerous reports since then have confirmed the catalytic production of carbon monoxide and formic acid at these metal centers.²²³ More recently, MOFs incorporating carboxylate porphyrin derivatives as linkers have also shown activity for CO₂ reduction. Two pathways exist for porphyrin utilization in MOF catalysts. Because these molecules absorb visible light over a wide range of the visible spectrum, the metal-free porphyrin derivatives can be used to photosensitize MOF metal building units for use as visible-light photocatalysts, as demonstrated by Xu and coworkers.⁴² Alternatively, the ligand can be incorporated into MOF structures in its metallated form, providing metal centers with pre-established OMSs having catalytic activity. Multiple groups have utilized this method for both electrocatalytic and photocatalytic CO₂ reduction studies.³⁸⁻⁴¹

Our previous study established that pure-phase single crystals of Bi³⁺ MOFs are obtainable by synthetically employing competing monocarboxylic acids (acid modulators) paired with judicious selection of reaction conditions.³⁵ Additionally, our results implied that integration of large polytopic linkers with more than two points of extension may promote the formation of permanently porous bismuth frameworks. With this in mind, we have prepared a new permanently porous Bi MOF, [(CH₃)₂NH₂][Bi(tcpp)(H₂O)]·*n*DMF (DMA⁺-Bi-tcpp), by utilizing the large meso-Tetra(4-carboxyphenyl)porphyrin (H₆tcpp) ligand. This material has coordinatively unsaturated sites on the Bi³⁺ PBU and forms an anionic framework that is charge balanced by dimethylammonium cations (DMA⁺) that are formed in-situ. Furthermore, DMA⁺ can be post-synthetically exchanged for Li⁺ cations (Li@Bi-tcpp). This exchange results in improved thermal stability and structural changes that were characterized by single-crystal X-ray diffraction on single crystal samples of Li[Bi(tcpp-M)(DMF)]·*n*DMF (Li-Bi-tcpp) that were

prepared by synthesizing the MOF with Li^+ present in the reaction. It was found that the structural changes that occur after cation exchange correspond to a reduced catenation state from 3-fold to 2-fold and repositioning/rearrangement of the carboxylate-Bi coordination bonds, demonstrating a rare example of metal-based framework flexibility. The new MOF can also material can be prepared with metalloporphyrins (Cu^{2+} , Co^{2+} , Ni^{2+} , Fe^{3+} , Mn^{3+}), providing an additional avenue for catalytic CO_2 reduction studies and resulting in a tri-metallic framework. Preliminary electrocatalytic results suggest that the Bi^{3+} does not have activity for CO_2 reduction, but that activity can be imbued by utilizing the Fe^{3+} metallated linker (Li-Bi-tcpp-Fe).

5.2 Experimental Details

Unless otherwise stated, all starting chemicals used in this study were reagent grade (>97%) and purchased from commercial sources. Benzoic acid used in MOF synthesis was recrystallized in a 1:1 mixture of ethanol (EtOH) and deionized (DI) water.

5.2.1 Ligand Synthesis

The metal-free Tetrakis(4-carboxyphenyl)porphyrin (H_6tcpp) ligand was purchased from TCI Chemicals. All metallated ($\text{H}_4\text{tcpp-M}$) variants were prepared used the general procedure described below, which was adopted from literature.¹⁶⁷

Synthesis of the porphyrin ester: 5,10,15,20-Tetrakis(4-methoxycarbonylphenyl)porphyrin (TPPCOOMe)

Pyrrole (3.0 mL, 0.043 mol) and methy p-formylbenzoate (6.9 g, 0.042 mol) were refluxed in 100 mL of propionic acid in a 500-mL round bottom flask for 12 hr. The reaction was protected from ambient light using aluminium foil. After cooling to room temperature, the mixture was filtered, washed with cold methanol and THF and dried under dynamic vacuum. The average yield of the purple product over multiple reactions was ~2.0 g (~ 22%).

Metallation of the porphyrin ester: 5,10,15,20-Tetrakis(4-methoxycarbonylphenyl)porphyrin-M (TPPCOOMe-M)

As a general procedure, a solution of TPPCOOMe (1.00 g, 1.17 mmol) and corresponding metal salt (~ 13.0 mmol of either: $\text{CuCl}_2 \cdot 2\text{H}_2\text{O}$, $\text{NiCl}_2 \cdot 6\text{H}_2\text{O}$, $\text{CoCl}_2 \cdot 6\text{H}_2\text{O}$, $\text{MnCl}_2 \cdot 4\text{H}_2\text{O}$, $\text{FeCl}_2 \cdot 4\text{H}_2\text{O}$) was heated to 150 °C in 100 mL of DMF for 6+ hours while protected from ambient light by foil. Water was added in excess (> 150 mL) to precipitate the dissolved product after cooling the mixture to room temperature, filtered, and washed with additional water. The product was then dissolved in CHCl_3 and washed three times with 1 M HCl (only in the case of Fe and Ni) and three times with H_2O (all samples). The organic layer was collected and dried over magnesium sulfate overnight, followed by filtration to remove the drying agent. Finally the dissolved product was dried using rotary evaporation to afford quantitative yields of TPPCOOMe-M.

Base hydrolysis and acidification of the porphyrin ester to form: meso-Tetra(4-carboxyphenyl)porphyrin-M (H_4tcpp -M)

~1.0 g of TPPCOOMe-M was dissolved and heated to 90 °C in a 1:1 mixture of THF and MeOH (~70 mL total volume). 35 mL of KOH solution (~ 3.0 M) was then added and the mixture was allowed to reflux overnight (12 hr+). The reaction was cooled to room temperature and rotary evaporated to remove the organic solvents. In the event of precipitation, additional water was added with heat, if necessary, to fully dissolve the product. The solution was then acidified and precipitated by adding it dropwise to 6 M HCl (we specifically add the product to acid to prevent any formation of the potassium salt form of the ligand). Finally, the precipitate was filtered, washed with water until pH neutral, and then dried at 90 °C under dynamic vacuum.

5.2.2 MOF Synthesis

DMA^+ -Bi- $tcpp$ and DMA^+ -Bi- $tcpp$ -M

Single crystals of DMA⁺-Bi-tcpp ($[(\text{CH}_3)_2\text{NH}_2][\text{Bi}(\text{tcpp})(\text{H}_2\text{O})]\cdot 3\text{DMF}$) suitable for diffraction studies were obtained solvothermally. BiPh₃ (8.7 mg, 0.02 mmol), H₆tcpp (or H₄tcpp-M) (21.0 mg, 0.026 mmol; 25.0 mg in the case of H₄tcpp-M), and benzoic acid (0.6 g, 4.9 mmol) were ultrasonically dissolved in 4 mL of DMF in a 20 mL scintillation vial. The reaction mixture was heated to 100 °C for 3d+ to afford large purple single crystals. The products were washed by decanting the mother liquor and washing with fresh DMF until the solution was completely transparent. Occasionally, a fine black impurity will accompany product formation but can easily be removed using ultrasonication to generate a suspension of the impurity, followed by decanting. Changing the acid modulator and reaction temperature to acetic acid at 90 °C for 7d resulted in very large 3 mm crystals in the case of the non-metallated ligand. This method did not work for the metallated variants. The typical product yield based on Bi is between 70-80%. Decreasing the quantity of benzoic acid can slightly improve yields, and also results in decreased crystal sizes. If no benzoic acid is used, only amorphous product is obtained.

DMA⁺-Bi-tcpp cation exchange with LiClO₄·3H₂O (Li@Bi-tcpp)

Crystalline samples of DMA⁺-Bi-tcpp (15 mg) were immersed in 10 mL of MeCN containing 100 mg of dissolved LiClO₄·3H₂O. The mixture was allowed to sit for 3 days, and the MOF was isolated and washed with fresh MeCN for PXRD and TGA measurements after 1 and 3 days of exchange time.

Li-Bi-tcpp and Li-Bi-tcpp-M

Single crystals of Li-Bi-tcpp ($\text{Li}[\text{Bi}(\text{tcpp-M})(\text{DMF})]\cdot n\text{DMF}$) and Li-Bi-tcpp-M suitable for diffraction studies were obtained in a similar manner as the DMA⁺ variant. BiPh₃ (8.7 mg, 0.02 mmol), H₆tcpp (or H₄tcpp-M) (21.0 mg, 0.026 mmol; 25.0 mg in the case of H₄tcpp-M), LiClO₄·3H₂O (160 mg, 0.1 mmol) and benzoic acid (0.6 g, 4.9 mmol) were ultrasonically dissolved in 4 mL of DMF in a 20 mL scintillation vial. The reaction mixture was heated to 100

°C for 3d+ to afford large reddish-purple single crystals. The products were washed by decanting the mother liquor and washing with fresh DMF until the solution was completely transparent.

5.2.3 Instrumental Details

Single Crystal X-ray Diffraction (SXRD) and Powder X-ray Diffraction (PXRD)

Single crystal diffraction data was collected at 100 K on a Bruker APEXII CCD diffractometer using the synchrotron source ($\lambda = 0.77490 \text{ \AA}$) at the Advanced Light Source 11.3.1 Chemical Crystallography beamline. The refinement method used was full-matrix least-squares on F^2 . PXRD patterns were recorded on a Rigaku Ultima IV X-ray diffractometer with Cu $K\alpha$ radiation ($\lambda = 1.5406 \text{ \AA}$). A graphite monochromator was used and the generator power settings were set to 40 kV and 44 mA. Data were collected between $2-35^\circ 2\theta$ with a step size of 0.02° and a scan speed of 1.5 deg/min .

Thermogravimetric Analysis (TGA)

Measurements were performed using a TA Q5000 Thermogravimetric Analyzer with a temperature ramp of 10°C/min from room temperature to 600°C under nitrogen gas flow (20 mL/min).

Ultraviolet-visible (UV-Vis) Spectroscopy

The optical absorption spectra of solid samples were collected on a Shimadzu UV-3600 spectrophotometer at room temperature. The baseline was taken on a BaSO_4 standard. Samples were prepared on a quartz sample holder and diffuse reflectance measurements were converted to absorption using the Kubelka-Munk Function.

N₂ sorption measurements

BET surface area measurements were made by N_2 gas adsorption at 77K on a volumetric gas sorption analyzer (Autosorb-1 MP, Quantachrome Instruments). $\sim 100 \text{ mg}$ of sample was

prepared by solvent exchanging the MOFs with MeCN, followed by outgassing under vacuum at 80 °C overnight.

Electrochemical Measurements

All electrochemical measurements were performed on a Princeton Applied Research (PAR) VersaSTAT 3 potentiostat/galvanostat using the Versastudio software under ambient conditions. Depending upon the trial, 0.1 M of either tetrabutylammonium hexafluorophosphate (TBAPF₆) or anhydrous LiClO₄ in MeCN (HPLC grade) were used as supporting electrolyte. The TBAPF₆ was twice recrystallized using EtOH prior to use. LiClO₄ was electrochemically purified at an applied potential of -2.0V vs. Ag/AgCl for 12 hours using a stainless steel working electrode and a platinum counter electrode. **Photocurrent measurements:** DMA⁺-Bi-tcpp was ground and applied to an ITO electrode with a working area of 0.24 cm². The working electrode was immersed into one side of a two-compartment H-cell with an Ag/AgCl quasi reference, and a Pt counter electrode was used in the other compartment, which was separated by a glass frit. 0.5 M TBAPF₆ was used as supporting electrolyte. Chronoamperometric measurements were then performed at open-circuit, and chopped WLED light was used to measure the photocurrent response at 30 sec intervals. **Cyclic Voltammetry (CV) measurements:** a standard two-compartment H-cell separated by a glass frit, with a total volume of 31.9 mL was used for all CV measurements. A glassy carbon electrode (GCE, CHI instruments) with a working area of ~0.071 cm² was used as the working electrode. The MOF samples were applied by spreading finely ground sample onto the GCE surface. Nafion suspensions were attempted for MOF application to the electrode, but failed to adhere well when immersed in organic electrolyte. Platinum wire was used as the counter electrode, and an Ag/AgCl quasi reference isolated in a vycor-tipped compartment was used as the reference electrode. The reference and working electrodes were contained in the same H-cell compartment with the Pt wire isolated in the adjacent one. Auxillary measurements were also performed using a graphite counter electrode, which produced the same

results at the Pt counter. Unless stated otherwise, data was collected at a scan rate of 0.01 V/s.

Chronoamperometric measurements (bulk electrolysis, BE): a custom made 5-port electrochemical cell was used for bulk electrolysis, with 0.1 M LiClO_4 as a supporting electrolyte and trifluoroethanol (TFE) as a proton source. Toray (120, 5% wet proofed) carbon paper working electrodes were fabricated (Figure 5.1) and the MOF was applied by drop-casting catalyst suspensions (10 mg in 250 μL of MeCN). Multiple applications were made with drying in between each application to ensure even coverage of the electrode. Some trials were performed using added VXC72R conductive carbon (Cabot) to improve charge percolation to active sites. In these cases, 9 mg of MOF was ground together with 1 mg of VXC72R and suspended in 250 μL of MeCN. ImageJ software was used to estimate the geometric surface area of the working electrode. A Pt counter electrode was used, but was isolated from the main reaction compartment using an isolation tube capped with an ultrafine

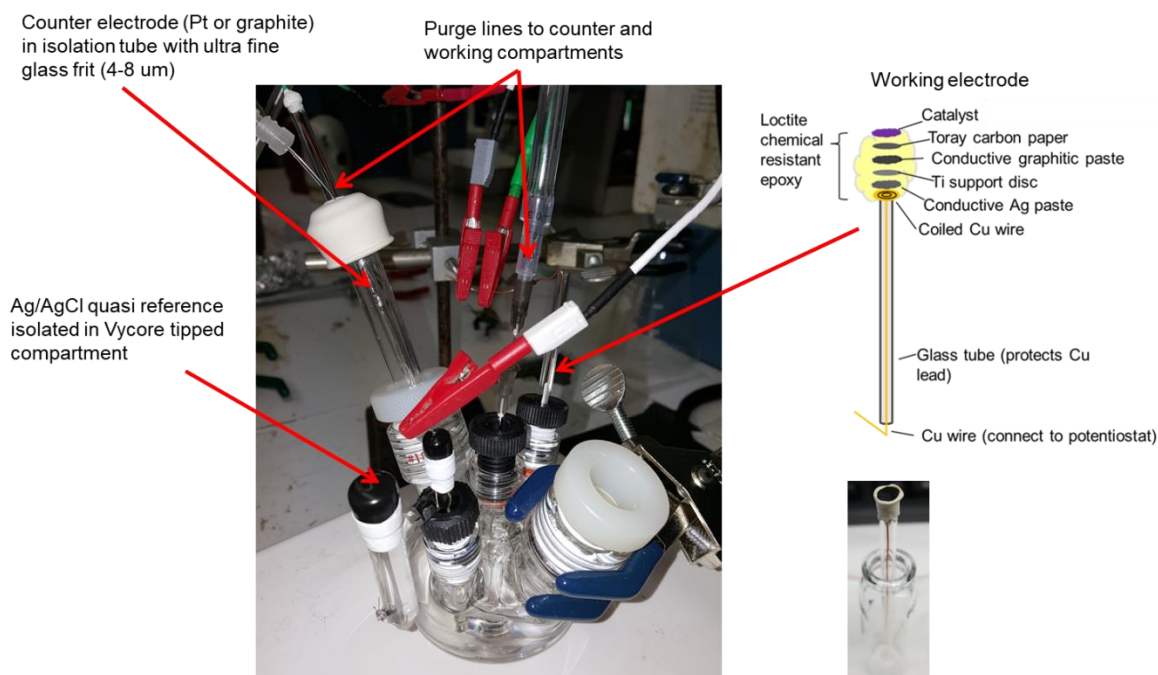


Figure 5.1. Photograph of the custom-made electrochemical cell and a schematic illustration of the Toray working electrodes used for BE measurements.

glass frit (4-8 μm pores). An Ag/AgCl quasi reference isolated in a vycor-tipped compartment was used as the reference electrode. The main compartment and isolation tube were sparged with either N_2 or CO_2 for 30 mins and the system was confirmed to be air free prior to beginning the measurement by GC headspace analysis. After a set duration (typically 2 hours), products were tested by GC headspace analysis.

Gas Chromatography

Headspace product analysis was performed using Agilent 6890N gas chromatograph (GC) with TCD and FID detectors connected in series with a 30 m, 0.53 mm ID, 50 μm Rt-MSieve 5A capillary column, which allows for simultaneous analysis of H_2 , CO, O_2 , N_2 and hydrocarbon gasses up to 3 carbons in length. Two temperature ramps were used (the first to 250 $^\circ\text{C}$, the second to 300 $^\circ\text{C}$) with a total run time of 35 min. The system was calibrated using calibration gas (ShopCross.com) containing 100 ppm each of H_2 , CO, CH_4 , C_2H_2 , C_2H_4 , C_2H_6 , 400 ppm CO_2 , 2500 ppm O_2 , 17000 ppm N_2 , and Ar as the balance. Over multiple repeated 100 μL injections, a 5% error was established, which is ascribed to human sampling error. A representative chromatogram is shown in figure 5.2.

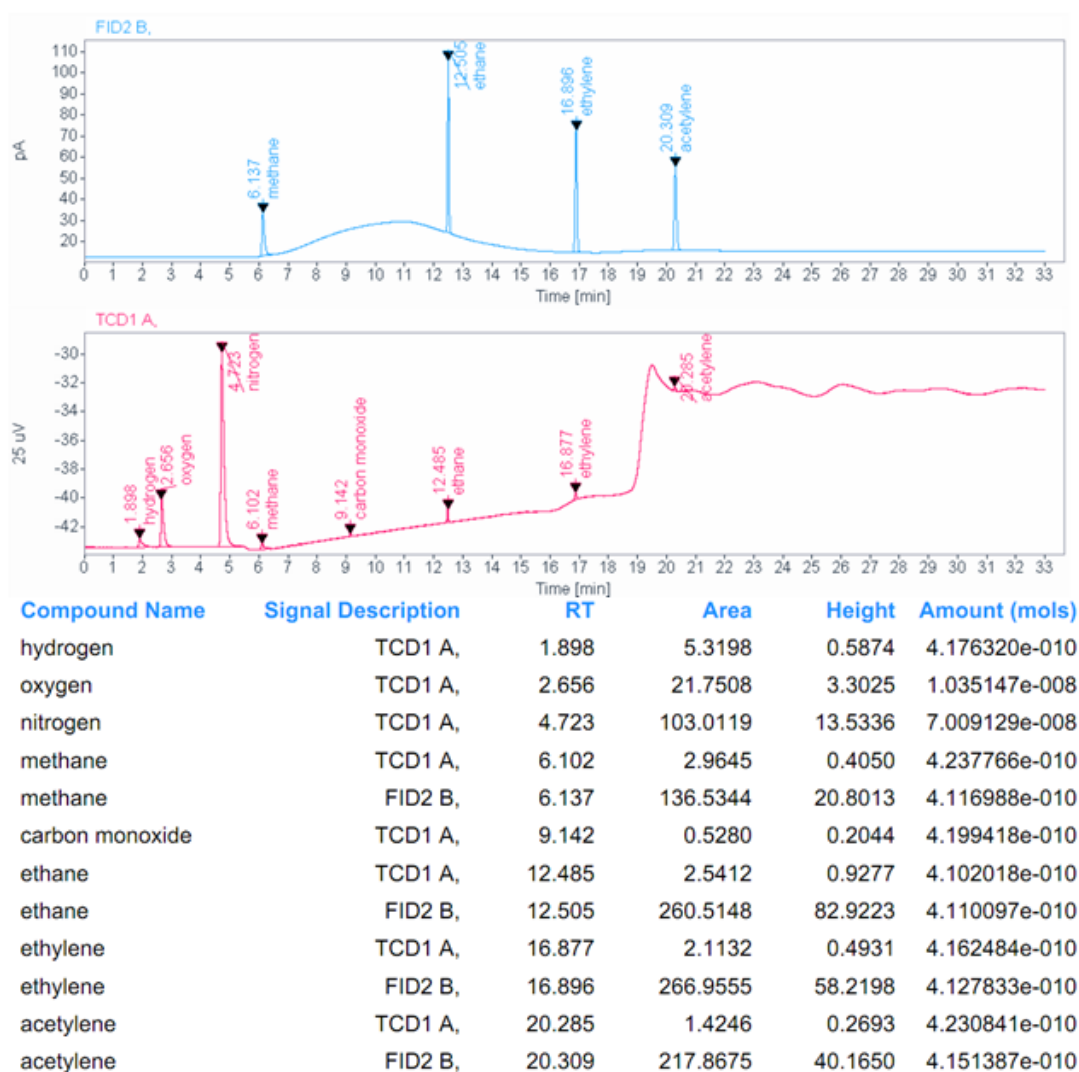


Figure 5.2. Representative chromatogram and analysis results of the calibration gas.

5.3 Results and Discussion

Single crystals of $\text{DMA}^+\text{-Bi-tcpp}$ and $\text{DMA}^+\text{-Bi-tcpp-M}$ ($\text{M} = \text{Cu}^{2+}$, Co^{2+} , Ni^{2+} , Fe^{3+} , Mn^{3+}) were obtained solvothermally in DMF (100 °C, 3+ days) with excess benzoic acid added as a synthetic modulating agent (see Experimental Details for synthetic conditions) (Figure 5.3). A Bisalicylate cluster described previously was originally used as the metal source, but was found to be unnecessary and instead, BiPh_3 was used directly. However, attempts using tradition Bi salts ($\text{Bi}(\text{NO}_3)_3$, BiI_3) failed, as impure products were obtained. $\text{DMA}^+\text{-Bi-tcpp}$ crystallizes in a

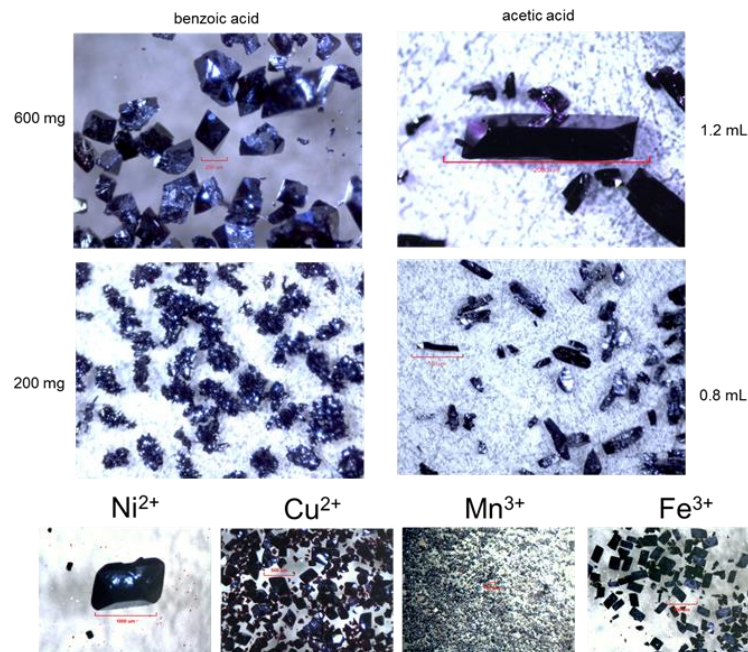


Figure 5.3. Optical micrographs of $\text{DMA}^+\text{-Bi-tcpp}$ crystals.

Structural Formula: $[\text{Bi}(\text{tcp})](\text{H}_2\text{O})[(\text{CH}_3)_2\text{NH}_2]\cdot 3\text{DMF}$

Crystal System: monoclinic

Space Group: C2/c

Unit Cell:

$a = 8.1544(6) \text{ \AA}$

$b = 21.7581(16) \text{ \AA}$

$c = 31.409(2) \text{ \AA}$

$\alpha = 90^\circ$

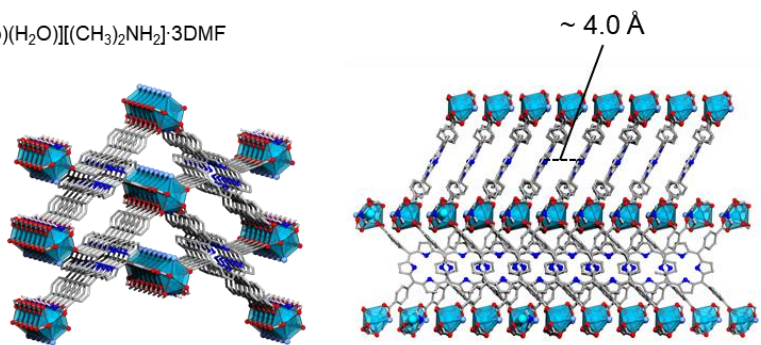
$\beta = 95.3910(10)^\circ$

$\gamma = 90^\circ$

$V = 5548.0(7) \text{ \AA}^3$

$Z = 4$

3-fold interpenetration



Structural Formula: $[\text{Li}[\text{Bi}(\text{tcp})\text{-M}](\text{DMF})]\cdot n\text{DMF}$

Crystal System: monoclinic

Space Group: C2/c

Unit Cell:

$a = 30.3090(13) \text{ \AA}$

$b = 16.1796(7) \text{ \AA}$

$c = 30.2549(13) \text{ \AA}$

$\alpha = 90^\circ$

$\beta = 105.045(2)(10)^\circ$

$\gamma = 90^\circ$

$V = 14328.1(11) \text{ \AA}^3$

$Z = 8$

2-fold interpenetration

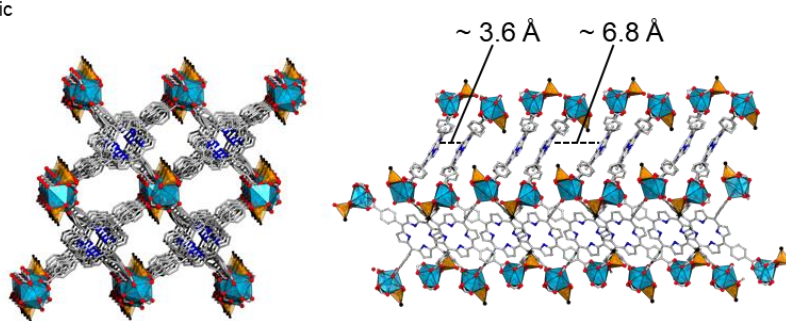


Figure 5.4. Structure plots and unit cell information for $\text{DMA}^+\text{-Bi-tcpp}$ and Li-Bi-tcpp .

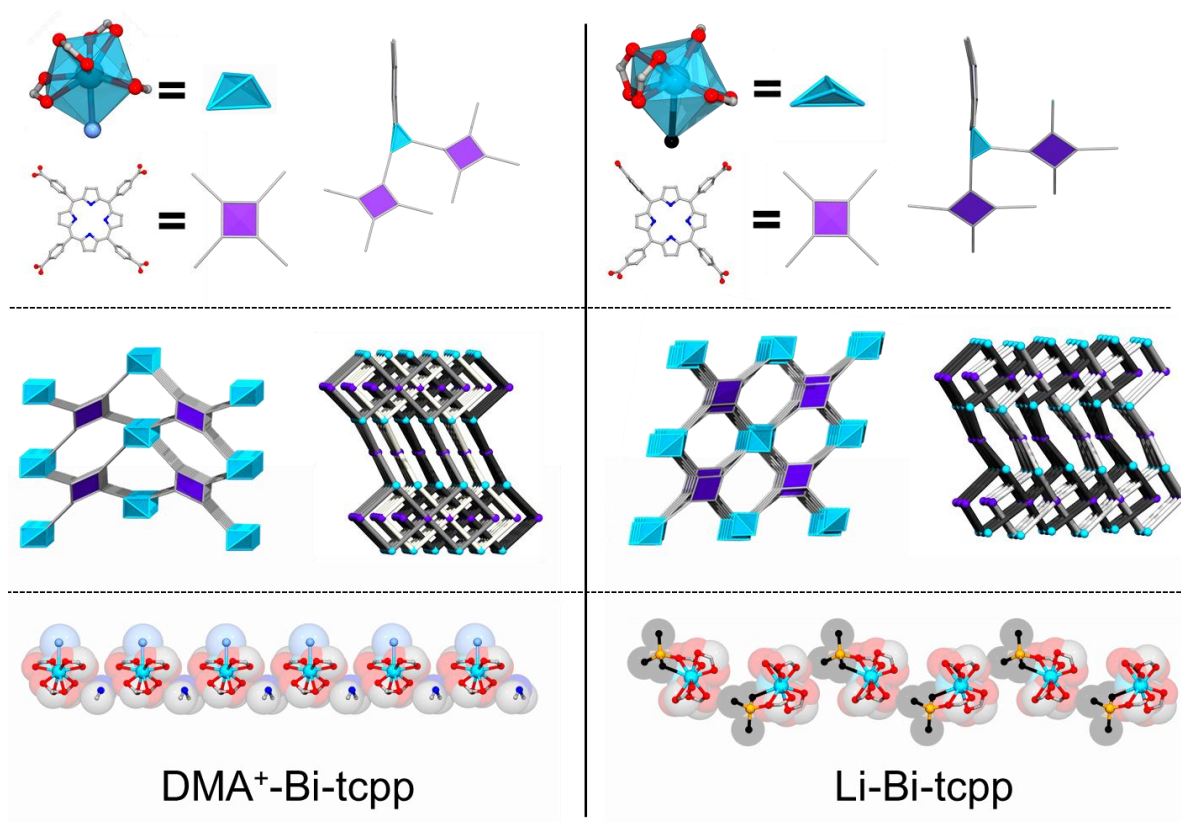


Figure 5.5. Polyhedral net, line drawings, and PBU 'chains' of DMA⁺-Bi-tcpp and Li-Bi-tcpp.

Table 5.1. Crystal data and structure refinement for DMA⁺-Bi-tcpp.

Identification code	DMA ⁺ -Bi-tcpp	
Empirical formula	C ₅₉ H ₅₅ Bi N ₈ O ₁₂	
Formula weight	1277.09	
Temperature	100(2) K	
Wavelength	0.71073 Å	
Crystal system	Monoclinic	
Space group	C2/c	
Unit cell dimensions	a = 8.1544(6) Å	a = 90°.
	b = 21.7581(16) Å	b = 95.3910(10)°.
	c = 31.409(2) Å	g = 90°.
Volume	5548.0(7) Å ³	
Z	4	
Density (calculated)	1.529 Mg/m ³	
Absorption coefficient	3.249 mm ⁻¹	
F(000)	2576	
Crystal size	0.17 x 0.08 x 0.05 mm ³	
Theta range for data collection	1.302 to 29.107°.	
Index ranges	-11 ≤ h ≤ 11, -29 ≤ k ≤ 29, -42 ≤ l ≤ 42	
Reflections collected	30207	
Independent reflections	7451 [R(int) = 0.0998]	
Completeness to theta = 25.242°	100.0 %	
Absorption correction	Semi-empirical from equivalents	
Max. and min. transmission	0.7461 and 0.5984	
Refinement method	Full-matrix least-squares on F ²	
Data / restraints / parameters	7451 / 329 / 440	
Goodness-of-fit on F ²	1.169	
Final R indices [I > 2σ(I)]	R1 = 0.0661, wR2 = 0.1495	
R indices (all data)	R1 = 0.0786, wR2 = 0.1543	
Extinction coefficient	n/a	
Largest diff. peak and hole	2.680 and -4.471 e.Å ⁻³	

monoclinic crystal system with a C2/c space group (Figure 5.4, Table 5.1); the asymmetric unit has one dimethyl ammonium cation, Bi^{3+} , tcpp and one coordinated water. The Bi^{3+} building unit is overall coordinated to nine oxygen atoms with hemidirectional coordination geometry owing to bismuth's lone pair of $6s^2$ electrons (Figure 5.5). Four carboxylates from four tcpp linkers form bidentate coordination bonds to Bi^{3+} , with the last oxygen from coordinated water. The overall structure has 3-fold interpenetration and can be described as three interpenetrated 4,4-connected anionic 3-D nets comprised of distorted tetrahedral Bi^{3+} and rectangular tcpp building units. The nets perfectly align, forming straight rows of Bi^{3+} PBUs with respect to the crystallographic *a*-axis. The Bi^{3+} building unit has highly distorted hemidirected tetrahedral geometry with respect to linker connectivity, as observed in our previous work. Two planes are formed by two each of the four linkers which extend throughout each net. DMA^+ cations are tightly packed between each PBU to balance the negative charge. Each pair of carboxylate oxygen atoms share one shorter and one longer coordination bond with Bi, as observed in similar materials. The longest coordination bond is from the coordinated water's O atom (light blue ball), at a distance of 2.781 Å. The two closest carboxylates to the coordinated water share the same bond lengths with each other, but have slightly longer bond lengths (~ 1 Å) than the pair of carboxylates opposite of the coordinated water. The longer Bi-O bond lengths for the closer two carboxylates are 2.497 and 2.560 Å, while the other pair of carboxylates have Bi-O distances of 2.383 and 2.455 Å.

$\text{DMA}^+\text{-Bi-tcpp}$ is stable in a wide variety of organic solvents, but does not seem to survive water treatment, as the PXRD pattern of recovered sample is severely altered, with only a few low-angle peaks present after immersion (Figure 5.6). TGA measurements on the as-made material show about 20% weight loss from synthesis solvent. After solvent exchange with numerous solvents, different weight losses are obtained, demonstrating the porous nature of the material (Figure 5.7). Additionally, after exchanging with MeOH followed by outgassing at room temperature under vacuum, the TGA profile shows two characteristic weight losses (Figure 5.8). The first is a $\sim 1.8\%$ weight loss, which is ascribed to the terminally coordinated water molecules

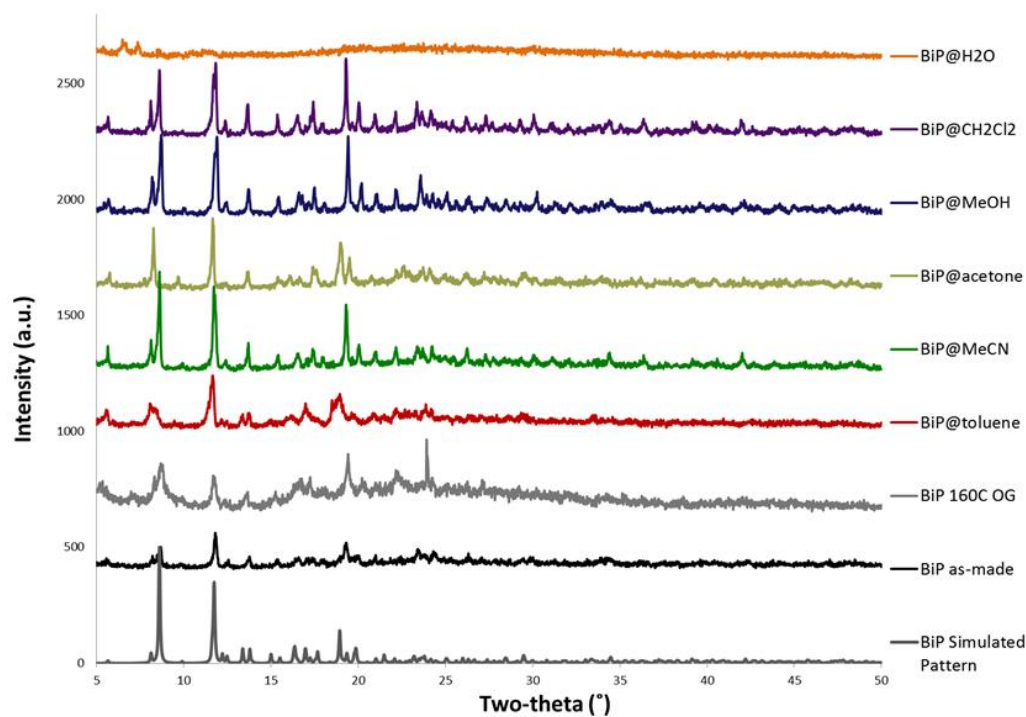


Figure 5.6. Simulated, as-made, directly outgassed, and solvent exchanged PXRD patterns for $\text{DMA}^+\text{-Bi-tcpp}$.

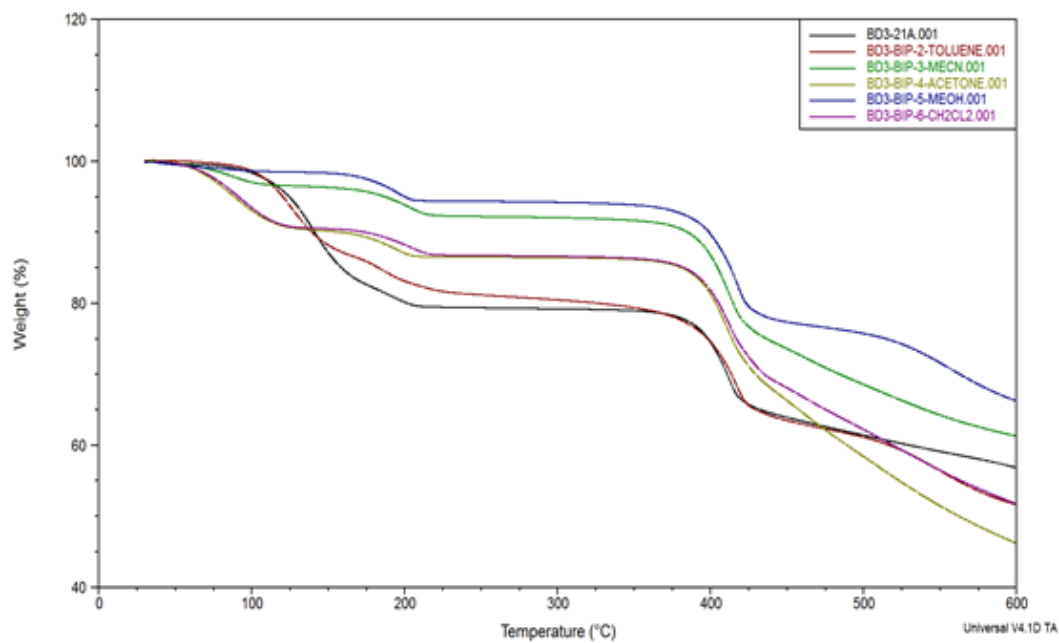


Figure 5.7. TGA profile for $\text{DMA}^+\text{-Bi-tcpp}$ as-made (black) and solvent exchanges samples.

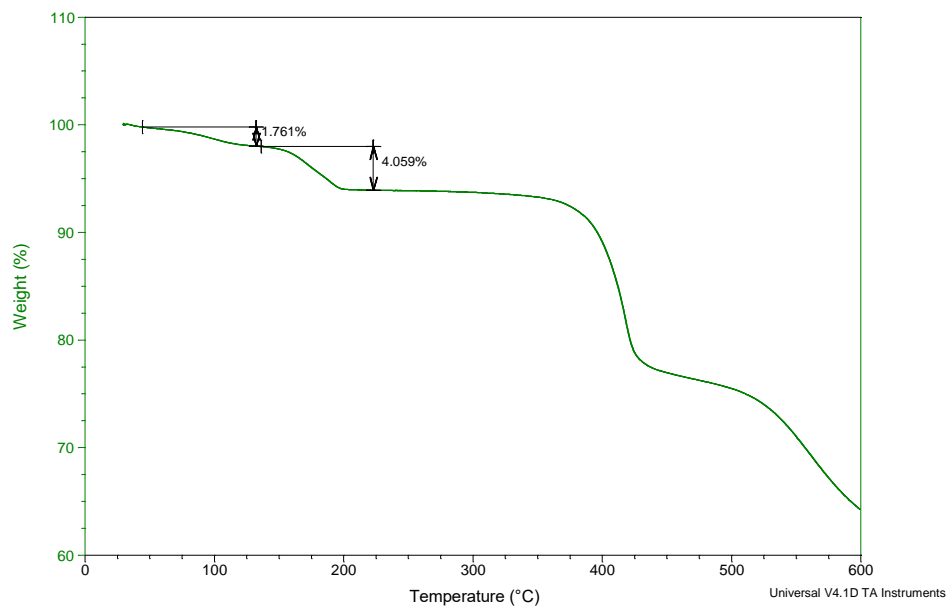


Figure 5.8. TGA profile of MeOH exchanged DMA⁺-Bi-tcpp after applying dynamic vacuum at room temperature overnight.

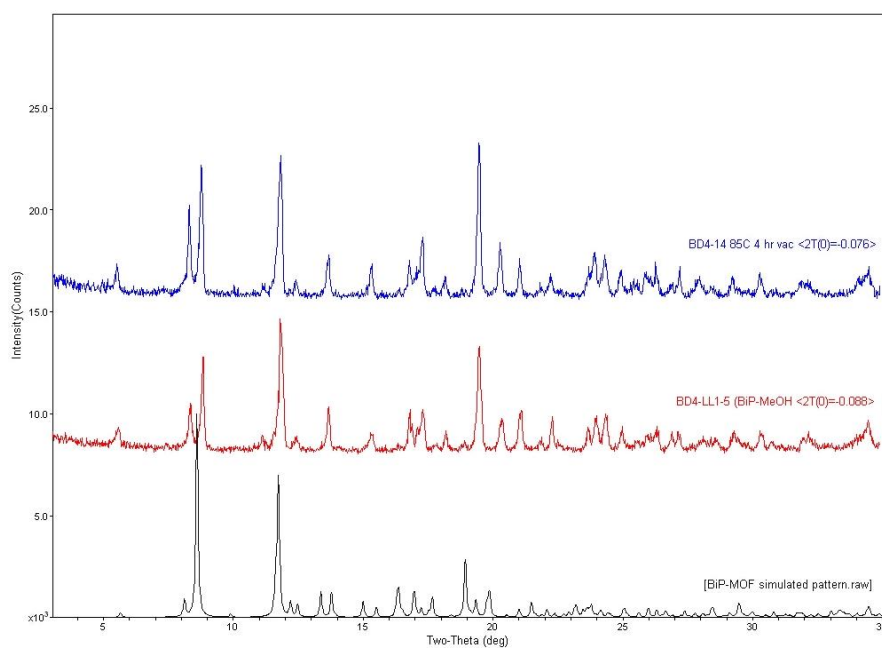


Figure 5.9. PXRD patterns for DMA⁺-Bi-tcpp (black = simulated pattern) after MeOH exchange followed by outgassing under dynamic vacuum at room temperature (red) and after heating at 85 °C for 4 hours (blue).

and occurs at about 85 °C, while the second is a ~4.1% weight loss and occurs at about 160°C, corresponding to the loss of DMA⁺. Both of these weight losses correlate strongly with the theoretic values. PXRD measurements show complete retention of the structure after the removal of coordinated water (Figure 5.9), but loss of crystallinity is observed after heating at 160°C overnight. Based on the crystal structure, there appear to be small 1-D channels of about 4 Å residing above the PBU rows (measured from the outer surface of the Van der Waals radius of the coordinated water O), which is where the terminal water molecules are located. This suggests the presence of Bi³⁺ OMSs that are accessible from the small 1-D channel. However, attempts to characterize the BET surface area and pore size distribution of this material using N₂ sorption experiments ultimately failed. While the activated MOF does uptake N₂, it never reaches equilibrium.

Rows of diagonally stacked porphyrin units form π stacked arrays with an inter-ligand distance ranging from 3-4 Å (Figure 5.10). The presence of these arrays and the broad UV-Vis absorption of the MOF across the visible spectrum prompted us to test the materials photocurrent response to chopped white LED light in LiClO₄ solution (see Experimental Details). Lithium based electrolyte was chosen due to the microporous nature of the material. A maximum photocurrent response of 330 nA/cm² was measured, suggesting some degree charge percolation through the material (Figure 5.10). However, after these measurements changes in the PXRD pattern of the material was observed. We suspected these changes arose from cation exchange as opposed to material instability. To test this hypothesis, the material was submerged in LiClO₄/MeCN solution for 3 days, with PXRD measurements taken on days 1 and 3 (Figure 5.11). These measurements confirmed our suspicion; after 3 days of exposure, two new low angle peaks appear at about 6° and 7.5° 2 θ , while an original peak at 12° 2 θ almost entirely disappears. Many other smaller peak changes can also be observed at various 2 θ angles. TGA measurements of the exchanged samples also support this conclusion, as the weight loss ascribed to the DMA⁺ molecules decreases from ~4.2% to about 0.7%, suggesting that about 84% of DMA⁺ is replaced

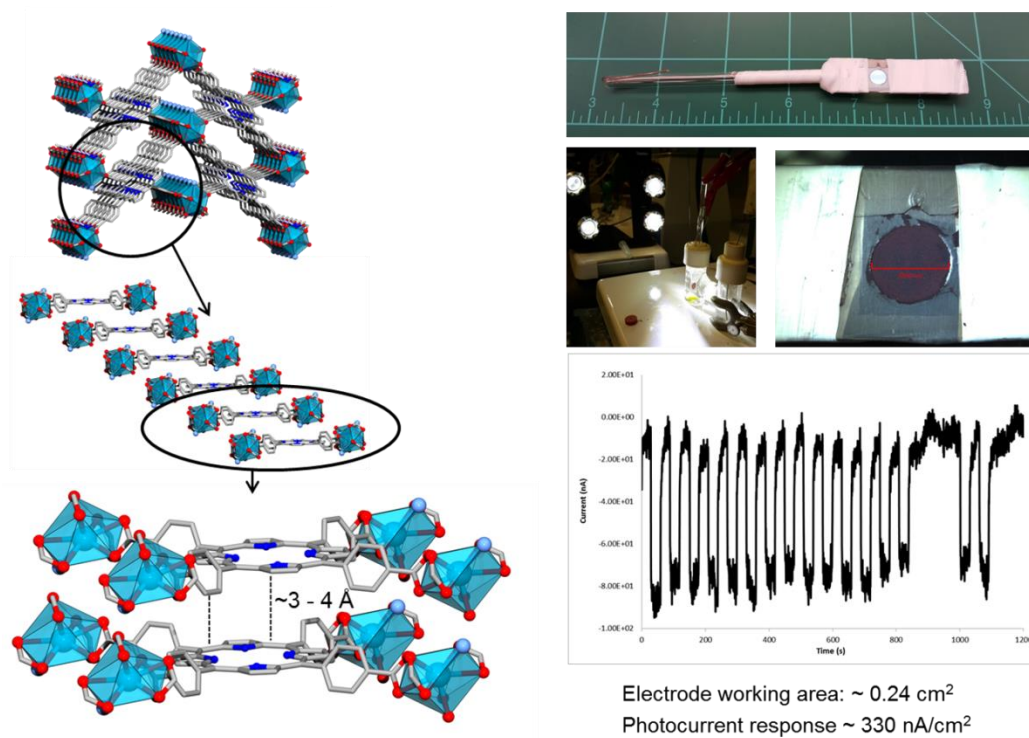


Figure 5.10. Depiction of π stacking in DMA⁺-Bi-tcpp, photographs of the ITO electrode used for photocurrent measurements, and photocurrent response under chopped white LED light at 30 sec intervals.

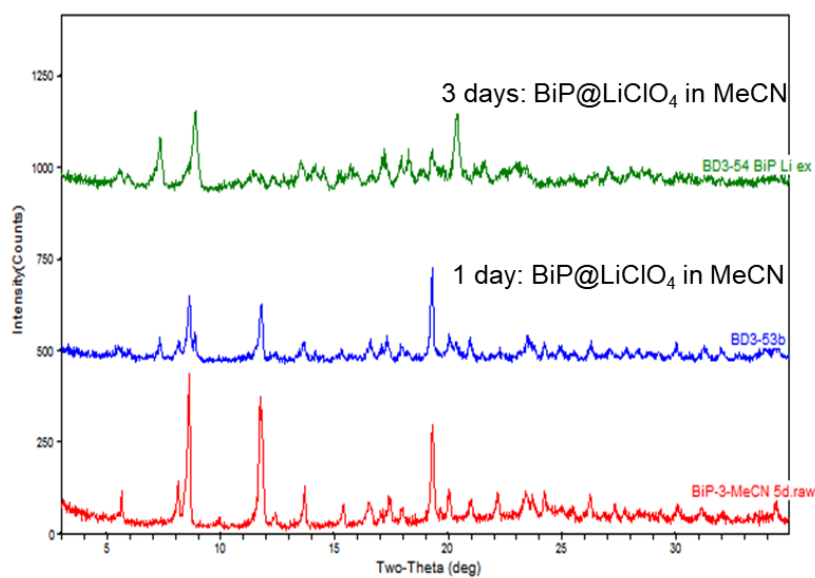


Figure 5.11. PXRD of DMA⁺-Bi-tcpp after 1 and 3 days of Li⁺ cation exchange.

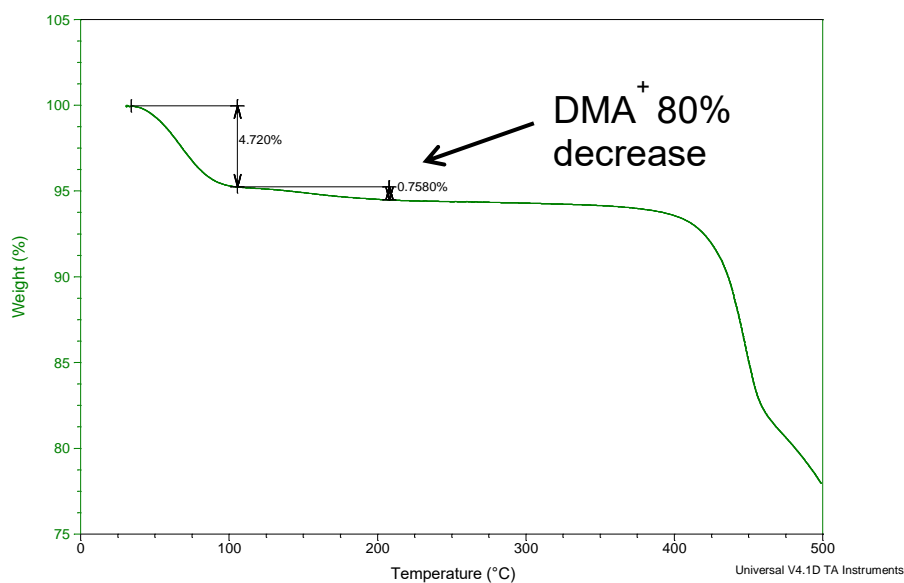


Figure 5.12. TGA profile of Li@Bi-tcpp after 3 days of exchange time.

by Li^+ . Interestingly, the exchange also appears to increase the thermal stability of the material, as the weight-loss ascribed to degradation of the porphyrin ligand at $\sim 395^\circ\text{C}$ is extended to $\sim 405^\circ\text{C}$. Attempts to maintain single-crystal integrity to crystallographically characterize these changes were unsuccessful, as the large crystals break down during the exchange into much smaller particles, indicating bond reformation or rearrangement taking place.

In order to structurally define the changes incurred during cation exchange with Li^+ , various amounts of Li^+ were added during synthesis, ranging from 2 (6.2 mg) – 50 (161.4 mg) molar equivalents. After a series of synthetic trials, PXRD measurements were used to compare the newly synthesized variants to the 3 day Li^+ exchanged material (Li@Bi-tcpp, Figure 5.13). Only beyond 15 eq. (40.4 mg) of added Li^+ is a single phase material, with PXRD peaks matching those of the new peaks of the Li@Bi-tcpp sample, obtained consistently. 50 eq. of Li^+ was chosen as standard synthetic conditions to ensure phase purity. Single crystals of the new Li^+ containing phase were obtained (see Experimental Details) and solved.

Li-Bi-tcpp also crystallizes in a monoclinic crystal system with a C2/c space group (Figure 5.4, Table 5.2); the asymmetric unit has one Li^+ cation, Bi^{+3} , tcpp and one coordinated

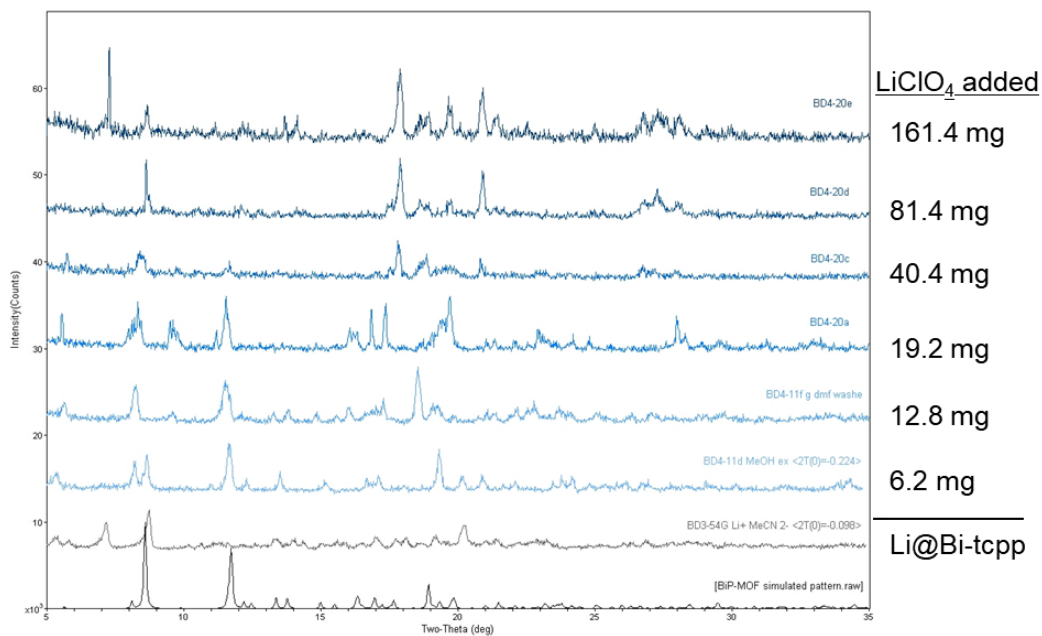


Figure 5.13. PXRD patterns for DMA^+ -Bi-tcpp (simulated, black), Li@Bi-tcpp (grey), and samples prepared with Li^+ present during synthetic trials (light to dark blue).

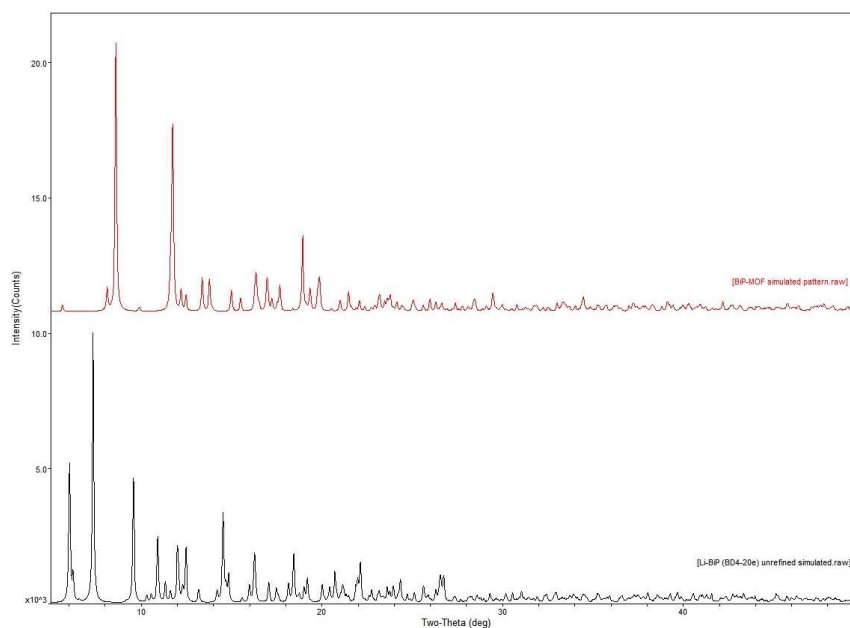


Figure 5.14. Simulated PXRD pattern comparison for Li-Bi-tcpp (bottom, black) and DMA^+ -Bi-tcpp (top, red).

DMF molecule. In contrast to $\text{DMA}^+\text{-Bi-tcpp}$, the newly formed phase is only 2-fold interpenetrated (Figure 5.5), and instead of being perfectly aligned, one of the two anionic nets is rotated around the crystallographic b-axis by 180° with respect to the other net. The Li^+ cations have tetrahedral coordination geometry generated by 4 O atoms. Two of the oxygens are from DMF solvent molecules coordinated exclusively to Li^+ , while the other two are $\mu_2\text{-O}$ bonds shared with the Bi^{3+} PBU; one from the terminally coordinated DMF solvent molecule (black ball), the other from a carboxylate. The structure is reminiscent of our previously reported Bi MOF, but differs in that the ‘chain’ of PBUs in Li-Bi-tcpp is not connected. The coordination sphere around Bi^{3+} is also quite different than in the case of $\text{DMA}^+\text{-Bi-tcpp}$. In this instance, no two Bi-O bonds share the same bond length, but follow the trend expected for Bi-carboxylate bonding, with one longer and one shorter bond. The longest Bi-O bond is from the terminally coordinated DMF molecule, with a distance of 2.864 Å, which is shared with Li^+ . As might be expected, the second longest bond is from the shared carboxylate $\mu_2\text{-O}$, at a distance of 2.715 Å, with the other Bi-O from the same carboxylate having a distance of 2.441 Å. The three other carboxylates have the following bond lengths, respectively: (2.702 Å, 2.230 Å), (2.660 Å, 2.369 Å), and (2.569 Å, 2.282 Å). In all cases, the Bi-O nearest to the Li^+ cation is the longer of the two Bi-O bonds from a single carboxylate. When the Bi-carboxylate connectivity is considered, the polyhedral geometry can also be described as a distorted tetrahedron (Figure 5.5). However, the tetrahedron has different angles than $\text{DMA}^+\text{-Bi-tcpp}$, due to rearrangement of the carboxylates around Bi, resulting in a slightly different structure with respect to the single nets of both $\text{DMA}^+\text{-Bi-tcpp}$ and Li-Bi-tcpp . These differences arise from the flexible/versatile nature of Bi coordination bonding.

Li-Bi-tcpp shares the same level of chemical stability as $\text{DMA}^+\text{-Bi-tcpp}$, but the thermal stability seems to be extended. The TGA profile (Figure 5.15) shows an initial ~20% weight loss from synthesis solvent, but the ~4% weight loss feature at 160 °C from DMA^+ is absent, and the

Table 5.2. Crystal data and structure refinement for Li-Bi-tcpp.

Identification code	Li-Bi-tcpp	
Empirical formula	C _{64.50} H ₆₇ Bi Li N _{9.50} O _{15.75}	
Formula weight	1443.19	
Temperature	100(2) K	
Wavelength	0.7749 Å	
Crystal system	Monoclinic	
Space group	C2/c	
Unit cell dimensions	a = 30.3090(13) Å	a = 90°.
	b = 16.1796(7) Å	b = 105.045(2)°.
	c = 30.2549(13) Å	g = 90°.
Volume	14328.1(11) Å ³	
Z	8	
Density (calculated)	1.338 Mg/m ³	
Absorption coefficient	2.725 mm ⁻¹	
F(000)	5860	
Crystal size	0.150 x 0.100 x 0.080 mm ³	
Theta range for data collection	2.042 to 38.077°.	
Index ranges	-48<=h<=48, -25<=k<=25, -48<=l<=48	
Reflections collected	485972	
Independent reflections	30172 [R(int) = 0.0499]	
Completeness to theta = 27.706°	99.8 %	
Absorption correction	Semi-empirical from equivalents	
Max. and min. transmission	0.811 and 0.682	
Refinement method	Full-matrix least-squares on F ²	
Data / restraints / parameters	30172 / 138 / 836	
Goodness-of-fit on F ²	1.103	
Final R indices [I>2sigma(I)]	R1 = 0.0445, wR2 = 0.1267	
R indices (all data)	R1 = 0.0579, wR2 = 0.1389	
Extinction coefficient	n/a	
Largest diff. peak and hole	2.458 and -2.692 e.Å ⁻³	

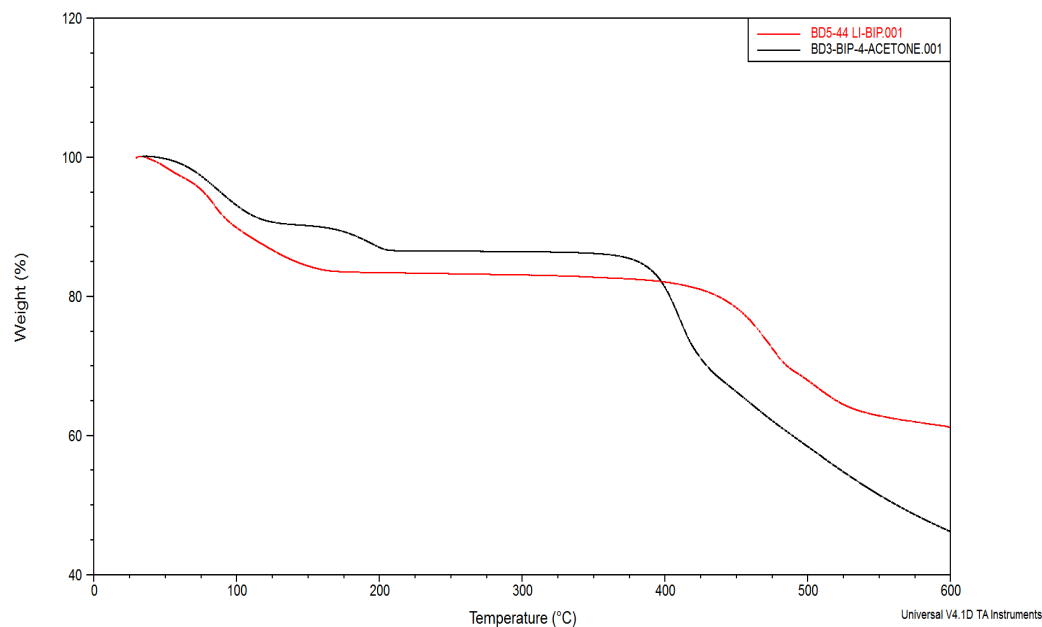


Figure 5.15. TGA profile for as-made Li-Bi-tcpp (red) and acetone exchanged DMA+-Bi-tcpp (black).

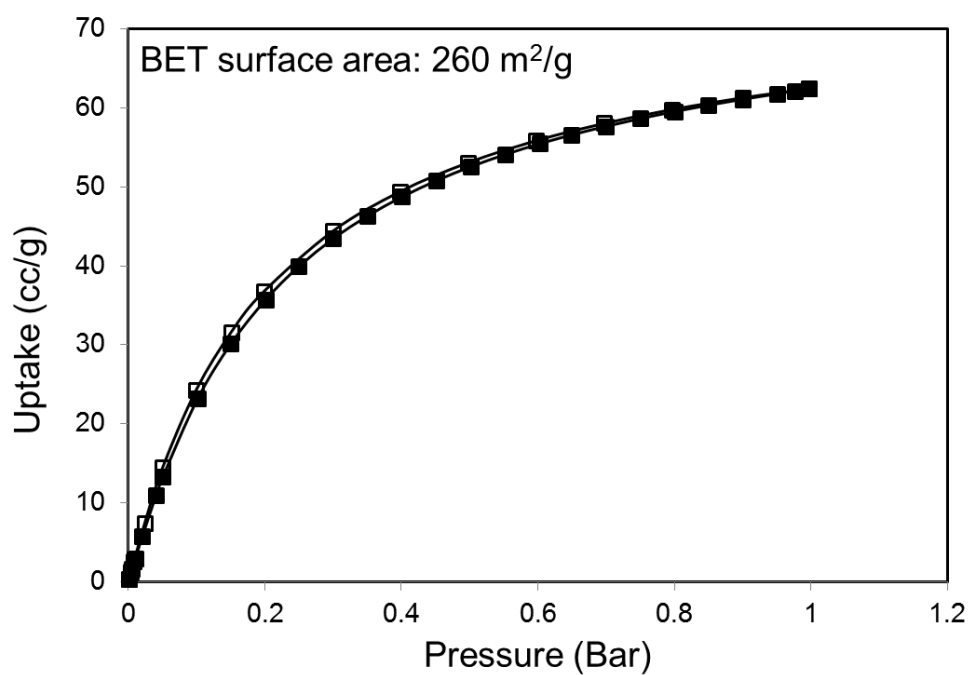


Figure 5.16. CO₂ sorption isotherm for Li-Bi-tcpp.

final weight loss from tcpp at 405 °C in the Li@Bi-tcpp is extended even further to about 425 °C, implying a greater degree of thermal stability. After solvent exchange with MeOH or MeCN following by outgassing at 80 °C, PXRD measurements show retention of the crystal structure. In contrast to DMA⁺-Bi-tcpp, the BET surface area of the material was able to be measured and was found to be 260 m²/g based on CO₂ sorption (Figure 5.16).

Based on reports of Bi activity for electrocatalytic CO₂ reduction, preliminary electrochemical measurements were performed. However, CV measurements on GCE (see Experimental Details) show little to no redox activity when scanning in the reductive direction up to an applied potential of -2.0 V vs. Ag/AgCl for the non-metalled parent structures, suggesting that Bi³⁺ will not be an accessible route for CO₂ reduction in these systems under these conditions. However, as metalloporphyrins are known to be CO₂ reduction catalysts, we tested various metallated versions of both Li-Bi-tcpp and DMA⁺-Bi-tcpp. In the cases of Cu²⁺, Ni²⁺, and Fe³⁺, (Figure 5.17 a-c) redox waves are observed at expected potentials corresponding to 1 electron reductions of the metal species. In the case of Li-Bi-tcpp-Fe, 3 different redox events were observed, corresponding to Fe (III/II), (II/I), and (I/0) redox couples. We focused on the Li-Bi-tcpp-Fe variant for bulk electrolysis (BE) measurements, as Fe-porphyrin species are documented to selectively produce CO at the (I/0) redox transition. For these measurements, LiClO₄ was used as supporting electrolyte as the Fe leeches out at the (I/0) couple when using TBAPF₆, which is ascribed to inability of the larger TBA⁺ cations to diffuse quickly enough through the material to stabilize the negatively charged framework upon reduction of Fe. Using LiClO₄ stabilizes the material and prevents such leeching. Catalyst inks comprised of conductive carbon (VXC72R) and Li-Bi-tcpp were applied to custom fabricated Toray working electrodes for extended BE measurements to improve catalyst loading. After two hours of BE (Figure 5.18d) at an applied potential of -1.7 V (vs. Ag/AgCl) in 0.1 M LiClO₄ with 0.5 M TFE added (see Experimental Details), CO is produced in approximately equal molar quantities as H₂ (Figure 5.19). Control experiments show that at this potential under these conditions, the bare Toray electrode produces

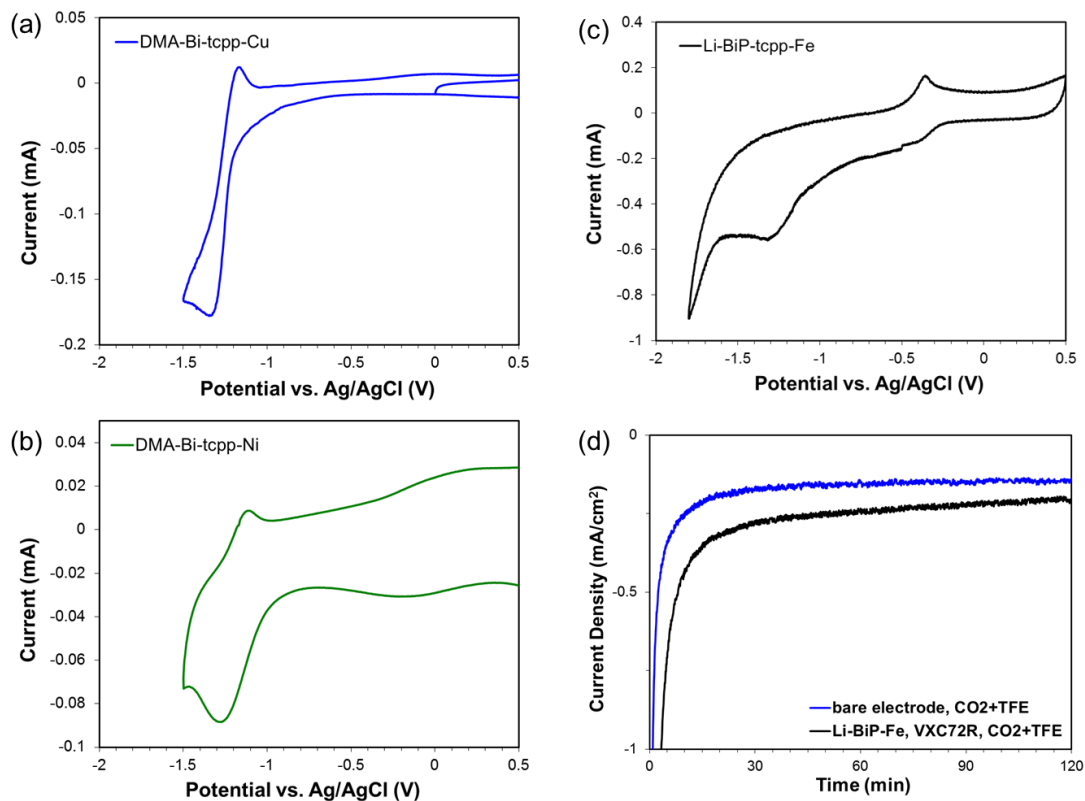


Figure 5.17. CV data for (a) DMA+Bi-tcpp-Cu, (b) DMA+Bi-tcpp-Ni, and (c) Li-Bi-tcpp-Fe. (d) BE data for the bare Toray electrode (blue) and Li-Bi-tcpp-Fe (black).

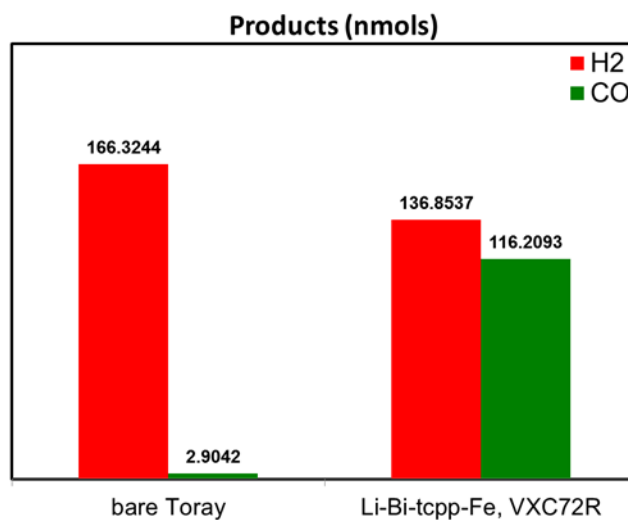


Figure 5.18. Product distribution after BE measurements on the bare Toray electrode and Li-Bi-tcpp-Fe with conductive carbon.

approximately the same quantity of H_2 , but little to no CO . This data can be considered as preliminary at best, and more electrochemical measurements are needed to fully characterize the materials performance, including metrics such as electroactive area, Tafel slope, and TOF/TON.

One of the most challenging elements of heterogenous electrocatalyst systems is obtaining good catalyst-electrode contact, especially in the case of MOF catalysts due to their insulating nature. In these cases, one should seek to grow ultra-thin films directly onto the electrode surface to maximize atom efficiency, as it is likely that only the atoms in direct contact with the electrode surface will be active. With this in mind, current efforts are focused on improving catalyst-electrode contact by utilizing a modulated synthetic approach to grow thin films of Bi-tcpp directly onto Toray carbon paper. Initial trials show that this is a promising

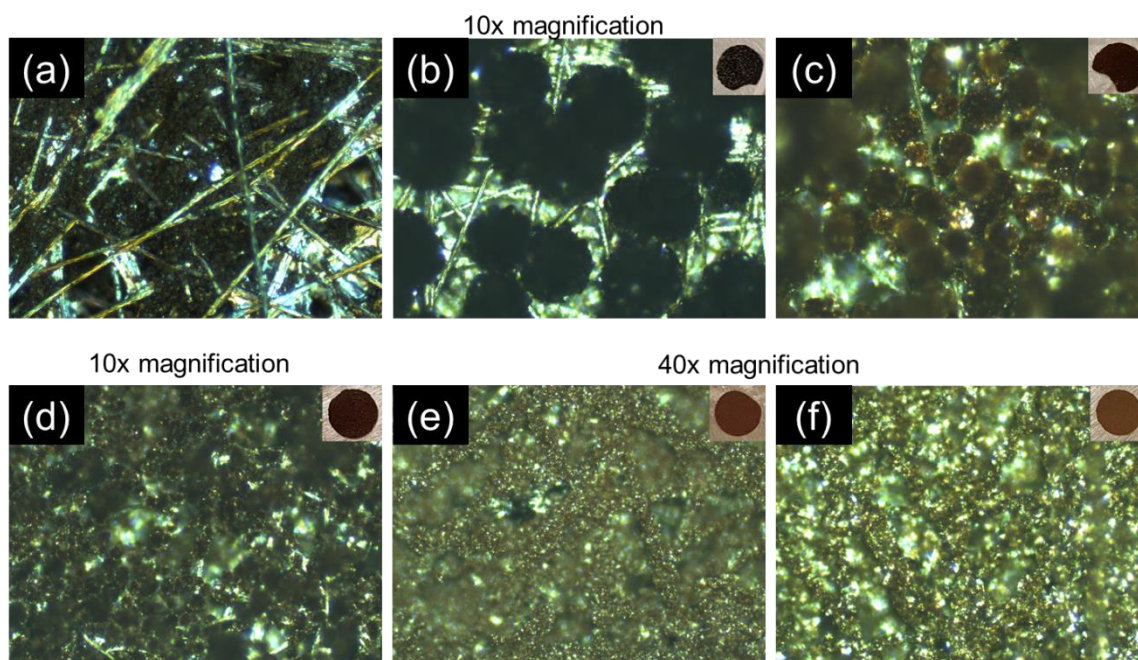


Figure 5.19. Optical micrographs of Li-Bi-tcpp-Fe/Toray composites. The inset images show zoomed out images of the coated carbon fiber paper; (a) manual application of catalyst showing poor catalyst-fiber contact, (b-f) direct growth on Toray paper with decreasing concentrations of benzoic acid.

approach (Figure 5.19). By reducing the MOF reaction time to 16 hr and varying the amount of benzoic acid modulator, crystal growth directly on the carbon fibers can be promoted. At higher benzoic acid concentrations, large crystal clusters can be observed to grow on the carbon fibers, but with poor coverage with respect to the total area (Figure 5.19 b, c, d). When the concentration of benzoic acid is minimized, a semi-uniform crystalline film is formed with complete coverage of the fibers (Figure 5.19 e, f). However, if no benzoic acid is employed, the correct phase is not obtained, as confirmed by PXRD measurements. This data suggests that by fine tuning the reaction conditions, an optimized thin crystalline film should be obtainable. Future work will focus on growing thinner films by further reducing reaction times and evaluating these electrode-MOF composite systems for electrocatalytic CO₂ reduction.

5.4 Future Outlook

Metal-organic frameworks have immense potential for many applications, but so far their use as electrocatalysts has been highly limited owing to a few factors, including poor conductivity and difficulty in fabricating electrodes. However, recent work has highlighted this potential by demonstrating a MOF electrocatalyst that is, according to the authors, the most efficient overall water splitting electrocatalyst reported to date.²²⁴ The key element in obtaining this level of performance is growing ultra-thin porous films directly on a conductive substrate, as well as having some degree of MOF conductivity. The spatial isolation of active sites intrinsic in MOF structures affords a theoretically ideal platform for catalysis, as the porous nature can provide access to each active site, a highly desirable feature from an atomic efficiency perspective. As the field further develops, it is doubtless that many more highly efficient systems will be discovered.

Appendix I

This project was coauthored by Dr. Jingming Zhang, who helped conceive the original idea and performed the preliminary material preparation and water oxidation experiments. The dissertation author was responsible for reproducing the work, performing analysis of the catalyst, as well as drafting the manuscript.

Appendix II

This project was coauthored by Ever Velasco, who helped perform ligand and MOF synthesis, as well as preliminary photoluminescence and UV-Vis experiments. The dissertation author conceived the original idea, performed all related experiments, and drafted the manuscript.

References

1. John, C.; Naomi, O.; Peter, T. D.; William, R. L. A.; Bart, V.; Ed, W. M.; Carlton, J. S.; Stephan, L.; Andrew, G. S.; Sarah, A. G.; Dana, N.; Peter, J.; Mark, R.; Bärbel, W.; Rob, P.; Ken, R., Consensus on consensus: a synthesis of consensus estimates on human-caused global warming. *Environmental Research Letters* **2016**, *11* (4), 048002.
2. Hulme, M., On the origin of 'the greenhouse effect': John Tyndall's 1859 interrogation of nature. *Weather* **2009**, *64* (5), 121-123.
3. Arrhenius, S., XXXI. On the influence of carbonic acid in the air upon the temperature of the ground. *Philosophical Magazine* **1896**, *41* (251), 237-276.
4. Högbom, A., Om Sannolikheten För Sekulära Förändringar I Atmosfärens Kolsyrehalt. *Svensk kemisk Tidskrift* **1894**, *6* (169), 77.
5. Shakun, J. D.; Clark, P. U.; He, F.; Marcott, S. A.; Mix, A. C.; Liu, Z.; Otto-Bliesner, B.; Schmittner, A.; Bard, E., Global warming preceded by increasing carbon dioxide concentrations during the last deglaciation. *Nature* **2012**, *484* (7392), 49-54.
6. Luthi, D.; Le Floch, M.; Bereiter, B.; Blunier, T.; Barnola, J.-M.; Siegenthaler, U.; Raynaud, D.; Jouzel, J.; Fischer, H.; Kawamura, K.; Stocker, T. F., High-resolution carbon dioxide concentration record 650,000-800,000[thinsp]years before present. *Nature* **2008**, *453* (7193), 379-382.
7. Bongaarts, J., Human population growth and the demographic transition. *Philosophical Transactions of the Royal Society B: Biological Sciences* **2009**, *364* (1532), 2985-2990.
8. BP Statistical Review of World Energy. **2017**.
9. Carbon Dioxide Information Analysis Center, Oak Ridge National Laboratory. **2015**.
10. Friedlingstein, P.; Andrew, R. M.; Rogelj, J.; Peters, G. P.; Canadell, J. G.; Knutti, R.; Luderer, G.; Raupach, M. R.; Schaeffer, M.; van Vuuren, D. P.; Le Quere, C., Persistent growth of CO₂ emissions and implications for reaching climate targets. *Nature Geosci* **2014**, *7* (10), 709-715.
11. <https://energy.gov/energysaver/led-lighting>. **2017**.
12. Li, H.; Eddaoudi, M.; O'Keeffe, M.; Yaghi, O. M., Design and synthesis of an exceptionally stable and highly porous metal-organic framework. *Nature* **1999**, *402* (6759), 276-279.
13. Cook, T. R.; Zheng, Y.-R.; Stang, P. J., Metal-Organic Frameworks and Self-Assembled Supramolecular Coordination Complexes: Comparing and Contrasting the Design, Synthesis and Functionality of Metal-Organic Materials. *Chem. Rev.* **2013**, *113* (1), 734-777.
14. Furukawa, H.; Ko, N.; Go, Y. B.; Aratani, N.; Choi, S. B.; Choi, E.; Yazaydin, A. Ö.; Snurr, R. Q.; O'Keeffe, M.; Kim, J.; Yaghi, O. M., Ultrahigh Porosity in Metal-Organic Frameworks. *Science* **2010**, *329* (5990), 424.
15. Furukawa, H.; Cordova, K. E.; O'Keeffe, M.; Yaghi, O. M., The Chemistry and Applications of Metal-Organic Frameworks. *Science* **2013**, *341* (6149).
16. Pettinari, C.; Marchetti, F.; Mosca, N.; Tosi, G.; Drozdov, A., Application of metal – organic frameworks. *Polym. Int.* **2017**, *66* (6), 731-744.
17. O'Keeffe, M.; Peskov, M. A.; Ramsden, S. J.; Yaghi, O. M., The Reticular Chemistry Structure Resource (RCSR) Database of, and Symbols for, Crystal Nets. *Acc. Chem. Res.* **2008**, *41* (12), 1782-1789.
18. Zhao, D.; Timmons, D. J.; Yuan, D.; Zhou, H.-C., Tuning the Topology and Functionality of Metal–Organic Frameworks by Ligand Design. *Acc. Chem. Res.* **2011**, *44* (2), 123-133.

19. Feng, D.; Gu, Z.-Y.; Li, J.-R.; Jiang, H.-L.; Wei, Z.; Zhou, H.-C., Zirconium-Metalloporphyrin PCN-222: Mesoporous Metal–Organic Frameworks with Ultrahigh Stability as Biomimetic Catalysts. *Angew. Chem. Int. Ed.* **2012**, *51* (41), 10307-10310.
20. Feng, D.; Chung, W.-C.; Wei, Z.; Gu, Z.-Y.; Jiang, H.-L.; Chen, Y.-P.; Darensbourg, D. J.; Zhou, H.-C., Construction of Ultrastable Porphyrin Zr Metal–Organic Frameworks through Linker Elimination. *J. Am. Chem. Soc.* **2013**, *135* (45), 17105-17110.
21. Jiang, H.-L.; Feng, D.; Wang, K.; Gu, Z.-Y.; Wei, Z.; Chen, Y.-P.; Zhou, H.-C., An Exceptionally Stable, Porphyrinic Zr Metal–Organic Framework Exhibiting pH-Dependent Fluorescence. *J. Am. Chem. Soc.* **2013**, *135* (37), 13934-13938.
22. Cavka, J. H.; Jakobsen, S.; Olsbye, U.; Guillou, N.; Lamberti, C.; Bordiga, S.; Lillerud, K. P., A New Zirconium Inorganic Building Brick Forming Metal Organic Frameworks with Exceptional Stability. *J. Am. Chem. Soc.* **2008**, *130* (42), 13850-13851.
23. Lin, C.-K.; Zhao, D.; Gao, W.-Y.; Yang, Z.; Ye, J.; Xu, T.; Ge, Q.; Ma, S.; Liu, D.-J., Tunability of Band Gaps in Metal–Organic Frameworks. *Inorg. Chem.* **2012**, *51* (16), 9039-9044.
24. Rowsell, J. L. C.; Yaghi, O. M., Metal–organic frameworks: a new class of porous materials. *Microporous Mesoporous Mater.* **2004**, *73* (1), 3-14.
25. Tsuruoka, T.; Furukawa, S.; Takashima, Y.; Yoshida, K.; Isoda, S.; Kitagawa, S., Nanoporous Nanorods Fabricated by Coordination Modulation and Oriented Attachment Growth. *Angew. Chem.* **2009**, *121* (26), 4833-4837.
26. Schaate, A.; Roy, P.; Godt, A.; Lippke, J.; Waltz, F.; Wiebcke, M.; Behrens, P., Modulated Synthesis of Zr-Based Metal–Organic Frameworks: From Nano to Single Crystals. *Chemistry – A European Journal* **2011**, *17* (24), 6643-6651.
27. Gutov, O. V.; Hevia, M. G.; Escudero-Adán, E. C.; Shafir, A., Metal–Organic Framework (MOF) Defects under Control: Insights into the Missing Linker Sites and Their Implication in the Reactivity of Zirconium-Based Frameworks. *Inorg. Chem.* **2015**, *54* (17), 8396-8400.
28. Bunaciu, A. A.; Udriștioiu, E. g.; Aboul-Enein, H. Y., X-Ray Diffraction: Instrumentation and Applications. *Crit. Rev. Anal. Chem.* **2015**, *45* (4), 289-299.
29. Mondloch, J. E.; Karagiari, O.; Farha, O. K.; Hupp, J. T., Activation of metal-organic framework materials. *CrystEngComm* **2013**, *15* (45), 9258-9264.
30. Limousin, G.; Gaudet, J. P.; Charlet, L.; Szenknect, S.; Barthès, V.; Krimissa, M., Sorption isotherms: A review on physical bases, modeling and measurement. *Appl. Geochem.* **2007**, *22* (2), 249-275.
31. Park, J.; Kim, H.; Han, S. S.; Jung, Y., Tuning Metal–Organic Frameworks with Open-Metal Sites and Its Origin for Enhancing CO₂ Affinity by Metal Substitution. *The Journal of Physical Chemistry Letters* **2012**, *3* (7), 826-829.
32. Chui, S. S. Y.; Lo, S. M. F.; Charmant, J. P. H.; Orpen, A. G.; Williams, I. D., A Chemically Functionalizable Nanoporous Material [Cu₃(TMA)₂(H₂O)₃]_n. *Science* **1999**, *283* (5405), 1148.
33. Serre, C.; Millange, F.; Surblé, S.; Férey, G., A Route to the Synthesis of Trivalent Transition-Metal Porous Carboxylates with Trimeric Secondary Building Units. *Angew. Chem. Int. Ed.* **2004**, *43* (46), 6285-6289.
34. Feng, D.; Wang, K.; Wei, Z.; Chen, Y.-P.; Simon, C. M.; Arvapally, R. K.; Martin, R. L.; Bosch, M.; Liu, T.-F.; Fordham, S.; Yuan, D.; Omary, M. A.; Haranczyk, M.; Smit, B.; Zhou, H.-C., Kinetically tuned dimensional augmentation as a versatile synthetic route towards robust metal–organic frameworks. **2014**, *5*, 5723.
35. Deibert, B. J.; Velasco, E.; Liu, W.; Teat, S. J.; Lustig, W. P.; Li, J., High-Performance Blue-Excitable Yellow Phosphor Obtained from an Activated Solvochromic Bismuth-Fluorophore Metal–Organic Framework. *Crystal Growth & Design* **2016**, *16* (8), 4178-4182.

36. Wang, C.; Xie, Z.; deKrafft, K. E.; Lin, W., Doping Metal–Organic Frameworks for Water Oxidation, Carbon Dioxide Reduction, and Organic Photocatalysis. *J. Am. Chem. Soc.* **2011**, *133* (34), 13445-13454.
37. Fei, H.; Sampson, M. D.; Lee, Y.; Kubiak, C. P.; Cohen, S. M., Photocatalytic CO₂ Reduction to Formate Using a Mn(I) Molecular Catalyst in a Robust Metal–Organic Framework. *Inorg. Chem.* **2015**, *54* (14), 6821-6828.
38. Liu, Y.; Yang, Y.; Sun, Q.; Wang, Z.; Huang, B.; Dai, Y.; Qin, X.; Zhang, X., Chemical Adsorption Enhanced CO₂ Capture and Photoreduction over a Copper Porphyrin Based Metal Organic Framework. *ACS Applied Materials & Interfaces* **2013**, *5* (15), 7654-7658.
39. Hod, I.; Sampson, M. D.; Deria, P.; Kubiak, C. P.; Farha, O. K.; Hupp, J. T., Fe-Porphyrin-Based Metal–Organic Framework Films as High-Surface Concentration, Heterogeneous Catalysts for Electrochemical Reduction of CO₂. *ACS Catalysis* **2015**, *5* (11), 6302-6309.
40. Kornienko, N.; Zhao, Y.; Kley, C. S.; Zhu, C.; Kim, D.; Lin, S.; Chang, C. J.; Yaghi, O. M.; Yang, P., Metal–Organic Frameworks for Electrocatalytic Reduction of Carbon Dioxide. *J. Am. Chem. Soc.* **2015**, *137* (44), 14129-14135.
41. Zhang, H.; Wei, J.; Dong, J.; Liu, G.; Shi, L.; An, P.; Zhao, G.; Kong, J.; Wang, X.; Meng, X.; Zhang, J.; Ye, J., Efficient Visible-Light-Driven Carbon Dioxide Reduction by a Single-Atom Implanted Metal–Organic Framework. *Angew. Chem. Int. Ed.* **2016**, *55* (46), 14310-14314.
42. Xu, H.-Q.; Hu, J.; Wang, D.; Li, Z.; Zhang, Q.; Luo, Y.; Yu, S.-H.; Jiang, H.-L., Visible-Light Photoreduction of CO₂ in a Metal–Organic Framework: Boosting Electron–Hole Separation via Electron Trap States. *J. Am. Chem. Soc.* **2015**, *137* (42), 13440-13443.
43. Hu, Z.; Deibert, B. J.; Li, J., Luminescent metal-organic frameworks for chemical sensing and explosive detection. *Chem. Soc. Rev.* **2014**, *43* (16), 5815-5840.
44. Gong, Q.; Hu, Z.; Deibert, B. J.; Emge, T. J.; Teat, S. J.; Banerjee, D.; Mussman, B.; Rudd, N. D.; Li, J., Solution Processable MOF Yellow Phosphor with Exceptionally High Quantum Efficiency. *J. Am. Chem. Soc.* **2014**, *136* (48), 16724-16727.
45. Hu, Z.; Huang, G.; Lustig, W. P.; Wang, F.; Wang, H.; Teat, S. J.; Banerjee, D.; Zhang, D.; Li, J., Achieving exceptionally high luminescence quantum efficiency by immobilizing an AIE molecular chromophore into a metal-organic framework. *Chem. Commun.* **2015**, *51* (15), 3045-3048.
46. Hu, Z.; Lustig, W. P.; Zhang, J.; Zheng, C.; Wang, H.; Teat, S. J.; Gong, Q.; Rudd, N. D.; Li, J., Effective Detection of Mycotoxins by a Highly Luminescent Metal–Organic Framework. *J. Am. Chem. Soc.* **2015**, *137* (51), 16209-16215.
47. Rocha, J.; Carlos, L. D.; Paz, F. A. A.; Ananias, D., Luminescent multifunctional lanthanides-based metal-organic frameworks. *Chem. Soc. Rev.* **2011**, *40* (2), 926-940.
48. Gouterman, M., Spectra of porphyrins. *J. Mol. Spectrosc.* **1961**, *6* (Supplement C), 138-163.
49. Ishihara, S.; Labuta, J.; Van Rossom, W.; Ishikawa, D.; Minami, K.; Hill, J. P.; Ariga, K., Porphyrin-based sensor nanoarchitectonics in diverse physical detection modes. *PCCP* **2014**, *16* (21), 9713-9746.
50. Deibert, B. J.; Li, J., A distinct reversible colorimetric and fluorescent low pH response on a water-stable zirconium-porphyrin metal-organic framework. *Chem. Commun.* **2014**, *50* (68), 9636-9639.
51. Deibert, B. J.; Zhang, J.; Smith, P. F.; Chapman, K. W.; Rangan, S.; Banerjee, D.; Tan, K.; Wang, H.; Pasquale, N.; Chen, F.; Lee, K.-B.; Dismukes, G. C.; Chabal, Y. J.; Li, J., Surface and Structural Investigation of a MnOx Birnessite-Type Water Oxidation Catalyst Formed under Photocatalytic Conditions. *Chemistry – A European Journal* **2015**, *21* (40), 14218-14228.
52. Kärkäs, M. D.; Verho, O.; Johnston, E. V.; Åkermark, B., Artificial Photosynthesis: Molecular Systems for Catalytic Water Oxidation. *Chem. Rev.* **2014**, *114* (24), 11863-12001.

53. Young, K. J.; Martini, L. A.; Milot, R. L.; Snoeberger Iii, R. C.; Batista, V. S.; Schmuttenmaer, C. A.; Crabtree, R. H.; Brudvig, G. W., Light-driven water oxidation for solar fuels. *Coord. Chem. Rev.* **2012**, 256 (21–22), 2503-2520.
54. Tachibana, Y.; Vayssieres, L.; Durrant, J. R., Artificial photosynthesis for solar water-splitting. *Nat. Photon* **2012**, 6 (8), 511-518.
55. Archana Singh, L. S., Water oxidation catalysts based on abundant 1st row transition metals. *Coord. Chem. Rev.* **2013**, 257, 2607-2622.
56. Berardi, S.; Drouet, S.; Francas, L.; Gimbert-Surinach, C.; Guttentag, M.; Richmond, C.; Stoll, T.; Llobet, A., Molecular artificial photosynthesis. *Chem. Soc. Rev.* **2014**, 43 (22), 7501-7519.
57. Concepcion, J. J.; Jurss, J. W.; Brennaman, M. K.; Hoertz, P. G.; Patrocinio, A. O. T.; Murakami Iha, N. Y.; Templeton, J. L.; Meyer, T. J., Making Oxygen with Ruthenium Complexes. *Acc. Chem. Res.* **2009**, 42 (12), 1954-1965.
58. Morris, N. D.; Suzuki, M.; Mallouk, T. E., Kinetics of Electron Transfer and Oxygen Evolution in the Reaction of [Ru(bpy)₃]³⁺ with Colloidal Iridium Oxide. *J. Phys. Chem. A* **2004**, 108 (42), 9115-9119.
59. Nakamura, R.; Frei, H., Visible Light-Driven Water Oxidation by Ir Oxide Clusters Coupled to Single Cr Centers in Mesoporous Silica. *J. Am. Chem. Soc.* **2006**, 128 (33), 10668-10669.
60. Geletii, Y. V.; Huang, Z.; Hou, Y.; Musaev, D. G.; Lian, T.; Hill, C. L., Homogeneous Light-Driven Water Oxidation Catalyzed by a Tetra Ruthenium Complex with All Inorganic Ligands. *J. Am. Chem. Soc.* **2009**, 131 (22), 7522-7523.
61. Youngblood, W. J.; Lee, S.-H. A.; Kobayashi, Y.; Hernandez-Pagan, E. A.; Hoertz, P. G.; Moore, T. A.; Moore, A. L.; Gust, D.; Mallouk, T. E., Photoassisted Overall Water Splitting in a Visible Light-Absorbing Dye-Sensitized Photoelectrochemical Cell. *J. Am. Chem. Soc.* **2009**, 131 (3), 926-927.
62. James P. McEvoy, G. W. B., Water-Splitting Chemistry of Photosystem II. *Chem. Rev.* **2006**, 106 (11), 4455-4483.
63. Umena, Y.; Kawakami, K.; Shen, J. R.; Kamiya, N., Crystal structure of oxygen-evolving photosystem II at a resolution of 1.9 Å. *Nature* **2011**, 473 (7345), 55-60.
64. Wiechen, M.; Najafpour, M. M.; Allakhverdiev, S. I.; Spiccia, L., Water oxidation catalysis by manganese oxides: learning from evolution. *Energy Environ. Sci.* **2014**, 7 (7), 2203-2212.
65. Meng, Y.; Song, W.; Huang, H.; Ren, Z.; Chen, S. Y.; Suib, S. L., Structure-property relationship of bifunctional MnO₂ nanostructures: highly efficient, ultra-stable electrochemical water oxidation and oxygen reduction reaction catalysts identified in alkaline media. *J. Am. Chem. Soc.* **2014**, 136 (32), 11452-64.
66. Frey, C. E.; Wiechen, M.; Kurz, P., Water-oxidation catalysis by synthetic manganese oxides--systematic variations of the calcium birnessite theme. *Dalton transactions* **2014**, 43 (11), 4370-9.
67. Wiechen, M.; Zaharieva, I.; Dau, H.; Kurz, P., Layered manganese oxides for water-oxidation: alkaline earth cations influence catalytic activity in a photosystem II-like fashion. *Chem. Sci.* **2012**, 3 (7), 2330.
68. Iyer, A.; Del-Pilar, J.; King'ondo, C. K.; Kissel, E.; Garces, H. F.; Huang, H.; El-Sawy, A. M.; Dutta, P. K.; Suib, S. L., Water Oxidation Catalysis using Amorphous Manganese Oxides, Octahedral Molecular Sieves (OMS-2), and Octahedral Layered (OL-1) Manganese Oxide Structures. *J. Phys. Chem. C* **2012**, 116 (10), 6474-6483.
69. Zaharieva, I.; Najafpour, M. M.; Wiechen, M.; Haumann, M.; Kurz, P.; Dau, H., Synthetic manganese-calcium oxides mimic the water-oxidizing complex of photosynthesis functionally and structurally. *Energy Environ. Sci.* **2011**, 4 (7), 2400-2408.

70. Mukhopadhyay, S.; Mandal, S. K.; Bhaduri, S.; Armstrong, W. H., Manganese Clusters with Relevance to Photosystem II. *Chem. Rev.* **2004**, *104* (9), 3981-4026.
71. Robinson, D. M.; Go, Y. B.; Mui, M.; Gardner, G.; Zhang, Z.; Mastrogiovanni, D.; Garfunkel, E.; Li, J.; Greenblatt, M.; Dismukes, G. C., Photochemical water oxidation by crystalline polymorphs of manganese oxides: structural requirements for catalysis. *J. Am. Chem. Soc.* **2013**, *135* (9), 3494-501.
72. Huynh, M.; Bediako, D. K.; Nocera, D. G., A functionally stable manganese oxide oxygen evolution catalyst in acid. *J. Am. Chem. Soc.* **2014**, *136* (16), 6002-10.
73. Robinson, D. M.; Go, Y. B.; Greenblatt, M.; Dismukes, G. C., Water Oxidation by λ -MnO₂: Catalysis by the Cubical Mn₄O₄ Subcluster Obtained by Delithiation of Spinel LiMn₂O₄. *J. Am. Chem. Soc.* **2010**, *132* (33), 11467-11469.
74. Najafpour, M. M.; Ehrenberg, T.; Wiechen, M.; Kurz, P., Calcium Manganese(III) Oxides (CaMn₂O₄·x H₂O) as Biomimetic Oxygen-Evolving Catalysts. *Angew. Chem. Int. Ed.* **2010**, *49* (12), 2233-2237.
75. Jiao, F.; Frei, H., Nanostructured cobalt and manganese oxide clusters as efficient water oxidation catalysts. *Energy Environ. Sci.* **2010**, *3* (8), 1018-1027.
76. Dismukes, G. C.; Brimblecombe, R.; Felton, G. A. N.; Pryadun, R. S.; Sheats, J. E.; Spiccia, L.; Swiegers, G. F., Development of Bioinspired Mn₄O₄-Cubane Water Oxidation Catalysts: Lessons from Photosynthesis. *Acc. Chem. Res.* **2009**, *42* (12), 1935-1943.
77. Harriman, A.; Pickering, I. J.; Thomas, J. M.; Christensen, P. A., Metal oxides as heterogeneous catalysts for oxygen evolution under photochemical conditions. *Journal of the Chemical Society, Faraday Transactions 1: Physical Chemistry in Condensed Phases* **1988**, *84* (8), 2795-2806.
78. Okuno, Y.; Yonemitsu, O.; Chiba, Y., MANGANESE DIOXIDE AS SPECIFIC REDOX CATALYST IN THE PHOTSENSITIZED OXYGEN GENERATION FROM WATER. *Chem. Lett.* **1983**, *12* (6), 815-818.
79. Menezes, P. W.; Indra, A.; Levy, O.; Kailasam, K.; Gutkin, V.; Pfrommer, J.; Driess, M., Using nickel manganese oxide catalysts for efficient water oxidation. *Chem. Commun.* **2015**, *51* (24), 5005-5008.
80. Singh, A.; Hocking, R. K.; Chang, S. L. Y.; George, B. M.; Fehr, M.; Lips, K.; Schnegg, A.; Spiccia, L., Water Oxidation Catalysis by Nanoparticulate Manganese Oxide Thin Films: Probing the Effect of the Manganese Precursors. *Chem. Mater.* **2013**, *25* (7), 1098-1108.
81. Bergmann, A.; Zaharieva, I.; Dau, H.; Strasser, P., Electrochemical water splitting by layered and 3D cross-linked manganese oxides: correlating structural motifs and catalytic activity. *Energy & Environmental Science* **2013**, *6* (9), 2745.
82. Zaharieva, I.; Chernev, P.; Risch, M.; Klingan, K.; Kohlhoff, M.; Fischer, A.; Dau, H., Electrosynthesis, functional, and structural characterization of a water-oxidizing manganese oxide. *Energy Environ. Sci.* **2012**, *5* (5), 7081.
83. Takashima, T.; Hashimoto, K.; Nakamura, R., Mechanisms of pH-dependent activity for water oxidation to molecular oxygen by MnO₂ electrocatalysts. *J. Am. Chem. Soc.* **2012**, *134* (3), 1519-27.
84. Takashima, T.; Hashimoto, K.; Nakamura, R., Inhibition of charge disproportionation of MnO₂ electrocatalysts for efficient water oxidation under neutral conditions. *J. Am. Chem. Soc.* **2012**, *134* (44), 18153-6.
85. Pinaud, B. A.; Chen, Z.; Abram, D. N.; Jaramillo, T. F., Thin Films of Sodium Birnessite-Type MnO₂: Optical Properties, Electronic Band Structure, and Solar Photoelectrochemistry. *J. Phys. Chem. C* **2011**, *115* (23), 11830-11838.
86. Glover, E. D., Characterization of a marine birnessite. *Am. Mineral.* **1977**, *62* (3-4), 278-285.
87. Taylor, R.; McKenzie, R.; Norrish, K., The mineralogy and chemistry of manganese in some Australian soils. *Soil Research* **1964**, *2* (2), 235-248.

88. Cygan, R. T.; Post, J. E.; Heaney, P. J.; Kubicki, J. D., Molecular models of birnessite and related hydrated layered minerals. *Am. Mineral.* **2012**, *97* (8-9), 1505-1514.
89. Villalobos, M.; Lanson, B.; Manceau, A.; Toner, B.; Sposito, G., Structural model for the biogenic Mn oxide produced by *Pseudomonas putida*. *Am. Mineral.* **2006**, *91* (4), 489-502.
90. Villalobos, M.; Toner, B.; Bargar, J.; Sposito, G., Characterization of the manganese oxide produced by *pseudomonas putida* strain MnB1. *Geochim. Cosmochim. Acta* **2003**, *67* (14), 2649-2662.
91. Lanson B., D. V. A., Feng Q., Manceau A., Structure of synthetic Na-birnessite: Evidence for a triclinic one-layer unit cell. *Am. Mineral.* **2002**, *87*, 1662-2002.
92. Bruno Lanson, V. A. D., Ewen Silvester, Alain Manceau, Structure of H-exchanged hexagonal birnessite and its mechanism of formation from Na-rich monoclinic buserite at low pH. *Am. Mineral.* **2000**, *85*, 826-838.
93. Drits V.A., S. E., Gorshkov A.I, Manceau A., Structure of synthetic monoclinic Na-rich birnessite and hexagonal birnessite; I, Results from X-ray diffraction and selected-area electron diffraction. *Am. Mineral.* **1997**, *October 1997* (82), 946-961.
94. Indra, A.; Menezes, P. W.; Driess, M., Uncovering Structure–Activity Relationships in Manganese-Oxide-Based Heterogeneous Catalysts for Efficient Water Oxidation. *ChemSusChem* **2015**, *8* (5), 776-785.
95. Hocking, R. K.; Malaeb, R.; Gates, W. P.; Patti, A. F.; Chang, S. L. Y.; Devlin, G.; MacFarlane, D. R.; Spiccia, L., Formation of a Nanoparticulate Birnessite-Like Phase in Purported Molecular Water Oxidation Catalyst Systems. *ChemCatChem* **2014**, *6* (7), 2028-2038.
96. Najafpour, M. M.; Moghaddam, A. N.; Dau, H.; Zaharieva, I., Fragments of layered manganese oxide are the real water oxidation catalyst after transformation of molecular precursor on clay. *J. Am. Chem. Soc.* **2014**, *136* (20), 7245-8.
97. Hocking, R. K.; Brimblecombe, R.; Chang, L. Y.; Singh, A.; Cheah, M. H.; Glover, C.; Casey, W. H.; Spiccia, L., Water-oxidation catalysis by manganese in a geochemical-like cycle. *Nature chemistry* **2011**, *3* (6), 461-6.
98. Menezes, P. W.; Indra, A.; Littlewood, P.; Schwarze, M.; Göbel, C.; Schomäcker, R.; Driess, M., Nanostructured Manganese Oxides as Highly Active Water Oxidation Catalysts: A Boost from Manganese Precursor Chemistry. *ChemSusChem* **2014**, *7* (8), 2202-2211.
99. Indra, A.; Menezes, P. W.; Zaharieva, I.; Baktash, E.; Pfrommer, J.; Schwarze, M.; Dau, H.; Driess, M., Active Mixed-Valent MnOx Water Oxidation Catalysts through Partial Oxidation (Corrosion) of Nanostructured MnO Particles. *Angew. Chem. Int. Ed.* **2013**, *52* (50), 13206-13210.
100. Demars, T. J.; Bera, M. K.; Seifert, S.; Antonio, M. R.; Ellis, R. J., Revisiting the Solution Structure of Ceric Ammonium Nitrate. *Angew. Chem. Int. Ed.* **2015**, n/a-n/a.
101. Cui, Y.; Yue, Y.; Qian, G.; Chen, B., Luminescent Functional Metal–Organic Frameworks. *Chem. Rev.* **2011**, *112* (2), 1126-1162.
102. Li, J.-R.; Sculley, J.; Zhou, H.-C., Metal–Organic Frameworks for Separations. *Chem. Rev.* **2011**, *112* (2), 869-932.
103. Sumida, K.; Rogow, D. L.; Mason, J. A.; McDonald, T. M.; Bloch, E. D.; Herm, Z. R.; Bae, T.-H.; Long, J. R., Carbon Dioxide Capture in Metal–Organic Frameworks. *Chem. Rev.* **2011**, *112* (2), 724-781.
104. Wu, H.; Gong, Q.; Olson, D. H.; Li, J., Commensurate Adsorption of Hydrocarbons and Alcohols in Microporous Metal Organic Frameworks. *Chem. Rev.* **2012**, *112* (2), 836-868.
105. Zhou, H.-C.; Long, J. R.; Yaghi, O. M., Introduction to Metal–Organic Frameworks. *Chem. Rev.* **2012**, *112* (2), 673-674.
106. Fu, Y.; Sun, D.; Chen, Y.; Huang, R.; Ding, Z.; Fu, X.; Li, Z., An Amine-Functionalized Titanium Metal–Organic Framework Photocatalyst with Visible-Light-Induced Activity for CO₂ Reduction. *Angew. Chem. Int. Ed.* **2012**, *51* (14), 3364-3367.

107. Zhang, J.; Biradar, A. V.; Pramanik, S.; Emge, T. J.; Asefa, T.; Li, J., A new layered metal-organic framework as a promising heterogeneous catalyst for olefin epoxidation reactions. *Chem. Commun.* **2012**, 48 (52), 6541-6543.
108. Tian, C.-B.; Zhang, H.-B.; Peng, Y.; Xie, Y.-E.; Lin, P.; Li, Z.-H.; Du, S.-W., Synthesis, Structures, and Magnetic Properties of Three 3D Coordination Polymers Based on M4O4 Cubanes (M = MnII, FeII, CoII). *Eur. J. Inorg. Chem.* **2012**, 2012 (25), 4029-4035.
109. Saratovsky, I.; Wightman, P. G.; Pastén, P. A.; Gaillard, J.-F.; Poeppelmeier, K. R., Manganese Oxides: Parallels between Abiotic and Biotic Structures. *J. Am. Chem. Soc.* **2006**, 128 (34), 11188-11198.
110. Gaillot, A.-C.; Flot, D.; Drits, V. A.; Manceau, A.; Burghammer, M.; Lanson, B., Structure of Synthetic K-rich Birnessite Obtained by High-Temperature Decomposition of KMnO₄. I. Two-Layer Polytype from 800 °C Experiment. *Chem. Mater.* **2003**, 15 (24), 4666-4678.
111. Wang, X.; Li, Y., Selected-Control Hydrothermal Synthesis of α - and β -MnO₂ Single Crystal Nanowires. *J. Am. Chem. Soc.* **2002**, 124 (12), 2880-2881.
112. Gupta, R. P.; Sen, S. K., Calculation of multiplet structure of core $3p$ -vacancy levels. *Physical Review B* **1974**, 10 (1), 71-77.
113. Nesbitt, H. W.; Banerjee, D., Interpretation of XPS Mn(2p) spectra of Mn oxyhydroxides and constraints on the mechanism of MnO₂ precipitation. *Am. Mineral.* **1998**, 83 (3-4), 305-315.
114. Post, J. E.; Veblen, D. R., Crystal structure determinations of synthetic sodium, magnesium, and potassium birnessite using TEM and the Rietveld method. *Am. Mineral.* **1990**, 75 (5-6), 477-489.
115. Lewandowski, W.; Barańska, H.; Mościbroda, P., Vibrational study of nicotinic acid complexes with different central ions. *Journal of Raman Spectroscopy* **1993**, 24 (12), 819-824.
116. Sala, O.; Gonçalves, N. S.; Noda, L. K., Vibrational analysis of nicotinic acid species based on ab initio molecular orbital calculations. *J. Mol. Struct.* **2001**, 565-566 (0), 411-416.
117. Smith, P. F.; Kaplan, C.; Sheats, J. E.; Robinson, D. M.; McCool, N. S.; Mezle, N.; Dismukes, G. C., What Determines Catalyst Functionality in Molecular Water Oxidation? Dependence on Ligands and Metal Nuclearity in Cobalt Clusters. *Inorg. Chem.* **2014**, 53 (4), 2113-2121.
118. Huang, Z.; Luo, Z.; Geletii, Y. V.; Vickers, J. W.; Yin, Q.; Wu, D.; Hou, Y.; Ding, Y.; Song, J.; Musaev, D. G.; Hill, C. L.; Lian, T., Efficient Light-Driven Carbon-Free Cobalt-Based Molecular Catalyst for Water Oxidation. *J. Am. Chem. Soc.* **2011**, 133 (7), 2068-2071.
119. Crisostomo, V. M. B.; Ngala, J. K.; Alia, S.; Doble, A.; Morein, C.; Chen, C.-H.; Shen, X.; Suib, S. L., New Synthetic Route, Characterization, and Electrocatalytic Activity of Nanosized Manganite. *Chem. Mater.* **2007**, 19 (7), 1832-1839.
120. Ramírez, A.; Hillebrand, P.; Stellmach, D.; May, M. M.; Bogdanoff, P.; Fiechter, S., Evaluation of MnO_x, Mn₂O₃, and Mn₃O₄ Electrodeposited Films for the Oxygen Evolution Reaction of Water. *J. Phys. Chem. C* **2014**, 118 (26), 14073-14081.
121. Gorlin, Y.; Jaramillo, T. F., Investigation of Surface Oxidation Processes on Manganese Oxide Electrocatalysts Using Electrochemical Methods and Ex Situ X-ray Photoelectron Spectroscopy. *J. Electrochem. Soc.* **2012**, 159 (10), H782-H786.
122. Marafatto, F. F.; Strader, M. L.; Gonzalez-Holguera, J.; Schwartzberg, A.; Gilbert, B.; Peña, J., Rate and mechanism of the photoreduction of birnessite (MnO₂) nanosheets. *Proceedings of the National Academy of Sciences* **2015**, 112 (15), 4600-4605.
123. Chupas, P. J.; Qiu, X. Y.; Hanson, J. C.; Lee, P. L.; Grey, C. P.; Billinge, S. J. L., Rapid-acquisition pair distribution function (RA-PDF) analysis. *J. Appl. Crystallogr.* **2003**, 36, 1342-1347.
124. Egami, T.; Billinge, S. J. L., *Underneath the Bragg Peaks Structural Analysis of Complex Materials*. Pergamon: Oxford, UK, 2003.

125. Billinge, S. J. L.; Kanatzidis, M. G., Beyond crystallography: the study of disorder, nanocrystallinity and crystallographically challenged materials with pair distribution functions. *Chem. Commun.* **2004**, (7), 749-760.
126. Chupas, P. J.; Chapman, K. W.; Lee, P. L., Applications of an amorphous silicon-based area detector for high-resolution, high-sensitivity and fast time-resolved pair distribution function measurements. *J. Appl. Crystallogr.* **2007**, *40*, 463-470.
127. Lee, J. H.; Aydinler, C. C.; Almer, J.; Bernier, J.; Chapman, K. W.; Chupas, P. J.; Haefner, D.; Kump, K.; Lee, P. L.; Lienert, U.; Miceli, A.; Vera, G., Synchrotron applications of an amorphous silicon flat-panel detector. *Journal of Synchrotron Radiation* **2008**, *15*, 477-488.
128. Du, P.; Kokhan, O.; Chapman, K. W.; Chupas, P. J.; Tiede, D. M., Elucidating the Domain Structure of the Cobalt Oxide Water Splitting Catalyst by X-ray Pair Distribution Function Analysis. *J. Am. Chem. Soc.* **2012**, *134* (27), 11096-11099.
129. Wojdyr, M., Fityk: a general-purpose peak fitting program. *J. Appl. Cryst.* **2010**, *43*, 1126-1128.
130. Zhu, M.; Farrow, C. L.; Post, J. E.; Livi, K. J. T.; Billinge, S. J. L.; Ginder-Vogel, M.; Sparks, D. L., Structural study of biotic and abiotic poorly-crystalline manganese oxides using atomic pair distribution function analysis. *Geochim. Cosmochim. Acta* **2012**, *81* (0), 39-55.
131. Julien, C.; Massot, M.; Baddour-Hadjean, R.; Franger, S.; Bach, S.; Pereira-Ramos, J. P., Raman spectra of birnessite manganese dioxides. *Solid State Ionics* **2003**, *159* (3-4), 345-356.
132. Hsu, Y.-K.; Chen, Y.-C.; Lin, Y.-G.; Chen, L.-C.; Chen, K.-H., Reversible phase transformation of MnO₂ nanosheets in an electrochemical capacitor investigated by in situ Raman spectroscopy. *Chem. Commun.* **2011**, 47 (4), 1252-1254.
133. Stanton Ching, J. A. L., Matthew L. Jorgensen, Niangao Duan, Steven L. Suib, Sol-Gel Synthesis of Birnessite from KMnO₄ and Simple Sugars. *Chem. Mater.* **1995**, *7*, 1604-1606.
134. John D. Hem, C. J. L., Nonequilibrium models for predicting forms of precipitated manganese oxides. *Geochim. Cosmochim. Acta* **1983**, *47*, 2037-2046.
135. Kostka, J. E.; Luther III, G. W.; Nealson, K. H., Chemical and biological reduction of Mn (III)-pyrophosphate complexes: Potential importance of dissolved Mn (III) as an environmental oxidant. *Geochim. Cosmochim. Acta* **1995**, *59* (5), 885-894.
136. Klewicki, J. K.; Morgan, J. J., Kinetic Behavior of Mn(III) Complexes of Pyrophosphate, EDTA, and Citrate. *Environ. Sci. Technol.* **1998**, *32* (19), 2916-2922.
137. Klewicki, J. K.; Morgan, J. J., Dissolution of β -MnOOH particles by ligands: pyrophosphate, ethylenediaminetetraacetate, and citrate. *Geochim. Cosmochim. Acta* **1999**, *63* (19-20), 3017-3024.
138. Smith, P. F.; Deibert, B. J.; Kaushik, S.; Gardner, G.; Hwang, S.; Wang, H.; Al-Sharab, J. F.; Garfunkel, E.; Fabris, L.; Li, J.; Dismukes, G. C., Coordination Geometry and Oxidation State Requirements of Corner-Sharing MnO₆ Octahedra for Water Oxidation Catalysis: An Investigation of Manganite (γ -MnOOH). *ACS Catalysis* **2016**, *6* (3), 2089-2099.
139. Hu, Z.; Deibert, B. J.; Li, J., Luminescent metal-organic frameworks for chemical sensing and explosive detection. *Chemical Society Reviews* **2014**.
140. Lan, A.; Li, K.; Wu, H.; Olson, D. H.; Emge, T. J.; Ki, W.; Hong, M.; Li, J., A Luminescent Microporous Metal-Organic Framework for the Fast and Reversible Detection of High Explosives. *Angew. Chem. Int. Ed.* **2009**, *48* (13), 2334-2338.
141. Pramanik, S.; Hu, Z.; Zhang, X.; Zheng, C.; Kelly, S.; Li, J., A Systematic Study of Fluorescence-Based Detection of Nitroexplosives and Other Aromatics in the Vapor Phase by Microporous Metal-Organic Frameworks. *Chemistry – A European Journal* **2013**, *19* (47), 15964-15971.
142. Pramanik, S.; Zheng, C.; Zhang, X.; Emge, T. J.; Li, J., New Microporous Metal-Organic Framework Demonstrating Unique Selectivity for Detection of High Explosives and Aromatic Compounds. *J. Am. Chem. Soc.* **2011**, *133* (12), 4153-4155.

143. Cohen, S. M., Postsynthetic Methods for the Functionalization of Metal–Organic Frameworks. *Chem. Rev.* **2011**, *112* (2), 970-1000.
144. Liu, J.; Strachan, D. M.; Thallapally, P. K., Enhanced noble gas adsorption in Ag@MOF-74Ni. *Chem. Commun.* **2014**, *50* (4), 466-468.
145. He, Y.; Zhou, W.; Krishna, R.; Chen, B., Microporous metal-organic frameworks for storage and separation of small hydrocarbons. *Chem Commun (Camb)* **2012**, *48* (97), 11813-31.
146. Jeremias, F.; Henninger, S. K.; Janiak, C., High performance metal-organic-framework coatings obtained via thermal gradient synthesis. *Chem. Commun.* **2012**, *48* (78), 9708-9710.
147. Kreno, L. E.; Leong, K.; Farha, O. K.; Allendorf, M.; Van Duyne, R. P.; Hupp, J. T., Metal–Organic Framework Materials as Chemical Sensors. *Chem. Rev.* **2011**, *112* (2), 1105-1125.
148. Lu, W.; Wei, Z.; Gu, Z.-Y.; Liu, T.-F.; Park, J.; Park, J.; Tian, J.; Zhang, M.; Zhang, Q.; Gentle Iii, T.; Bosch, M.; Zhou, H.-C., Tuning the structure and function of metal-organic frameworks via linker design. *Chem. Soc. Rev.* **2014**.
149. Wang, J.-L.; Wang, C.; Lin, W., Metal–Organic Frameworks for Light Harvesting and Photocatalysis. *ACS Catalysis* **2012**, *2* (12), 2630-2640.
150. Wang, H.; Yao, K.; Zhang, Z.; Jagiello, J.; Gong, Q.; Han, Y.; Li, J., The first example of commensurate adsorption of atomic gas in a MOF and effective separation of xenon from other noble gases. *Chemical Science* **2014**, *5* (2), 620-624.
151. Doherty, C. M.; Buso, D.; Hill, A. J.; Furukawa, S.; Kitagawa, S.; Falcaro, P., Using Functional Nano- and Microparticles for the Preparation of Metal–Organic Framework Composites with Novel Properties. *Acc. Chem. Res.* **2013**, *47* (2), 396-405.
152. Wang, C.; Xie, Z.; deKrafft, K. E.; Lin, W., Doping metal-organic frameworks for water oxidation, carbon dioxide reduction, and organic photocatalysis. *J. Am. Chem. Soc.* **2011**, *133* (34), 13445-54.
153. Corma, A.; García, H.; Llabrés i Xamena, F. X., Engineering Metal Organic Frameworks for Heterogeneous Catalysis. *Chem. Rev.* **2010**, *110* (8), 4606-4655.
154. Choi, M. Y.; Pollard, J. A.; Webb, M. A.; McHale, J. L., Counterion-Dependent Excitonic Spectra of Tetra(p-carboxyphenyl)porphyrin Aggregates in Acidic Aqueous Solution. *J. Am. Chem. Soc.* **2002**, *125* (3), 810-820.
155. Gouterman, M.; Wagnière, G. H.; Snyder, L. C., Spectra of porphyrins: Part II. Four orbital model. *J. Mol. Spectrosc.* **1963**, *11* (1–6), 108-127.
156. Karl M. Kadish, K. M. S., Roger Guillard, *The Porphyrin Handbook: Inorganic, organic and coordination chemistry, Volume 3*. 1 ed.; Elsevier: 2000; Vol. 3, p 425.
157. Khairutdinov, R. F.; Serpone, N., Photoluminescence and Transient Spectroscopy of Free Base Porphyrin Aggregates. *The Journal of Physical Chemistry B* **1999**, *103* (5), 761-769.
158. Panda, M. K.; Ladomenou, K.; Coutsolelos, A. G., Porphyrins in bio-inspired transformations: Light-harvesting to solar cell. *Coord. Chem. Rev.* **2012**, *256* (21–22), 2601-2627.
159. Thyagarajan, S.; Leiding, T.; Årsköld, S. P.; Cheprakov, A. V.; Vinogradov, S. A., Highly Non-Planar Dendritic Porphyrin for pH Sensing: Observation of Porphyrin Monocation. *Inorg. Chem.* **2010**, *49* (21), 9909-9920.
160. Vangberg, T.; Ghosh, A., Direct Porphyrin–Aryl Orbital Overlaps in Some meso-Tetraarylporphyrins. *J. Am. Chem. Soc.* **1998**, *120* (25), 6227-6230.
161. *The Porphyrin Handbook Volume 6, Applications: Past, Present, Future*. Academic Press: 2000; Vol. 6, p 131.
162. Ma, S. Y.; Li, Z. H.; Liu, R. Z., Studies on the structure of N-protonated porphyrin. Part II. The effects of the substituting groups m-(p-carboxylatophenyl) and m-(p-nitrophenyl). *Journal of Molecular Structure: THEOCHEM* **2000**, *528* (1–3), 121-131.
163. Štěpánek, P.; Andrushchenko, V.; Ruud, K.; Bouř, P., Porphyrin Protonation Studied by Magnetic Circular Dichroism. *The Journal of Physical Chemistry A* **2011**, *116* (1), 778-783.

164. Farha, O. K.; Shultz, A. M.; Sarjeant, A. A.; Nguyen, S. T.; Hupp, J. T., Active-site-accessible, porphyrinic metal-organic framework materials. *J. Am. Chem. Soc.* **2011**, *133* (15), 5652-5.
165. Fateeva, A.; Chater, P. A.; Ireland, C. P.; Tahir, A. A.; Khimyak, Y. Z.; Wiper, P. V.; Darwent, J. R.; Rosseinsky, M. J., A water-stable porphyrin-based metal-organic framework active for visible-light photocatalysis. *Angew. Chem. Int. Ed. Engl.* **2012**, *51* (30), 7440-4.
166. Feng, D.; Chung, W. C.; Wei, Z.; Gu, Z. Y.; Jiang, H. L.; Chen, Y. P.; Darensbourg, D. J.; Zhou, H. C., Construction of ultrastable porphyrin Zr metal-organic frameworks through linker elimination. *J. Am. Chem. Soc.* **2013**, *135* (45), 17105-10.
167. Feng, D.; Gu, Z. Y.; Li, J. R.; Jiang, H. L.; Wei, Z.; Zhou, H. C., Zirconium-metalloporphyrin PCN-222: mesoporous metal-organic frameworks with ultrahigh stability as biomimetic catalysts. *Angew. Chem. Int. Ed. Engl.* **2012**, *51* (41), 10307-10.
168. Jiang, H. L.; Feng, D.; Wang, K.; Gu, Z. Y.; Wei, Z.; Chen, Y. P.; Zhou, H. C., An exceptionally stable, porphyrinic Zr metal-organic framework exhibiting pH-dependent fluorescence. *J. Am. Chem. Soc.* **2013**, *135* (37), 13934-8.
169. Lee, C. Y.; Farha, O. K.; Hong, B. J.; Sarjeant, A. A.; Nguyen, S. T.; Hupp, J. T., Light-harvesting metal-organic frameworks (MOFs): efficient strut-to-strut energy transfer in bodipy and porphyrin-based MOFs. *J. Am. Chem. Soc.* **2011**, *133* (40), 15858-61.
170. Zou, C.; Xie, M.-H.; Kong, G.-Q.; Wu, C.-D., Five porphyrin-core-dependent metal-organic frameworks and framework-dependent fluorescent properties. *CrystEngComm* **2012**, *14* (14), 4850.
171. Allendorf, M. D.; Bauer, C. A.; Bhakta, R. K.; Houk, R. J. T., Luminescent metal-organic frameworks. *Chem. Soc. Rev.* **2009**, *38* (5), 1330-1352.
172. Cui, Y.; Yue, Y.; Qian, G.; Chen, B., Luminescent Functional Metal-Organic Frameworks. *Chem. Rev.* **2012**, *112* (2), 1126-1162.
173. Azhdari Tehrani, A.; Ghasempour, H.; Morsali, A.; Makhoulfi, G.; Janiak, C., Effects of Extending the π -Electron System of Pillaring Linkers on Fluorescence Sensing of Aromatic Compounds in Two Isorecticular Metal-Organic Frameworks. *Crystal Growth & Design* **2015**, *15* (11), 5543-5547.
174. He, J.; Zeller, M.; Hunter, A. D.; Xu, Z., White Light Emission and Second Harmonic Generation from Secondary Group Participation (SGP) in a Coordination Network. *J. Am. Chem. Soc.* **2012**, *134* (3), 1553-1559.
175. Kang, Y.; Wang, F.; Zhang, J.; Bu, X., Luminescent MTN-Type Cluster-Organic Framework with 2.6 nm Cages. *J. Am. Chem. Soc.* **2012**, *134* (43), 17881-17884.
176. Energy, U. S. D. o. Solid-State Lighting. <http://energy.gov/eere/ssl/solid-state-lighting>.
177. Fasol, S. N. a. G., *The Blue Laser Diode, GaN Based Light Emitters and Lasers*. Springer Berlin Heidelberg: 1997.
178. Xie, R.-J.; Hirosaki, N.; Sakuma, K.; Yamamoto, Y.; Mitomo, M., Eu²⁺-doped Ca- α -SiAlON: A yellow phosphor for white light-emitting diodes. *Appl. Phys. Lett.* **2004**, *84* (26), 5404-5406.
179. Shang, M.; Li, C.; Lin, J., How to produce white light in a single-phase host? *Chem. Soc. Rev.* **2014**, *43* (5), 1372-1386.
180. Diana Bauer, D. D., Jennifer Li, Michael McKittrick, David Sandalow, Paul Telleen, Critical Materials Strategy. Energy, U. S. D. o., Ed. 2011.
181. Wei, Z.; Gu, Z.-Y.; Arvapally, R. K.; Chen, Y.-P.; McDougald, R. N.; Ivy, J. F.; Yakovenko, A. A.; Feng, D.; Omary, M. A.; Zhou, H.-C., Rigidifying Fluorescent Linkers by Metal-Organic Framework Formation for Fluorescence Blue Shift and Quantum Yield Enhancement. *J. Am. Chem. Soc.* **2014**, *136* (23), 8269-8276.
182. Shustova, N. B.; Cozzolino, A. F.; Reineke, S.; Baldo, M.; Dincă, M., Selective Turn-On Ammonia Sensing Enabled by High-Temperature Fluorescence in Metal-Organic Frameworks with Open Metal Sites. *J. Am. Chem. Soc.* **2013**, *135* (36), 13326-13329.

183. Shustova, N. B.; McCarthy, B. D.; Dincă, M., Turn-On Fluorescence in Tetraphenylethylene-Based Metal–Organic Frameworks: An Alternative to Aggregation-Induced Emission. *J. Am. Chem. Soc.* **2011**, *133* (50), 20126-20129.
184. Shustova, N. B.; Ong, T.-C.; Cozzolino, A. F.; Michaelis, V. K.; Griffin, R. G.; Dincă, M., Phenyl Ring Dynamics in a Tetraphenylethylene-Bridged Metal–Organic Framework: Implications for the Mechanism of Aggregation-Induced Emission. *J. Am. Chem. Soc.* **2012**, *134* (36), 15061-15070.
185. Datta, R. K., Luminescent Behavior of Bismuth in Rare-Earth Oxides. *J. Electrochem. Soc.* **1967**, *114* (11), 1137-1142.
186. Dianov, E. M., Bismuth-doped optical fibers: a challenging active medium for near-IR lasers and optical amplifiers. *Light Sci Appl* **2012**, *1*, e12.
187. Setlur, A. A.; Srivastava, A. M., The nature of Bi³⁺ luminescence in garnet hosts. *Opt. Mater.* **2006**, *29* (4), 410-415.
188. Sun, H.-T.; Sakka, Y.; Shirahata, N.; Matsushita, Y.; Deguchi, K.; Shimizu, T., NMR, ESR, and Luminescence Characterization of Bismuth Embedded Zeolites Y. *The Journal of Physical Chemistry C* **2013**, *117* (12), 6399-6408.
189. Ojebuoboh, F. K., Bismuth—Production, properties, and applications. *JOM* **44** (4), 46-49.
190. Mineral Commodity Summaries 2015. In *U.S. Geological Survey*, Interior, U. S. D. o. t., Ed. 2015; p 196.
191. Stavila, V.; Davidovich, R. L.; Gulea, A.; Whitmire, K. H., Bismuth(III) complexes with aminopolycarboxylate and polyaminopolycarboxylate ligands: Chemistry and structure. *Coord. Chem. Rev.* **2006**, *250* (21–22), 2782-2810.
192. Yang, N.; Sun, H., Biocoordination chemistry of bismuth: Recent advances. *Coord. Chem. Rev.* **2007**, *251* (17–20), 2354-2366.
193. Busch, S.; Stein, I.; Ruschewitz, U., Hydrate Isomerism in Coordination Polymers of Bismuth and Acetylenedicarboxylate. *Z. Anorg. Allg. Chem.* **2012**, *638* (12-13), 2098-2101.
194. Chen, X.; Cao, Y.; Zhang, H.; Chen, Y.; Chen, X.; Chai, X., Hydrothermal synthesis and characteristics of 3-D hydrated bismuth oxalate coordination polymers with open-channel structure. *J. Solid State Chem.* **2008**, *181* (5), 1133-1140.
195. Feyand, M.; Koppen, M.; Friedrichs, G.; Stock, N., Bismuth tri- and tetraarylcarboxylates: crystal structures, in situ X-ray diffraction, intermediates and luminescence. *Chemistry* **2013**, *19* (37), 12537-46.
196. Feyand, M.; Mugnaioli, E.; Vermoortele, F.; Bueken, B.; Dieterich, J. M.; Reimer, T.; Kolb, U.; de Vos, D.; Stock, N., Automated diffraction tomography for the structure elucidation of twinned, sub-micrometer crystals of a highly porous, catalytically active bismuth metal-organic framework. *Angew. Chem. Int. Ed. Engl.* **2012**, *51* (41), 10373-6.
197. Inge, A. K.; Koppen, M.; Su, J.; Feyand, M.; Xu, H.; Zou, X.; O'Keeffe, M.; Stock, N., Unprecedented Topological Complexity in a Metal-Organic Framework Constructed from Simple Building Units. *J. Am. Chem. Soc.* **2016**, *138* (6), 1970-6.
198. Savage, M.; Yang, S.; Suyetin, M.; Bichoutskaia, E.; Lewis, W.; Blake, A. J.; Barnett, S. A.; Schroder, M., A novel bismuth-based metal-organic framework for high volumetric methane and carbon dioxide adsorption. *Chemistry* **2014**, *20* (26), 8024-9.
199. Shi, F.-N.; Silva, A. R.; Yang, T.-H.; Rocha, J., Mixed Cu(ii)–Bi(iii) metal organic framework with a 2D inorganic subnetwork and its catalytic activity. *CrystEngComm* **2013**, *15* (19), 3776.
200. Sun, Y.-Q.; Ge, S.-Z.; Liu, Q.; Zhong, J.-C.; Chen, Y.-P., A novel 3-D chiral bismuth–organic framework with mixed carboxylate, pyridine and thiolate donors exhibiting a semiconductive property. *CrystEngComm* **2013**, *15* (47), 10188.

201. Thirumurugan, A.; Cheetham, A. K., Anionic Metal-Organic Frameworks of Bismuth Benzenedicarboxylates: Synthesis, Structure and Ligand-Sensitized Photoluminescence. *Eur. J. Inorg. Chem.* **2010**, 2010 (24), 3823-3828.
202. Thirumurugan, A.; Tan, J.-C.; Cheetham, A. K., Heterometallic Inorganic–Organic Frameworks of Sodium–Bismuth Benzenedicarboxylates. *Crystal Growth & Design* **2010**, 10 (4), 1736-1741.
203. Tran, D. T.; Chu, D.; Oliver, A. G.; Oliver, S. R. J., A 3-D bismuth–organic framework containing 1-D cationic inorganic $[\text{Bi}_2\text{O}_2]^{2+}$ chains. *Inorg. Chem. Commun.* **2009**, 12 (10), 1081-1084.
204. Tröbs, L.; Wilke, M.; Szczerba, W.; Reinholz, U.; Emmerling, F., Mechanochemical synthesis and characterisation of two new bismuth metal organic frameworks. *CrystEngComm* **2014**, 16 (25), 5560-5565.
205. Wang, G.; Liu, Y.; Huang, B.; Qin, X.; Zhang, X.; Dai, Y., A novel metal-organic framework based on bismuth and trimesic acid: synthesis, structure and properties. *Dalton Trans* **2015**, 44 (37), 16238-41.
206. Wang, G.; Sun, Q.; Liu, Y.; Huang, B.; Dai, Y.; Zhang, X.; Qin, X., A bismuth-based metal-organic framework as an efficient visible-light-driven photocatalyst. *Chemistry* **2015**, 21 (6), 2364-7.
207. Wibowo, A. C.; Smith, M. D.; zur Loye, H.-C., Structural Diversity of Metal–Organic Materials Containing Bismuth(III) and Pyridine-2,5-Dicarboxylate. *Crystal Growth & Design* **2011**, 11 (10), 4449-4457.
208. Wibowo, A. C.; Smith, M. D.; Yeon, J.; Halasyamani, P. S.; zur Loye, H.-C., Novel 3D bismuth-based coordination polymers: Synthesis, structure, and second harmonic generation properties. *J. Solid State Chem.* **2012**, 195, 94-100.
209. Wibowo, A. C.; Smith, M. D.; zur Loye, H.-C., New 3D bismuth-oxo coordination polymers containing terephthalate-based ligands: observation of Bi_2O_2 -layer and Bi_4O_3 -chain motifs. *CrystEngComm* **2011**, 13 (2), 426-429.
210. Wibowo, A. C.; Smith, M. D.; zur Loye, H. C., A new Kagome lattice coordination polymer based on bismuth and pyridine-2,5-dicarboxylate: structure and photoluminescent properties. *Chem Commun (Camb)* **2011**, 47 (26), 7371-3.
211. Wibowo, A. C.; Vaughn, S. A.; Smith, M. D.; Zur Loye, H. C., Novel bismuth and lead coordination polymers synthesized with pyridine-2,5-dicarboxylates: two single component "white" light emitting phosphors. *Inorg. Chem.* **2010**, 49 (23), 11001-8.
212. Bai, Y.; Dou, Y.; Xie, L.-H.; Rutledge, W.; Li, J.-R.; Zhou, H.-C., Zr-based metal-organic frameworks: design, synthesis, structure, and applications. *Chem. Soc. Rev.* **2016**.
213. Boyd, T. D.; Kumar, I.; Wagner, E. E.; Whitmire, K. H., Synthesis and structural studies of the simplest bismuth(III) oxo-salicylate complex: $[\text{Bi}_4(\mu_3\text{-O})_2(\text{HO}-2\text{-C}_6\text{H}_4\text{CO}_2)_8]\cdot 2\text{Solv}$ (Solv = MeCN or MeNO₂). *Chem Commun (Camb)* **2014**, 50 (27), 3556-9.
214. White, J. L.; Baruch, M. F.; Pander, J. E.; Hu, Y.; Fortmeyer, I. C.; Park, J. E.; Zhang, T.; Liao, K.; Gu, J.; Yan, Y.; Shaw, T. W.; Abelev, E.; Bocarsly, A. B., Light-Driven Heterogeneous Reduction of Carbon Dioxide: Photocatalysts and Photoelectrodes. *Chem. Rev.* **2015**, 115 (23), 12888-12935.
215. Qiao, J.; Liu, Y.; Hong, F.; Zhang, J., A review of catalysts for the electroreduction of carbon dioxide to produce low-carbon fuels. *Chem. Soc. Rev.* **2014**, 43 (2), 631-675.
216. Zhong, H.; Qiu, Y.; Zhang, T.; Li, X.; Zhang, H.; Chen, X., Bismuth nanodendrites as a high performance electrocatalyst for selective conversion of CO₂ to formate. *Journal of Materials Chemistry A* **2016**, 4 (36), 13746-13753.
217. DiMeglio, J. L.; Rosenthal, J., Selective Conversion of CO₂ to CO with High Efficiency Using an Inexpensive Bismuth-Based Electrocatalyst. *J. Am. Chem. Soc.* **2013**, 135 (24), 8798-8801.

218. Huang, Y.-B.; Liang, J.; Wang, X.-S.; Cao, R., Multifunctional metal-organic framework catalysts: synergistic catalysis and tandem reactions. *Chem. Soc. Rev.* **2017**, *46* (1), 126-157.
219. Zhang, X. P.; Tian, H. R.; Yan, G. F.; Su, Y.; Feng, Y. L.; Cheng, J. W., Incorporating different secondary building units of {Bi₂}, {Bi₈} and {Bi₁₀} to construct diversity of luminescent bismuth-organic frameworks. *Dalton Trans* **2013**, *42* (4), 1088-93.
220. Thirumurugan, A.; Li, W.; Cheetham, A. K., Bismuth 2,6-pyridinedicarboxylates: assembly of molecular units into coordination polymers, CO₂ sorption and photoluminescence. *Dalton Trans* **2012**, *41* (14), 4126-34.
221. Koppen, M.; Beyer, O.; Wuttke, S.; Luning, U.; Stock, N., Synthesis, functionalisation and post-synthetic modification of bismuth metal-organic frameworks. *Dalton transactions* **2017**, *46* (26), 8658-8663.
222. *The Porphyrin Handbook*. Academic Press 1999.
223. Benson, E. E.; Kubiak, C. P.; Sathrum, A. J.; Smieja, J. M., Electrocatalytic and homogeneous approaches to conversion of CO₂ to liquid fuels. *Chem. Soc. Rev.* **2009**, *38* (1), 89-99.
224. Duan, J.; Chen, S.; Zhao, C., Ultrathin metal-organic framework array for efficient electrocatalytic water splitting. **2017**, *8*, 15341.